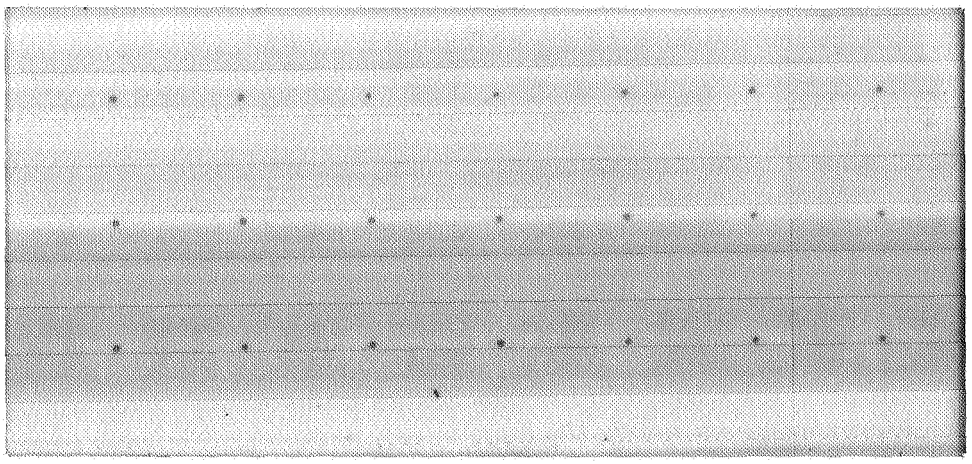

ENGINEERING AND INDUSTRIAL EXPERIMENT STATION

College of Engineering

University of Florida

Gainesville

Fourth Semiannual Report

A STUDY OF DEFECT STRUCTURES WITH THE FIELD ION MICROSCOPE

NASA Research Grant
NGR-10-005-039

Submitted to:

NATIONAL AERONAUTICS AND SPACE ADMINISTRATION

Submitted by:

DEPARTMENT OF METALLURGICAL AND MATERIALS ENGINEERING
UNIVERSITY OF FLORIDA
GAINESVILLE, FLORIDA 32601

J. J. Hren, Chief Investigator

R. W. Newman
R. C. Sanwald
U. T. Son

For the Period:

September 1, 1967 - February 29, 1968

Abstract

Results of a survey study of the secondary defects existing in quenched platinum are presented. Transmission electron microscopy used in conjunction with field ion microscopy has yielded direct experimental evidence for the existence of prismatic dislocation loops (both glissile and sessile) as well as polyhedral voids.

For the most part, the dislocation loops were observed as black spot defects in the electron microscope and were resolvable only via field ion microscopy. The loop density was estimated to be $10^{13}/cm^3$ with an average size of approximately 50 Å. In one instance a defect interpreted as a Frank loop with Burgers vector a/3 [111] was observed in the field ion microscope. Resolvable loops (i.e., > 100 Å) were found among networks of heavily jogged dislocation lines.

The void concentration reached a maximum of $7 \times 10^{14}/cm^3$ after annealing at 400°C for 24 hours and fell sharply on either side of this temperature. The shape of the voids was found to be a function of the concentration. At low density the voids can be described as regular octahedra, some of which are truncated by {100} and occasionally by {111} planes. Small voids appear spherical but careful tilting experiments reveal hexagonal cross sections implying that the shapes are {100} truncated octahedra. It is shown

that the apparent sphericity can be attributed to strain contrast arising from the matrix immediately surrounding the void.

Small tetrahedral voids have been discovered in field ion specimens, and it is postulated that these clusters are the nuclei for both voids and dislocation loops, depending upon the number and efficiency of the vacancy sinks in the local environment. The voids are shown to be extremely stable almost to the melting point.

TABLE OF CONTENTS

LIST OF TABLES

LIST OF FIGURES

LIST OF FIGURES--*Continued*

LIST OF FIGURES--*Continued*

LIST OF FIGURES--*Continued*

LIST OF FIGURES--*Continued*

INTRODUCTION

The development of the field ion microscope by E. W. Müller (1951) opened the way for the study of the defect structure of materials on the atomic scale. Relatively little progress has been made in this direction, however, since defect analysis on the atomic level is far from routine. Advances are being made in image interpretation but at the present time it is imperative that experimental results be correlated with evidence obtained by other means. For some reason this has not been done. In the present investigation extensive use has been made of both field ion microscopy and transmission electron microscopy to determine the nature of the defect structure of quenched and annealed platinum.

The type of defects to be considered in the body of this manuscript are usually referred to as secondary defects. Although grouped under a common label, secondary defects may be any one of a number of known crystallographic imperfections. These defects are all related in that they all have their origin in a supersaturation of vacant lattice sites (vacancies). Point defects are commonly produced by one of three methods:

(1) deformation, (2) radiation, (3) quenching. The latter has been chosen for this study because it does not introduce additional defects such as interstitials, dislocation tangles, and displacement spikes which would only complicate the analysis of this first study.

Vacancies are equilibrium defects and it is well known that the number of these point defects in thermodynamic equilibrium with the system increases with temperature. Therefore, a piece of metal equilibrated at some elevated temperature will contain a larger number of vacancies than would be in equilibrium at a lower temperature. Rapid quenching from near the melting point results in the retention of most of the high temperature vacancy concentration at some lower temperature, say room temperature. Since this is a non-equilibrium situation, the system lowers its free energy by allowing isolated vacancies to cluster into energetically more favorable configurations if it is permitted to recover with time. These cluster configurations are referred to as secondary defects.

The importance of secondary defects lies in their effect on the mechanical properties of crystals and crystalline materials. It is now accepted that the mechanical behavior of a crystal is governed by the motion of the line defects or dislocations through the

crystalline lattice (Read 1953, Cottrell 1953). It follows that any obstacle interfering with this motion will have some effect on the mechanical properties of the crystal. Secondary defects are such obstacles. While it is the ultimate aim to understand the effect of secondary defects on the deformation behavior of a metal in terms of their interaction with dislocations, it is first necessary to understand the atomic geometry of the cluster configurations and their density distribution. Consequently, a large portion of the literature in the field concerns itself with the geometry of these two and three-dimensional defects.

The idea that excess vacancies could condense into secondary defects was suggested by Frank (1949) and Seitz (1950) in their discussions of the origin of dislocations in crystals. The growing amount of data on the unusual behavior of quenched materials, much of which is reviewed by Cottrell (1958), led a number of workers to expect evidence of vacancy clustering from transmission electron microscopy. This expectation was fulfilled in a paper published by Hirsch *et al.* (1958) which presented direct experimental evidence for the clustering of vacancies in quenched aluminum. Frank (1949) proposed that vacancies in FCC material would agglomerate on a single {111} plane to form an area of stacking fault

surrounded by a dislocation with Burgers vector a/3 <111>. This defect was appropriately called a Frank loop. Hirsch *et al.* (1958), however, found the loops in quenched aluminum to be prismatic with a Burgers vector a/2 <110>. They suggested that the Frank loops would be energetically unstable because of the high stacking fault energy of aluminum, and would, therefore, transform to a perfect prismatic loop by a reaction:

$$a/3\ \langle 111\rangle + a/6\ \langle 11\bar{2}\rangle \rightarrow a/2\ \langle 110\rangle$$

as suggested by Kuhlmann-Wilsdorf (1958). In other words, the stacking fault could be eliminated by the nucleation of a Shockley partial dislocation.

The success of the electron microscope work on aluminum prompted Silcox and Hirsch (1959) to examine a lower stacking fault energy metal in the quenched state, namely gold. As a result of this investigation a totally new defect, the tetrahedron, was discovered. The description of the stacking fault tetrahedron in terms of its component stair-rod dislocations and fault planes is not now disputed but the scientific community has yet to agree on the mechanism of its formation. See, for example, de Jong and Koehler (1963), Kuhlmann-Wilsdorf (1965), and Chik (1965).

Further studies on quenched metals and alloys employing transmission electron microscopy have revealed the existence of polyhedral voids and an unknown defect sometimes referred to as "black death." The latter appear as small, unresolvable black spots on an electron micrograph and their character or configuration is not yet certain.

In addition to transmission microscopy, several indirect methods, notably resistivity, have been employed to study materials in the quenched state. For the most part, these methods are capable only of studying the kinetics of the clustering process. Very little information can be obtained as to the precise geometry of the secondary defects, but the kinetics of resistivity change do give an indication as to the type of defect formed. It is at this point that direct observation with the electron microscope becomes necessary. Unfortunately, some materials are not amenable to thin film microscopy for one reason or another. Platinum, until recently, was such a metal. Specifically it was not possible to electropolish a platinum foil thin enough to be transparent to an electron beam without altering the structure, although Ruedl *et al.* (1962) and Ruedl and Amelinckx (1963) observed platinum in transmission after beating the foil to less than 1000

Å thick. This is not suitable for quenching studies though, since the defects would most likely be affected by the large stresses introduced by quenching such a thin specimen (Jackson 1965a).

Studies of quenched platinum have been limited to electrical resistivity, except for that of Piercy (1960) who correlated this data with other physical and mechanical property measurements. From these data and his own studies Jackson concludes that the annealing behavior of platinum is much different from that of other quenched metals. In fact, he went so far as to say that neither loops nor tetrahedra would exist in quenched and annealed platinum. Ahlers and Balluffi (1967) have published information on an electrolytic solution with which one can prepare thin foils of quenched platinum while maintaining sub-zero temperatures. Thus, for the first time, it became possible to see if secondary defects exist in platinum following various annealing treatments of the quenched material.

The work of Ruedl and Amelinckx (1963) indicated that the defect clusters in platinum would be much smaller (possibly by an order of magnitude) than those in aluminum and gold. This suggests that it would be informative to use the field ion microscope in conjunction with the electron microscope. Field ion microscopy has already

proven its value for studying small defect clusters induced by α-particle bombardment (Müller 1960) and neutron radiation (Bowkett *et al.* 1964). Employing a technique known as field evaporation, layers of atoms can be stripped from the surface of the specimen enabling the investigator to cause the visible surface to pass through the bulk of the specimen. Hence, one has a tool with which he can determine, in three dimensions, the atomic configuration of defects within the metal tip.

This, then, was the aim of this research; to use both field ion microscopy and transmission electron microscopy in a survey study of the defect structure of quenched and annealed platinum. It is doubtful that all stable configurations have been discovered for the work on aluminum is still underway. Almost ten years after the initial studies, multilayer defects are only now being discovered (Edingdon and West 1966). It is felt that complementing the electron microscope studies with field ion microscopy not only reduces the chance of misinterpretation, as happened in the case of aluminum (Loretto *et al.* 1966), but is in fact a unique way to study the defect structure of quenched and annealed metals.

CHAPTER I

DEFECTS IN QUENCHED PLATINUM

Defect Formation

Vacancies

The first author who realized that crystals in thermal equilibrium should contain a well-defined concentration of point defects appears to have been Frenkel (1926). The thermodynamics and kinetics of these point defects is discussed extensively by Damask and Dienes (1963).

The concentration of vacant lattice sites in a crystal increases with increasing temperature according to the familiar Arrhenius relation

$$C = A \exp(-E_f/kT) \qquad (1)$$

where A is an entropy factor (~1), E_f the energy of formation for a vacancy (~1 eV), and k is the Boltzmann constant. Very large supersaturations of vacancies can be produced by rapidly quenching ($>10^4$ deg sec^{-1}) a piece of metal from temperatures near the melting point. The excess vacancies retained in the crystal can be eliminated by annealing at some intermediate temperature (~1/2 T_{mp})

thereby causing them to diffuse to some form of sink. In addition to the pre-existing or fixed sinks such as dislocations and surfaces (internal as well as external), there is evidence for the existence of variable sinks. These are variable in that their size and/or shape changes as more vacancies are annihilated, resulting in a change in the annealing kinetics. These variable sinks take on several forms: (1) voids, (2) dislocation loops, (3) stacking fault tetrahedra; but they are identical in that they all originate from the very defects which they are helping to eliminate. The geometry of these sinks will be discussed in the next section.

Equation (1) gives information as to the total number of vacancies at equilibrium but says nothing about where they are. However, reasonable assumptions suggest that 90% are isolated single vacancies with the remainder in clusters of up to about six vacancies. The relative numbers of each of these configurations is dependent upon the respective binding energies. From the data in Table 1 it is evident that the divacancy is the most mobile of these defects since higher order complexes are immobile as such.

During an annealing treatment, single vacancies and divacancies migrating through the crystal will interact to form trivacancies, tetravacancies, etc. with a corresponding reduction in the internal energy of the crystal

TABLE 1

BEST VALUES OF THE THERMODYNAMIC PROPERTIES OF POINT DEFECTS IN SOME COMMON METALS

Property	Cu	Ag	Au	Al	Ni	Pt
E_f^{1v} (eV)	1.17	1.09	0.94	0.75	1.4	1.5
E_m^{1v} (eV)	1.0	0.85	0.85	0.65	1.5	1.4
E_m^{2v} (eV)	0.65	0.58	0.65	0.3	0.72	1.1
E_b^{2v} (eV)	0.15	0.2-0.4	0.1-0.3	0.17	0.23	0.37
$C \times 10^4$	2.0	1.7	7.2	9.0	0.05	6.0-10.0
Q (eV)	2.1	1.91	1.81	1.35	2.9	2.9
γ (erg/cm^2)	85	20	50	280	150-450	95

E_f^{1v} - energy of formation of a vacancy

E_m^{1v} - energy of motion of a vacancy

E_m^{2v} - energy of motion of a divacancy

E_b^{2v} - binding energy between two vacancies

C - concentration of vacancies at T_{mp}

Q - activation energy for self diffusion

γ - stacking fault energy

as a whole. As these clusters increase in size they tend to: (1) form into spherical cavities, (2) become polyhedral-shaped cavities, (3) collapse to form Frank loops, (4) collapse to form perfect prismatic loops, or (5) form stacking fault tetrahedra. There are, as yet, no hard and fast rules as to what kind of defect will form in a particular material after a given heat treatment but all of the parameters listed in Table 1 will have a definite effect. The stacking fault energy is perhaps mentioned most often in the literature, but the problem of using it as a criterion is that there is so much controversy over its magnitude.

Secondary Defects

Cavities of various sizes and shapes have been observed in metals and alloys, and they can usually be classified as either spherical or polyhedral. It is not at all understood precisely what determines the final shape, but it is probably a combination of defect size and the surface energy of the material. The polyhedral surfaces are generally made up of low index planes and the voids are therefore quite symmetric.

Frank dislocation loops can be envisioned as the removal of part of the <111> plane from the lattice. The result is a fault in the stacking sequence, as the planes above and below the missing plane will collapse to fill the gap. The region of stacking fault is surrounded by a partial dislocation with a Burgers vector a/3 <111> and has the appearance of a pure edge dislocation (Figure 1a). The dislocation is sessile and the loop is usually hexagonal in shape with the sides parallel to <110> directions.

A second type of loop commonly found is the perfect prismatic loop. It can be obtained from the Frank loop by the nucleation of a Shockley partial, according to the reaction

$$a/3\ \langle 111\rangle + a/6\ \langle 211\rangle \rightarrow a/2\ \langle 110\rangle$$

The resulting configuration is shown in Figure 1b. It is entirely possible that the prismatic loop forms directly from the collapsed cluster, but the question is academic. It is generally felt that the prismatic loop will be favored in materials with a high stacking fault energy, but recent papers by Loretto *et al.* (1966) and Humble *et al.* (1967) place this conclusion in some doubt.

The prismatic loop can sometimes lower its energy by becoming rhomboidal in shape (it is usually elliptical) and rotating toward a {110} plane, thereby

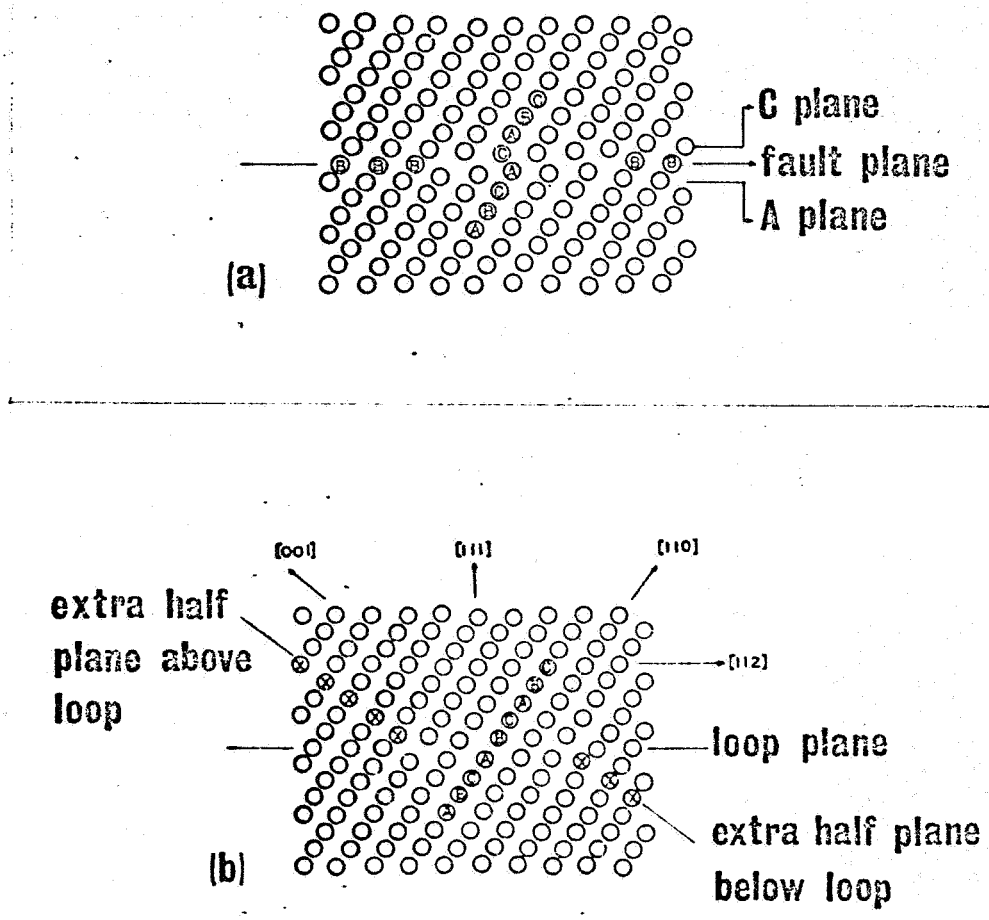

Figure 1.--Transformation of a Frank Loop to a perfect prismatic loop. (a) Side view of a Frank loop showing HCP stacking sequence across the loop plane. Viewing direction is $[1\bar{1}0]$; (b) the same loop after being converted to a perfect prismatic loop. The FCC stacking sequence has been restored, but there are two extra half planes, one above and one below, at the ends of the loop. (After Bell and Thomas 1966.)

becoming nearly pure edge in character. That is, the habit plane is not quite {110}. Both the prismatic and rhomboidal (often referred to as rhombus) loops are glissile and can move by conservative glide in the <110> direction.

The stacking fault tetrahedron, as its name implies, is a four-sided defect. Each of the faces is a {111} plane containing a stacking fault and the six lines of intersection of the faces is a stair-rod dislocation of Burgers vector a/6 <110> (Figure 2). Several mechanisms of formation of tetrahedra have been proposed (Silcox and Hirsch 1959, de Jong and Koehler 1963, and Kuhlmann-Wilsdorf 1965) but these are as yet unproven.

Review of the Work on Platinum

In view of the fact that platinum is a relatively easy metal to work with in quenching studies (Doyama 1965), it is rather surprising that so little information has been published on it. Perhaps the answer can be found in the difficulty of employing direct observation techniques with platinum. Whereas both aluminum and gold are amenable to thin film microscopy, platinum, until recently, was not. Therefore, quenching and annealing studies could not be extended beyond the somewhat limited resistivity investigations.

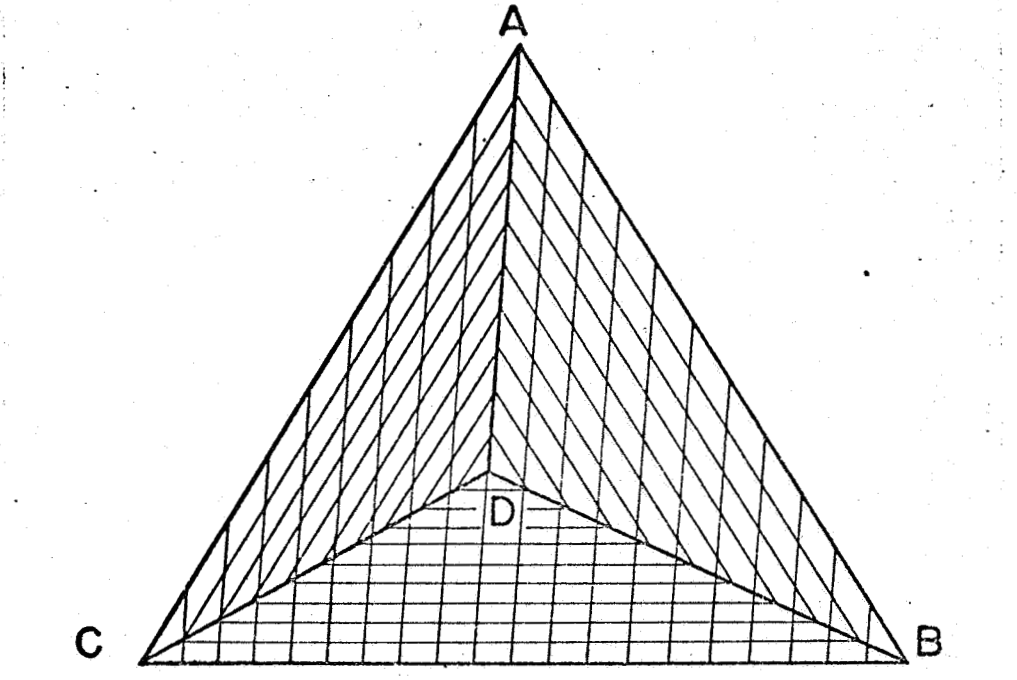

Figure 2.--The stacking fault tetrahedron. The faces are {111} containing a stacking fault. The intersecting faults give rise to stair-rod dislocations at the edges.

The first published work on quenched platinum was an electrical resistivity study by Lazarev and Ovcharenko (1955). They reported values of 1.18 eV and 1.08 eV for the energies of formation and migration of vacancies respectively. Soon after, Bradshaw and Pearson (1956) found the energy of formation to be 1.4 eV and attributed the discrepancy to an insufficient rate of quenching in the previous work. It was also concluded that there was only one recovery stage (non-exponential) and that there was no evidence for vacancy agglomeration. In a later paper (Pearson and Bradshaw 1957) no significant effect was found with the addition of rhodium and gold as impurities. Successful experiments with gold prompted Ascoli *et al.* (1958) to make new measurements on platinum. The energy of formation was determined to be 1.23 eV. The annealing curves exhibited exponential behavior (unlike Bradshaw and Pearson's data) from which the migration energy was a surprisingly large 1.42 eV. Of equal significance was the calculation of the number of jumps made by a typical vacancy during anneal, before annihilation. Whereas Bradshaw and Pearson (1956) had calculated 10^{10} jumps, Ascoli *et al.* (1958) arrived at a value of 10^{7} to 10^{8}. However, they also found no evidence for defect clusters.

Bacchella *et al.* (1959) were the first authors to suggest that the complex kinetics observed after high temperature quenches might be due to some clustering of vacancies. Measured values of the activation energies were not significantly different from those of Ascoli *et al.* (1958), i.e.,

$$E_f = 1.20 \text{ eV and } E_m = 1.48 \text{ eV}$$

Müller (1960) made a vacancy count on quenched platinum using the field ion microscope and calculated a value of 1.15 eV for E_f. However, Pimbley *et al.* (1966) found the number of vacancies to be anomalously high and attributed this to a stress effect inherent in field ion microscopy.

Piercy (1960) made a rather thorough investigation of point defects in platinum, using deformation and neutron radiation as well as quenching to introduce an initial excess of point defects. He also complemented electrical resistivity measurements with x-ray line broadening, hardness, and density measurements. Quenching from above 1600°C, Piercy found $E_m = 1.13$ eV in good agreement with the work of Bradshaw and Pearson (1956). Values of E_m for the irradiated specimens compare well with those of Ascoli *et al.* (1958) and Bacchella *et al.* (1959). Piercy

attributes the lower value to the motion of divacancies and the higher to single vacancies.

The order of reaction is a measure of the rate of change of a number of jumps required by a defect to reach a sink during the recovery process. Therefore, it should be possible to determine the type of sink from measurements of the relaxation time and the jump frequency. Piercy argues that 10^8 to 10^9 jumps (his calculation) is much too high for the recombination of defects but, if the defects are being annihilated at dislocations, the order of reaction might be expected to be unity. He reasons that the observed value of 1.46 may be caused by a change in the dislocation network due to extensive climb. Thus the last defects will migrate to a much different dislocation network than was initially present.

Jackson (1965a) quenched platinum wires from various temperatures in the range from 700°C to 1750°C in an attempt to resolve the discrepancy between the reported activation energies. His findings are listed in Table 2, along with previously obtained values. The evidence is quite convincing for assigning the lower value, 1.1 eV, to the motion of divacancies and the high value, 1.4 eV, to single vacancies. His data also verify that there is only one clearly resolved annealing state,

TABLE 2

COLLECTED VALUES FOR THE ENERGIES OF FORMATION AND MOTION OF VACANCIES IN PLATINUM

E_f (eV)	E_m (eV)	Basis of Measurement	Reference
1.18	1.08	Quenched from 1600°C	Lazarev and Ovcharenko (1955)
1.40	1.20	Quenched from 1600°C	Bradshaw and Pearson (1956)
1.23	1.42	Quenched from 1200°C	Ascoli *et al.* (1958)
1.20	1.48	Quenched from 1200°C	Bacchella *et al.* (1959)
1.15	. .	Quenched from ∿1600°C	Müller (1959)
. .	1.13	Quenched from 1600°C	Piercy (1960)
. .	1.40	Neutron Irradiated	Piercy (1960)
1.51	1.10	Quenched from 1600°C	Jackson (1965a)
. .	1.38	Quenched from 1000°C	Jackson (1965a)
. .	1.36	Electron Irradiated	Bauer and Sosin (1966)
1.58	. .	Theoretical	Mukherjee (1966)

regardless of initial concentration. Jackson also states that the shape of the isothermal annealing curves correspond to diffusion of point defects to sinks that become less efficient with time. He concludes that the very low resistivity increment remaining after anneals below 1/4 T_{mp} and the large number of jumps (two orders of magnitude greater than in gold) for vacancy annihilation argue that the sinks for vacancies in platinum are much different from those in other metals.

Amelinckx's group in Belgium has been alone in the use of TEM (transmission electron microscopy) to study quenched platinum foils. Ruedl *et al.* (1962) and Ruedl and Amelinckx (1963) were principally interested in radiation damage, but many of their findings are quite applicable to the present work. This is particularly true in the case of foils quenched prior to irradiation. However, one must be aware that quenching strains in the extremely thin (1000 Å) foils could have a significant effect on these results. This problem has been investigated by Jackson (1965b), and the principal effect seems to be a change in the vacancy structures produced by subsequent aging.

Ruedl *et al.* (1962) reported finding defects which were interpreted as spherical voids and some instances of polygonal features in the neighborhood of 100 Å diameter;

the contrast of both being quite different from that of dislocation loops. The presence of these cavities rather than loops is attributed to the high surface energy of platinum. It is felt that the energy barrier in transforming from a spherical to a penny-shaped cavity would be rather large, and would therefore inhibit the collapse of clusters into loops. It should be pointed out, however, that the concept of surface energy become ambiguous when dealing with very small surfaces. In fact, it has been suggested by Jackson (1962) that the energy of a cluster might better be calculated as the energy of formation of a vacancy divided by its surface area. If this be the case, the energy of a void will always be less than that of a Frank loop, whereas the reverse is true if the bulk surface energy is used (Friedel 1964). Thus, as Clarebrough (1966) points out, it is impossible to decide which type of defect is more stable at small sizes, without detailed knowledge of surface energies for very small voids.

Bauer and Sosin (1966) found stage IV recovery of electron irradiated platinum to be a diffusion-controlled process up to approximately 50% recovery. The rest of the recovery is considerably slower than predicted by theory. According to them, the possible mechanisms which may account for this delay include: (1) clustering of the vacancies, (2) exhaustible sinks, (3) concurrent trapping

of vacancies during the diffusion process. The authors choose to explain their results by the third mechanism. Their reason for ruling out the second are understandable, but their basis for ruling out the first is open to question (Chik 1965). It is worth noting that they measured the activation energy of stage IV recovery to be 1.36 eV; i.e., approximately equal to the energy of motion of single vacancies.

Cízek (1967) investigated the irreversible component of resistivity remaining after repeated quenching of platinum wires. After subtracting out the non-recoverable resistivity increment attributable to dimensional changes in the specimen, some 20% of the irreversible change was unaccounted for. The author suggests that while vacancy clusters and/or voids may contribute, it is more reasonable to investigate the possibility of more stable defect configurations such as the oxygen stabilized stacking fault tetrahedra present in silver up to 930°C (Clarebrough *et al.* 1964).

It should be mentioned at this point that Ruedl *et al.* (1962) observed dislocation configurations indicating the possibility of dissociation into partials (i.e., Lomer-Cottrell barriers). This was complemented by a common occurrence of annealing twins and only rare

observations of cross slip which, when it did occur, was rather complicated. The authors are cognizant of the fact that the stacking fault energy of platinum is reportedly high (75-95 erg/cm^2).

While a discussion of irradiation experiments is perhaps not appropriate here, the defects observed by Ruedl *et al.* in foils bombarded by neutrons, fission fragments, or α particles are of interest. Both black spot defects ("black death") and resolvable loops were present. The prismatic nature of the loops was inferred from motion in <110> directions during observation. This is consistent with the concept of conservative glide on a prismatic cylinder. Evidence was also found for interaction between these defects and dislocation lines. The resulting ragged appearance could be due to climb or stress field interactions. Large polyhedral voids and prismatic loops were found to occur in foils exposed to α-particles and subsequently annealed at temperatures up to 500°C. The voids were presumed to be filled with helium gas, the presence of which may stabilize the cavities. This may be substantiated by the fact that the voids remained after anneals in excess of 700°C.

CHAPTER II

ELECTRON MICROSCOPY

Contrast Theory

When the electron microscope is used with thin metal foils, extensive use is made of the phenomena of diffraction of electrons by a crystal lattice. The radius of the Ewald sphere is extremely large for electron diffraction; so large, in fact, that it is almost planar over the solid angle subtended in the electron microscope. The small curvature that does exist is compensated for by the rod-like nature of the reciprocal lattice points. The physical reason for the existence of these "relrods" is the relatively small number of reflecting planes in the thickness direction. There simply are not enough scattering centers to attain complete destructive interference for non-Bragg conditions. Therefore, the diffraction peak (i.e., reciprocal lattice point) is broadened in the direction of the small dimension and the extent of the streaking varies inversely as the foil thickness. (This phenomenon is analogous to particle size broadening encountered in x-ray diffraction.) As a result, the diffraction pattern that is projected on the microscope

screen is actually a plane section through the reciprocal lattice of the crystal. Most of the commonly observed patterns display a high degree of symmetry and are relatively easy to identify.

The normal procedure is to intercept all diffracted beams with an aperture allowing only the transmitted beam to pass through the lens system to be magnified and projected onto the fluorescent screen. Thus, any regions of the crystal which are diffracting strongly will appear dark on the screen.

When studying defects it is often desirable to view what is called the "dark field" image. This is a procedure whereby the above mentioned objective aperture is moved so that only one of the diffracted beams passes through the lens system. According to the Kinematical Theory developed by Hirsch *et al.* (1960), the dark field and bright field images should be complementary because of the two beam assumption. In practice this is not always found to be the case, but the discrepancies can usually be explained with the more complex Dynamical Theory (Howie and Whelan 1961).

Diffraction by a Perfect Crystal

Representing an electron wave at the position $\vec{r}$ by the function exp $(2\pi i \vec{k}_o \cdot \vec{r})$ and the scattered wave by

$\exp(2\pi i\,\vec{K}\cdot\vec{r})$, the total amplitude of electron waves scattered from an assembly of unit cells is:

$$A = \sum_n F_n \exp(2\pi i\,\vec{K}\cdot\vec{r}_n) \tag{2}$$

where F_n is the electron scattering factor, $\vec{K} = \vec{k} - \vec{k}_o$, $\vec{r}_n = n_1\hat{a} + n_2\hat{b} + n_3\hat{c}$, and the summation extends over all atom positions in the crystal. The total scattered amplitude is a maximum (i.e., the exponential is unity) when $\vec{K}$ is a reciprocal lattice vector.

$$\vec{K} = h\hat{a}^* + k\hat{b}^* + l\hat{c}^* \equiv \vec{g} \tag{3}$$

which simply says that the Bragg law is satisfied. By definition, the magnitude of a reciprocal lattice vector is equal to the reciprocal of the spacing between the planes described by that vector (see Figure 3a). Hence

$$|\vec{g}| = 1/d = \frac{2\sin\theta}{\lambda} \tag{4}$$

which is the Bragg equation.

In general there is a distribution of scattered radiation such that the crystal need not be in the exact Bragg position to result in some diffracted intensity. If the deviation is described by the vector $\vec{s}$ we have

$$A = \sum_n F_n \exp[2\pi i(\vec{g} + \vec{s})\cdot\vec{r}_n] \tag{5}$$

where $\vec{K} = \vec{g} + \vec{s}$ as in Figure 3b. Recognizing that $\vec{g}\cdot\vec{r}_n$ is an integer and approximating the summation by an integral, we have, for a given $\vec{s}$

$$A(s) = \frac{F}{V}\int_\tau \exp(2\pi i\, \vec{s}\cdot\vec{r}_n)\,d\tau \qquad (6)$$

For a crystal of infinite dimension in the x and y direction and thickness t

$$A(s) = F\int_{-t/2}^{t/2}\exp(2\pi isz)\,dz = \frac{\sin\pi ts}{\pi s} \qquad (7)$$

From which

$$I(s) \propto \frac{\sin^2\pi ts}{(\pi s)^2} \qquad (8)$$

This intensity distribution is plotted in Figure 4. In other words this says that the thinness of the crystal causes sufficient relaxation of the Bragg condition which in turn allows a considerable amount of diffraction to occur even though the crystal is not quite in the proper orientation; the misorientation being described by the vector $\vec{s}$.

The above equation also indicates that the intensity of the transmitted and diffracted beams oscillates with depth as illustrated in Figure 5. At successive depths t_o, the diffracted intensity is zero and the transmitted

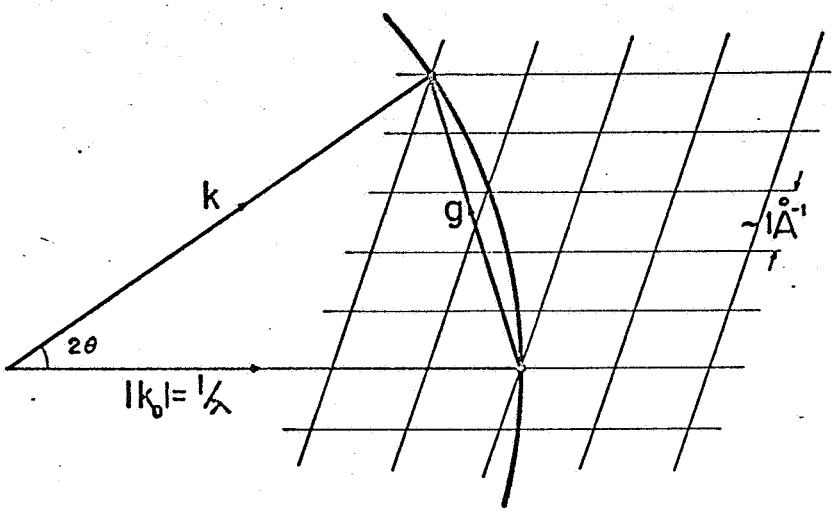

(a)

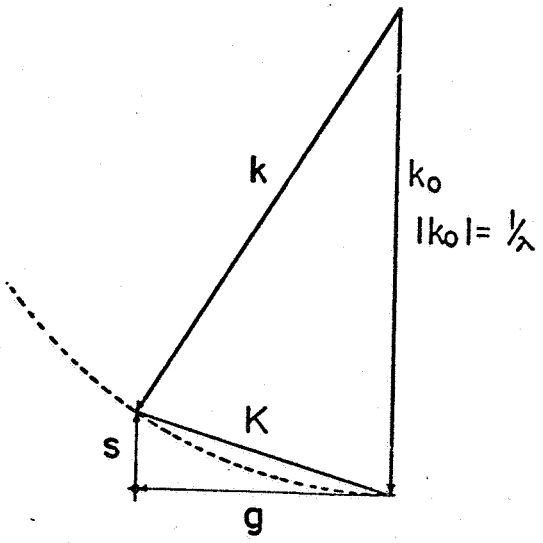

(b)

Figure 3.--Reflecting sphere construction for electron diffraction. (a) When the reciprocal lattice point is on the Ewald sphere, (b) displaced from the Ewald sphere by the vector $\vec{s}$.

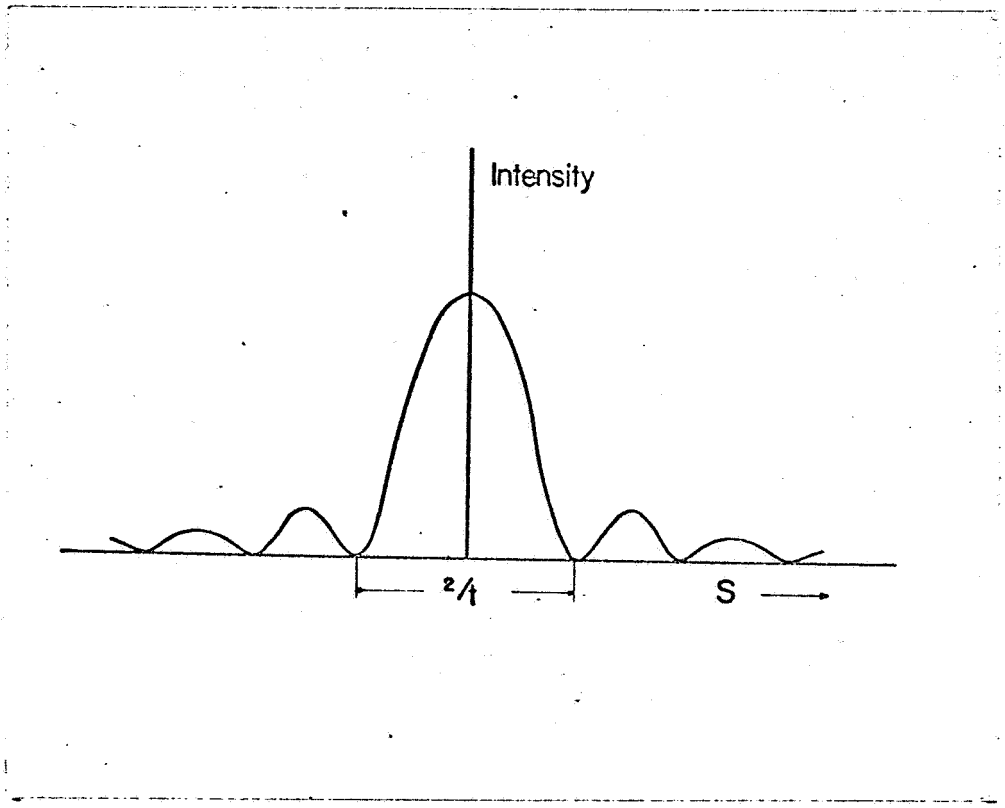

Figure 4.--Diffracted intensity versus the interference error, $\vec{s}$, according to the kinematical approximation.

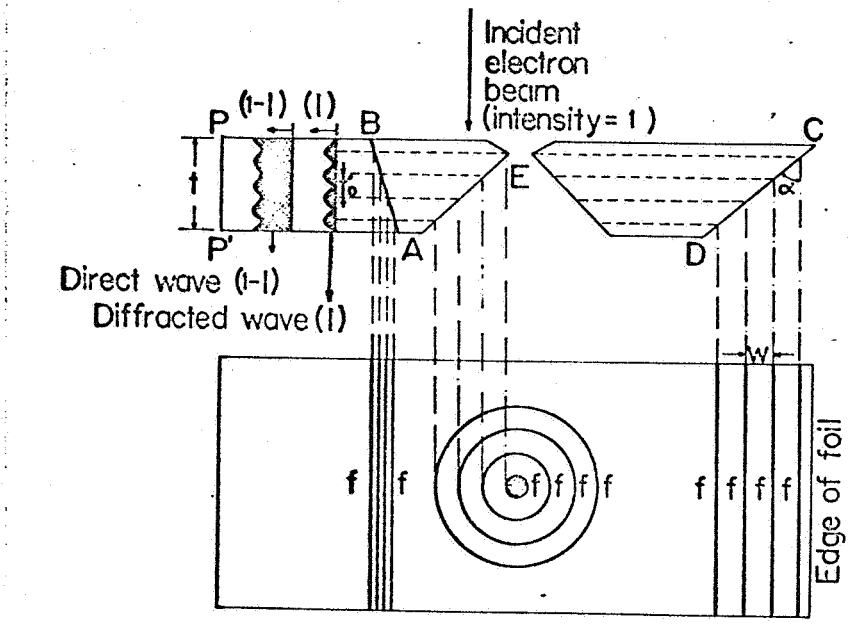

Figure 5.--Schematic illustration of the origin of fringe contrast. (a) Section through the crystal showing kinematical intensity oscillations of direct and diffracted waves. AB represents a grain boundary or stacking fault, CD a wedge, and E a hole. (b) Section normal to beam showing dark fringes f (extinction contours) as they would appear in a bright field image. (After Thomas 1962.)

intensity reaches a maximum. The depth periodicity of this intensity oscillation is $1/|\vec{s}|$ and reaches a maximum at $|\vec{s}| = 0$. That is

$$\lim_{|\vec{s}| \to 0} t_o = \zeta \tag{9}$$

where ζ is defined as the extinction distance. Note that this is not quite rigorous since ζ is a function of both the operating reflection and the material under observation.

With this information we can explain two contrast effects commonly observed in the electron microscope: extinction contours and bend contours. Practically all specimens used in transmission microscopy are slightly bent and non-uniform in thickness. Extinction contours will occur in wedge-shaped regions of the specimen as a result of the sinisoidal variation of the transmitted and diffracted beams discussed above. The contours will appear as continuous alternating bands following equi-thickness paths, as schematically illustrated in Figure 5. Local curvature of the foil will cause some regions (continuous surfaces) to be rotated into diffracting orientation giving rise to continuous dark bands called bend contours. The two can easily be distinguished since the latter is very sensitive to the angle between the incident

beam and the foil normal while the former is dependent principally on the thickness of the crystal. Hence, a small amount of specimen tilt will cause a bend contour to move much more rapidly across the field of view.

Diffraction by an Imperfect Crystal

Any defect within a crystal which produces a distortion of some set of lattice planes $\{hkl\}$ will alter the diffraction conditions of that set of planes in the vicinity of the defect. If the atom at $\vec{r}_n$ is displaced by the vector $\vec{R}$, equation 6 becomes

$$A(s) = \frac{F}{V}\int_{\tau} \exp[2\pi i\, \vec{K}\cdot(\vec{r}_n + \vec{R})]d\tau \qquad (10)$$

Neglecting the term $\vec{s}\cdot\vec{R}$ and again assuming the crystal to be finite only in the z-direction, we have

$$A(s) = \frac{F}{V}\int_{-t/2}^{t/2} \exp[2\pi i s z]\, \exp[2\pi i\, \vec{g}\cdot\vec{R}]dz \qquad (11)$$

where $\alpha = 2\pi\vec{g}\cdot\vec{R}$ is an additional phase factor due to the presence of the defect. The contrast at a defect is then determined by computing the difference between the intensity diffracted by the perfect and imperfect crystal, all other parameters being equal.

Defect Interpretation

Dislocations

It is sufficient for the present purpose to consider the intuitive explanation for contrast at dislocations as originally presented by Amelinckx (1964). Let us assume that we have an edge dislocation in a crystal. This could be depicted schematically as in Figure 6. Suppose that the set of planes outside the region E_1 - E_2 would satisfy the Bragg condition for diffraction if the foil were rotated slightly counterclockwise about the normal to the paper. Note that the planes in the region E_1 - E have undergone such a rotation due to the presence of the dislocation, while the same set of planes in E - E_2 have rotated in the opposite sense. As mentioned previously, the fact that the foil is much thinner in one dimension makes it possible to have some diffraction even though the crystal is not precisely oriented. Under these conditions (thin foil) a considerable intensity is diffracted away in the perfect part of the foil outside E_1 - E_2; the remaining part is transmitted. The figure reveals that the Bragg condition is better satisfied on the left than on the right of the dislocation. Consequently, more intensity will be diffracted away from E_1 (to be intercepted by the above mentioned aperture) and

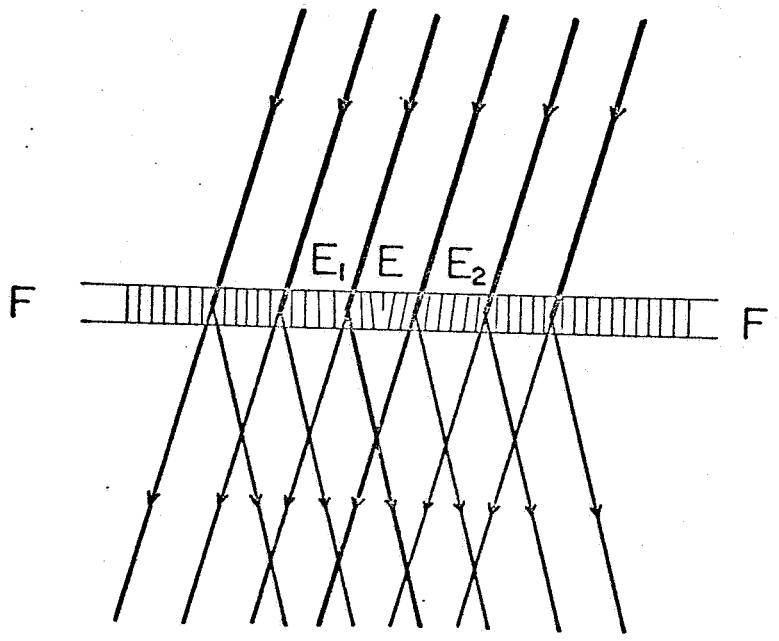

Figure 6.--Diffraction of electrons by a foil containing an edge dislocation at E. In E_2, less intensity is diffracted away than in the perfect part while more is diffracted away in E_1. (After Amelinckx 1964.)

less away from E_2. Therefore, when the transmitted beam strikes the fluorescent screen, the intensity at E_1 will be lower than background and greater than background at E_2. That is, a black line will be observed slightly *to the E_1 side* of the actual dislocation. It can be shown that this analysis holds equally well for any arbitrary dislocation and Burgers vector.

Determination of the Burgers Vector

It follows from the intuitive picture presented above that contrast effects are to be expected only from those lattice planes which are deformed by the presence of the dislocation. To a first approximation it can be assumed that the planes parallel to the Burgers vector will not be affected and, therefore, diffraction from these planes will not exhibit contrast effects. In other words, if the foil is oriented so that this particular set of planes is in the reflecting condition, the dislocation will be invisible.

Since the diffraction vector $\vec{g}$ is normal to the set of diffracting planes, we can state that the dislocation will be invisible if the relation $\vec{g}\cdot\vec{b} = 0$ is satisfied. Knowing two vectors $\vec{g}$ for which this equation holds with respect to a single dislocation, it is possible to determine $\vec{b}$ for that dislocation. To avoid ambiguity

in the analysis, it is necessary to employ the dark field technique. The procedure is to tilt the specimen until a particular defect disappears. Assuming the brightest spot on the diffraction pattern to be the cause of the observed contrast, it follows that the displacement vector $\vec{R}$ (in this case $\vec{R} = \vec{b}$) is parallel to the set of planes $\vec{g}$. If the correct reflection has been chosen, the defect will also be invisible in the dark field image of this spot.

Dislocation Loops

Although a dislocation cannot terminate within a crystal (Frank 1951), it may close on itself to form the so-called dislocation loop. The nature of the dislocation requires that a sign convention be set up to avoid confusion in analysis. The actual convention is a matter of personal preference, but must be consistent.

Define the Burgers vector as the closure failure FS after traversing the circuit in a clockwise direction while looking in the positive direction of the dislocation line (Bilby *et al.* 1955). This circuit is also defined as a right hand screw. Using this FS/RH convention, a 90° counterclockwise rotation of the Burgers vector points in the direction of the extra half plane for the case of a pure edge dislocation. See Figure 7a. It follows that the Burgers vector of a right hand screw

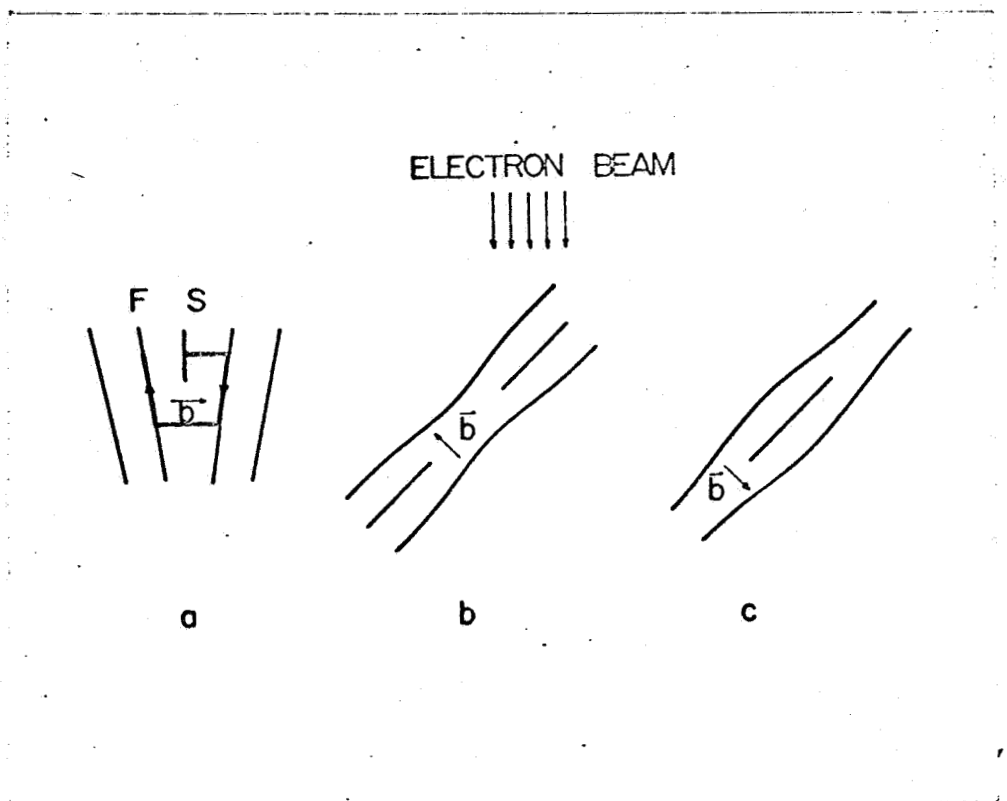

Figure 7.--Burgers vector convention for dislocation loops. (a) FS/RH convention for defining the Burgers vector; (b) applied to a vacancy loop; (c) applied to an interstitial loop.

dislocation will point along the negative direction of the dislocation line while a left hand screw will have a Burgers vector in the positive sense of the line.

Now define the positive sense of going around the dislocation loop as clockwise when viewed from above; i.e., in the direction of the electron beam. Thus, a vacancy loop will have a component making an acute angle with the upward drawn normal to the plane containing the loop. That is, if we use a "left hand rule" to describe a vacancy loop and a "right hand rule" for the interstitial loop, the fingers of the hand point in the positive direction round the loop and the thumb defines the sense of the Burgers vector. This is schematically illustrated in Figure 7b and c.

In the light of our knowledge concerning the position of the dislocation line relative to its image, consider three intermediate positions of a vacancy loop as it is rotated counterclockwise through the Bragg condition about an axis normal to $\vec{g}$ and $\vec{b}$. In Figure 8, the dotted line is the actual position of the loop while the solid line represents the image of the loop. Choosing $\vec{s}$ as positive when the reciprocal lattice point associated with $\vec{g}$ lies inside the Ewald sphere (angle of incidence on the reflecting planes is greater than the Bragg angle),

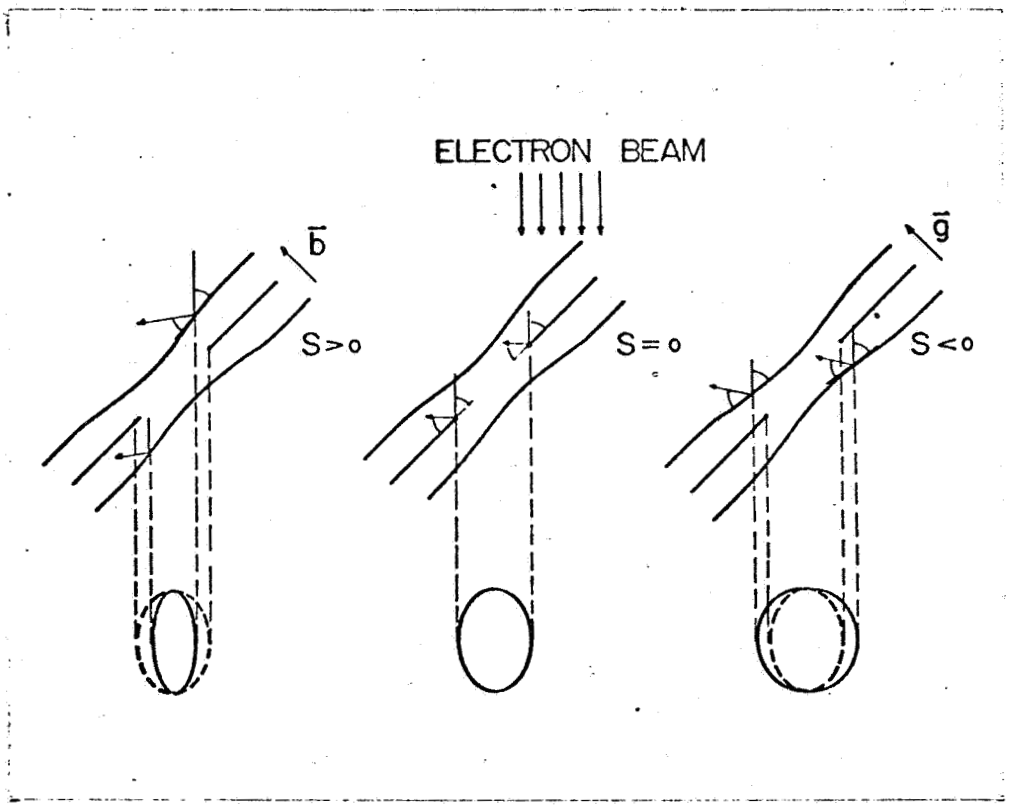

Figure 8.--Relative position of the dislocation loop as the set of planes, $\vec{g}$, is rotated through the Bragg orientation.

the image of the loop will lie inside or outside the actual position of the loop depending on whether the sign of $(\vec{g}\cdot\vec{b})\vec{s}$ is positive or negative respectively.

Kikuchi Lines

The above discussion leads to the question of how to determine the sign of $\vec{s}$. All of the previous development assumes the electrons to be elastically scattered by the atoms, but it is known that there will be some inelastic scattering resulting in an incoherent beam of electrons. Their origin is not completely understood but it is postulated that the divergent beam can undergo Bragg diffraction and produce a pair of nearly straight lines on the diffraction pattern, one dark and one light. The two will be separated by a distance commensurate with the magnitude of the associated vector $\vec{g}$. Figure 9 is a diagram showing the relation between the sign of $\vec{s}$ and the positions of the dark and light Kikuchi lines. Note that the light line is always furthest from the main beam.

Stacking Faults

The discussion of loops also leads us to consider the contrast arising from the presence of stacking faults. The formation of the stacking fault on the interior of a Frank dislocation loop of Burgers vector a/3<111> was

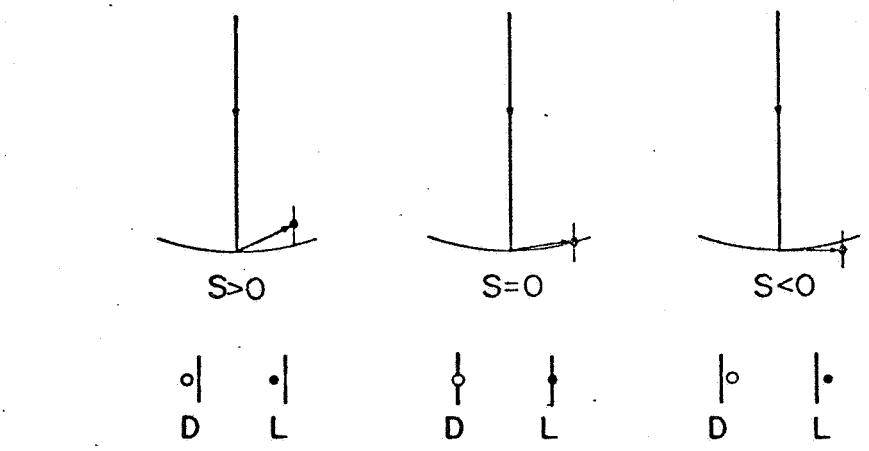

Figure 9.--Relative positions of the diffraction spot and the Kikuchi line due to the same reflection. The open circle represents the main beam and the solid circle is a particular diffracted beam.

discussed in Chapter I. We are concerned here with the interpretation of such a defect with transmission electron microscopy.

Contrast arises at a stacking fault because such a defect displaces the reflecting planes with respect to each other across the plane of the fault. Using the appropriate value of $\vec{R}$ in equation 11, we find that the observed contrast is a function of the position of the plane in the foil. In fact, the observed intensity is a periodic function since the diffracted intensity oscillates with depth into the crystal. For the general case of a fault inclined to the electron beam, the depth periodicity will become visible as alternating contrast fringes parallel to the line of intersection (or projected line of intersection) of the fault plane and the surface of the foil. This fringe contrast is illustrated in Figure 5. Clearly, if the extinction distance t_o is known, the dimension of the fault can be obtained (to within the error between t_o and ζ) from the product nt_o, where n is the number of fringes. The fringe contrast also provides valuable information for determining the plane of the fault.

This information is usually sufficient to specify the nature of the fault but a cross check is possible with a $\vec{g}\cdot\vec{b}$ criterion. The stacking fault displacement

vector $\vec{R}$ is defined by the shear at the fault, or the Burgers vector in the case of the Frank loop. Referring again to equation 11 we find that there is no contribution to the intensity for the case of $\alpha = 2\pi n$, i.e., when $\vec{g}\cdot\vec{R} = n$. In words this means that the fault will be invisible when the vector $\vec{R}$ moves the reflecting planes normal to themselves by an integral number of spacings between the planes or when the displacement is parallel to the reflecting planes as in Figure 10. One other criterion for the invisibility of stacking fault fringes involves the dimensions of the fault plane. If the fault does not extend over a depth in the crystal of more than an extinction distance for the operating reflection, no fringe contrast will be observed. The fault will, however, appear either dark or light depending on its position in the foil.

The dislocation line bounding a faulted loop presents a problem quite different than that encountered in the unfaulted or prismatic loop mentioned above, as it is a partial dislocation. Under these circumstances, the $\vec{g}\cdot\vec{b}$ criterion no longer applies since $\vec{b}$ is not a lattice vector. Therefore, the scalar is not necessarily an integer but, rather, it is usually found to be a multiple of 1/3. Gevers (1963) has shown that the variation in contrast will not be significant unless

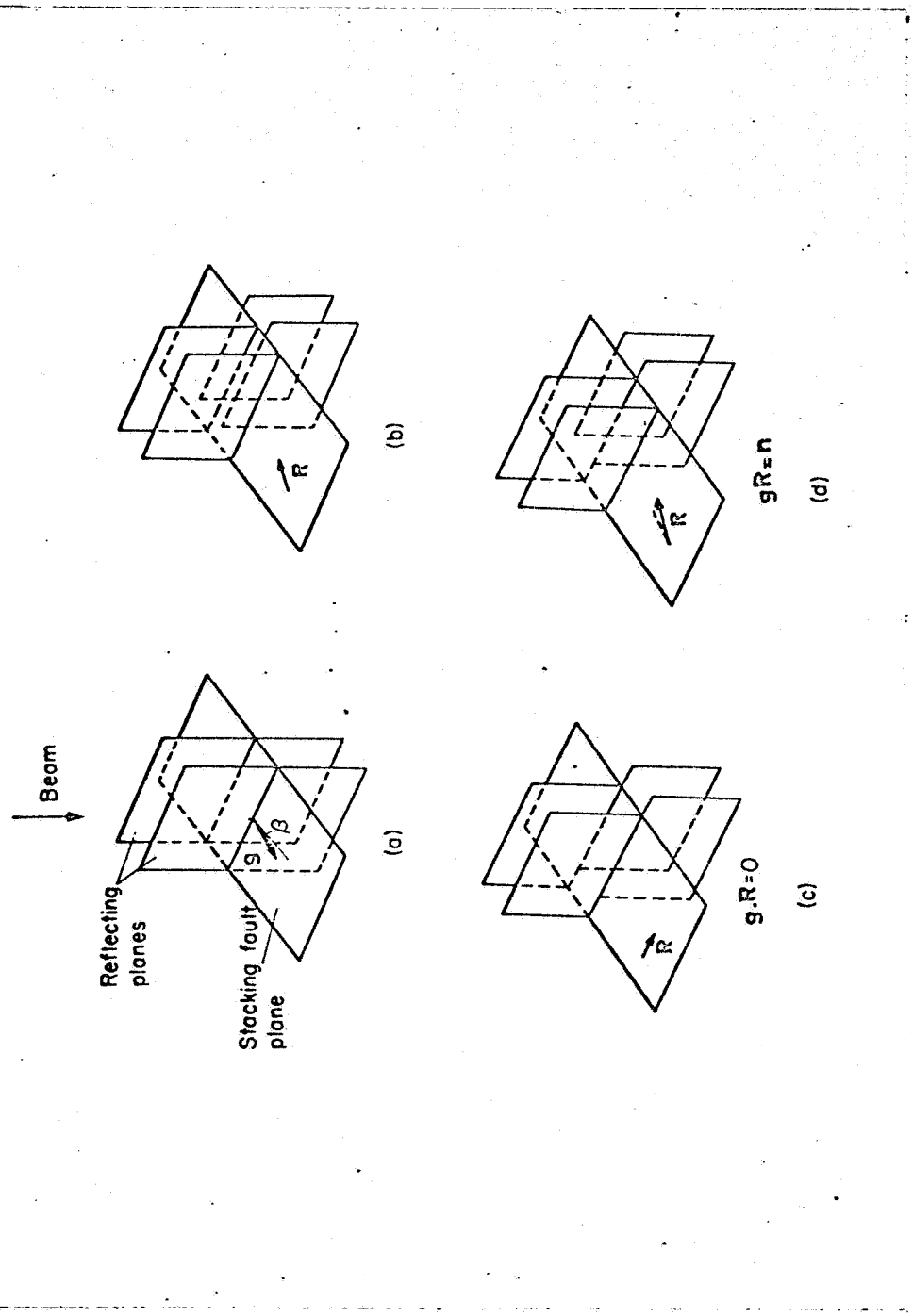

Figure 10.--Diagram showing the displacement of reflecting planes by a stacking fault to give contrast in (b) but not in (c) or (d). (After Smallman and Ashbee 1966.)

$|\vec{g}\cdot\vec{b}| \geq 2/3$. However, for $\vec{s} > 0$ and $\vec{g}\cdot\vec{b} < 0$ the image of the dislocation line will be superimposed on the fault contrast and proably not be visible. Silcock and Tunstall (1964) showed that the dislocation would be in good contrast for $\vec{g}\cdot\vec{b} = + 2/3$ but would be in poor contrast for $\vec{g}\cdot\vec{b} = - 2/3$, provided the deviation from the Bragg orientation is rather large, i.e., $t_o\vec{s} \geq 0.6$. Loretto *et al.* (1966) used this criterion to show that, contrary to common belief, 95% of the loops in quenched aluminum are faulted. This is significant in that the loops were too small to exhibit stacking fault contrast.

Voids

Another defect commonly observed in quenched materials is the void or large vacancy cluster. van Landuyt *et. al.* (1965) have shown that the contrast at a void is adequately represented by a phase angle $\alpha = 2\pi sf$, where f is the thickness of the void. Further, their theory predicts odd contrast behavior such as: (1) contrast variation as a function of depth, void size, the parameter $\vec{s}$, total foil thickness, and (2) a possible lack of contrast reversal from bright field to dark field. The interpretation is relatively simple for the case of a thick foil (> 5 t_o) with $\vec{s} = 0$, since the contrast will be mainly due to normal absorption.

However, the voids will have to be larger than 1/2 t_o before they produce a clear positive contrast (i.e., lighter than background). Unfortunately, it is not always possible to see defects in the region of $\vec{s} = 0$ and one must usually work in regions of $\vec{s} > 0$ (anomalous transmission region).

An attempt has been made to generalize the results of van Landuyt as they apply to the case of secondary defects in platinum foils: (1) the foils are considered as being thick, (2) $1/4\ t_o < f < t_o$, (3) the absorption μ is relatively high, (4) the defects will be confined to the center of the foil. As can be seen from Tables 3 and 4, the contrast in both bright and dark fields is quite unpredictable. Therefore, some knowledge of defect size and the diffraction conditions is required in order to determine whether contrast should be positive or negative. Using both bright and dark field images, the above mentioned tables, and large tilt angles, one should be able to distinguish voids from loops. In fact it is possible to specify the geometry of the defect as shown in Chapter V.

TABLE 3

EXPECTED CONTRAST FROM VOIDS AS A FUNCTION OF DIFFRACTION CONDITIONS

Void Dimension (f)	Bragg Error ($\vec{x} = \vec{s}t_o$)	Bright Field ($I - I_o$)	Dark Field ($I - I_o$)
1.8 t_o	0.2	N > P	P
	0.5	P > N	N > P
	1.0	N > P	P = N
1.0 t_o	0.2	P = N	P = N
	0.5	N	N > P
	1.0	P	P

Assume the absorption coefficient, μ, to be $3\pi/\tau_o$, where τ_o is the absorption length and is usually taken as 10 t_o.

The parameter $\vec{x}$ is a measure of the misorientation from the Bragg angle.

N indicates that the void will appear darker than background and P indicates that the void will appear lighter than background.

TABLE 4

EXPECTED CONTRAST FROM VOIDS AS A FUNCTION OF VOID SIZE

Void Dimension (f)	Bright Field ($I - I_o$)	Dark Field ($I - I_o$)
1/8 t_o	P > N	N > P
1/4 t_o	P > N	N > P
1/2 t_o	N > P	N > P
1 t_o	N	N > P

Assume $x = st_o = 0.5$.

CHAPTER III

FIELD ION MICROSCOPY

Basic Theory

As discussed in the Introduction, the field ion microscope has resolving power and magnification capabilities enabling the direct observation of the atomic lattice. Since the concept of the field ion microscope is relatively new (Müller 1951), there are almost as many designs as there are microscopes. However, they all have the same basic components (Figure 11). The specimen is a short fine wire polished to produce a sharp hemispherical tip of 100 to 1000 Å radius which is connected to metal electrodes immersed in a cryogenic fluid such as liquid N_2, Ne, H_2 or He. Facing the tip, a few centimeters away, is a phosphor screen which emits photons when bombarded by ionized atoms and is an integral part of the vacuum chamber enclosing the specimen. The system is evacuated to 10^{-7} to 10^{-9} Torr, backfilled with high purity (99.9995%) helium gas to a pressure of 1 to 10μ, and a positive potential of up to 30 kV is impressed on the tip relative to the screen. The strength of the resulting field at the surface depends on both the

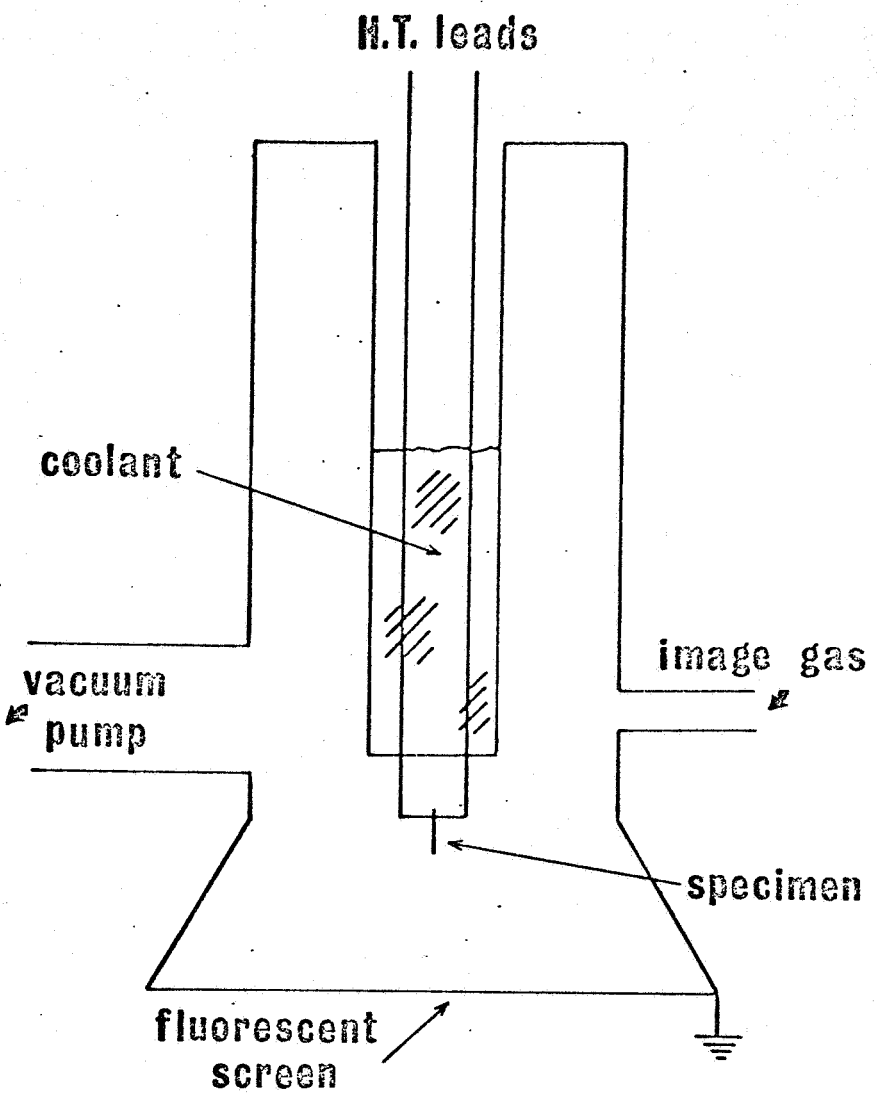

Figure 11.--Schematic drawing of a field ion microscope.

applied voltage and the radius of the specimen (Müller 1960, Gomer 1961), but is in the neighborhood of 10^8 to 10^9 volts/cm or about 5 volts/Å near the tip. This is equivalent to the removal of about one-third of an electron from each atom, and means that the "free electron cloud" is drawn back into the metal, exposing the positive ion cores on the surface.

A neutral atom of the imaging gas coming under the influence of the field around the tip becomes slightly polarized and acts as an oriented dipole. That is, the more weakly bound electrons are pulled toward one side of the atom causing it to act like a small magnet which then accelerates toward the specimen. When the polarized gas atom is a few tens of Angstroms away from the tip, the potential well of the atom is distorted by the presence at the potential field at the tip. Therefore, an electron in the atom no longer sees the symmetric potential well of the nucleus as in free space but, rather, as an asymmetric barrier that reaches a maximum and has a finite width on the side nearest the specimen.

According to wave mechanics, ionization is possible by tunneling of the electron through the potential barrier into the metal tip, provided there is an available energy level. This process is schematically illustrated in Figure 12. The resulting ion is then repelled by the

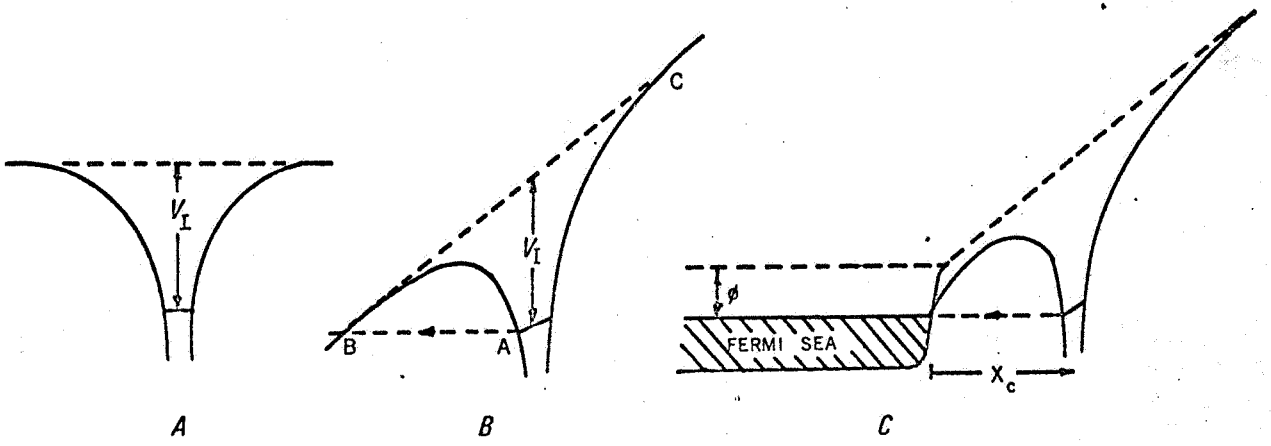

Figure 12.--Potential diagrams for an electron in field ionization. (a) the potential due to the parent ion in zero field; (b) in an applied field; (c) in an applied field near the surface of a metal of work function ϕ.

positive tip and travels along a trajectory (approximately elliptical) defined by the electrostatic lines of force to the screen. The field ion image is, therefore, a sensitive contour plot of the surface field distribution. Bright spots, corresponding to regions of high electric field (i.e., surface atom positions), give rise to a very regular spot pattern which can be interpreted directly in terms of the atomic lattice (Figure 13).

The current-voltage characteristic of the helium field ion microscope has the form shown in Figure 14 (Southon and Brandon 1963). A stable field ion image is formed in the region $\overline{BC}$ and the terminus of the curve at C corresponds to field evaporation of the specimen. At this point, the field at the surface of the specimen is sufficiently large to ionize and remove the loosely bound metal atoms on the surface. All too frequently, field evaporation occurs at a field lower than that required to obtain stable images. Thus, while field evaporation limits the materials capable of being studied in the field ion microscope, it is also the very process which makes the instrument unique by permitting three dimensional micro-dissection of the specimen. By controlled field evaporation of individual atoms from the surface of the specimen, the structure of the bulk can be deduced in atomic detail.

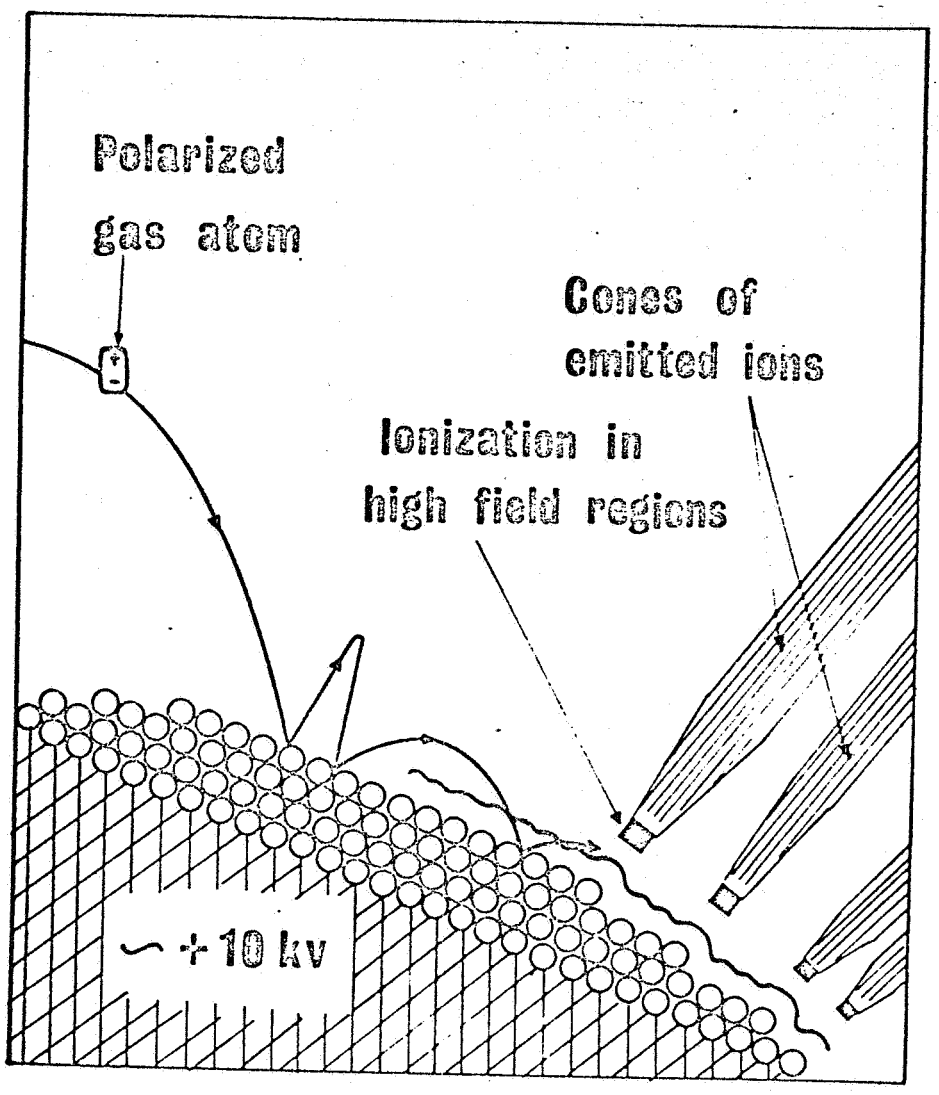

Figure 13.--Detailed schematic of the ionization process illustrating the relationship between the atom positions and the cones of emitted ions.

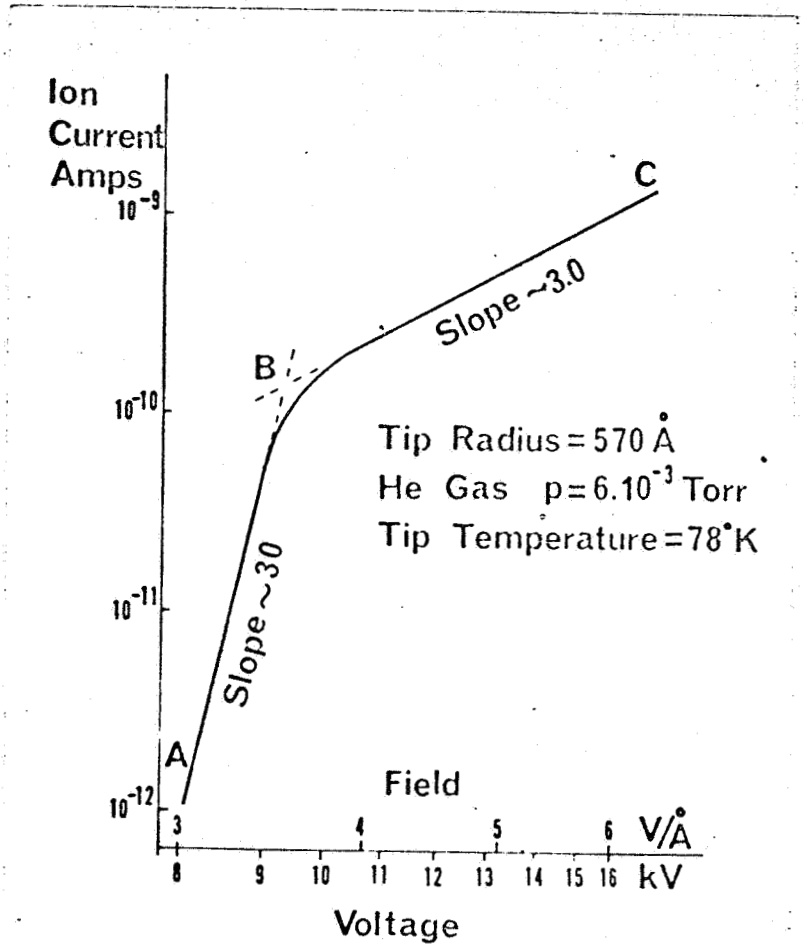

Figure 14.--Current-voltage characteristic of the helium field-ion microscope. (After Southon and Brandon 1963.)

Image Interpretation

Indexing

Normally, the first step to be taken when attempting to interpret a field ion image is to properly index the planes (or poles) on the micrograph. Although Müller (1960) has used an orthographic projection to index a micrograph, Brenner (1962) considers the stereographic projection to be a better approximation. More recently Brandon (1964) has shown experimentally that the true projection is somewhere between these two. It is possible to obtain a simple equation for accurately calculating the angles between poles on a field ion image (Newman *et al.* 1967) with the result that:

$$d = MR\theta \qquad (12)$$

where d is a linear distance measured on the micrograph, M is the combined magnification of the optics, R is the radius of the projection sphere, and θ is the inter-planar angle. This equation is derived and discussed in detail in Appendix I.

Computer Model

The computer model originally developed by Moore (1962) has been extended by Sanwald *et al.* (1966) to enable the interpretation of defects in the field ion image.

The image is simulated by plotting the positions of those atoms whose centers lie inside a thin spherical shell passing through a point lattice. The resulting array looks very similar in appearance to an actual field ion image. It is then a simple matter to introduce the strain field of a defect into the point lattice to determine its effect on the image. By adjusting the radius and thickness of the shell, and by varying the parameters associated with a particular defect (e.g., Burgers vector and habit plane for a loop), it is possible to obtain quite good agreement with experimental micrographs.

Defect Analysis

It has been proposed (Pashley 1965, Ranganathan 1966a) that a dislocation will appear as a spiral configuration in a field ion image. Furthermore, the exact nature of this configuration will be given by the scalar product $\vec{g}\cdot\vec{b}$ where $\vec{g}$ is a vector normal to the set of planes being disturbed by the emergence of the dislocation and $\vec{b}$ is the Burgers vector of that dislocation. It is worthwhile pointing out that $\vec{g}$ and $\vec{b}$ are geometrical in nature so the scalar product is simply a measure of the displacement component in the direction normal to the set of planes $\vec{g}$, (Figure 15). If one is consistent in using the correct plane notation (i.e., $\{hkl\}$ unmixed

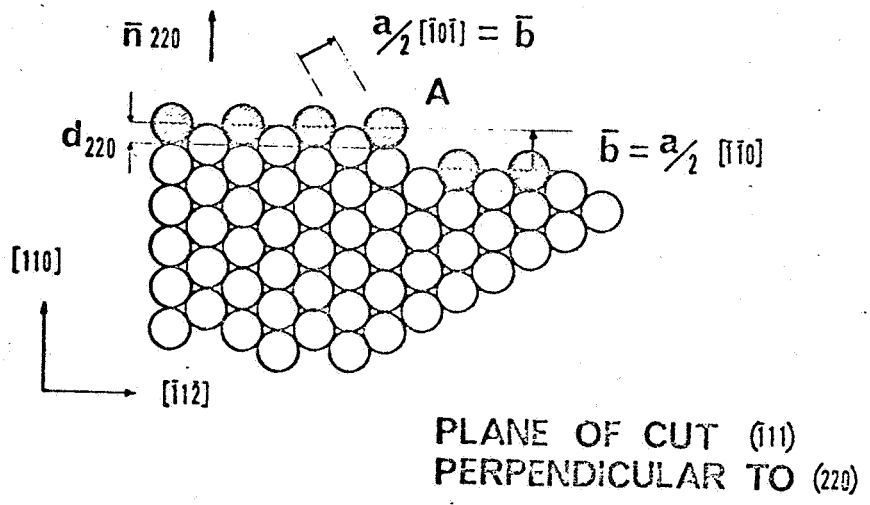

Figure 15.--Diagram of ($\bar{1}11$) plane showing how single and double spirals can be produced on (220) plane with Burgers vectors of a/2 [$\bar{1}0\bar{1}$] and a/2 [$\bar{1}\bar{1}0$], respectively.

for FCC, etc.), the dot product is an integer which determines the number of "leaves" in the spiral configuration, regardless of the dislocation character (i.e., edge or screw). Any dislocation, for example, with $\vec{b}$ = 1/2 [110]* intersecting the surface in the vicinity of a (204) pole will produce a single spiral as illustrated in Figure 16. The sense of the Burgers vector will determine the direction of rotation of the spiral for a given pole.

It is well known that one of the principle secondary defects formed after annealing a quenched specimen is the dislocation loop. It was mentioned in the section on electron microscopy that the dislocation loop is described by a single Burgers vector. It is implicit in this definition that the reference coordinate system move around the perimeter of the closed dislocation line to maintain consistency. However, it is impossible to distinguish it from a dislocation dipole (i.e., two individual dislocations with opposite Burgers vector) in an FIM image without a controlled field evaporation sequence. Provided there is no appreciable interaction between the strain fields, the two points of

---

*Defining both vectors in terms of lattice unit vectors i, j, k, the a-factor or lattice parameter term is not included in the Burgers vector notation.

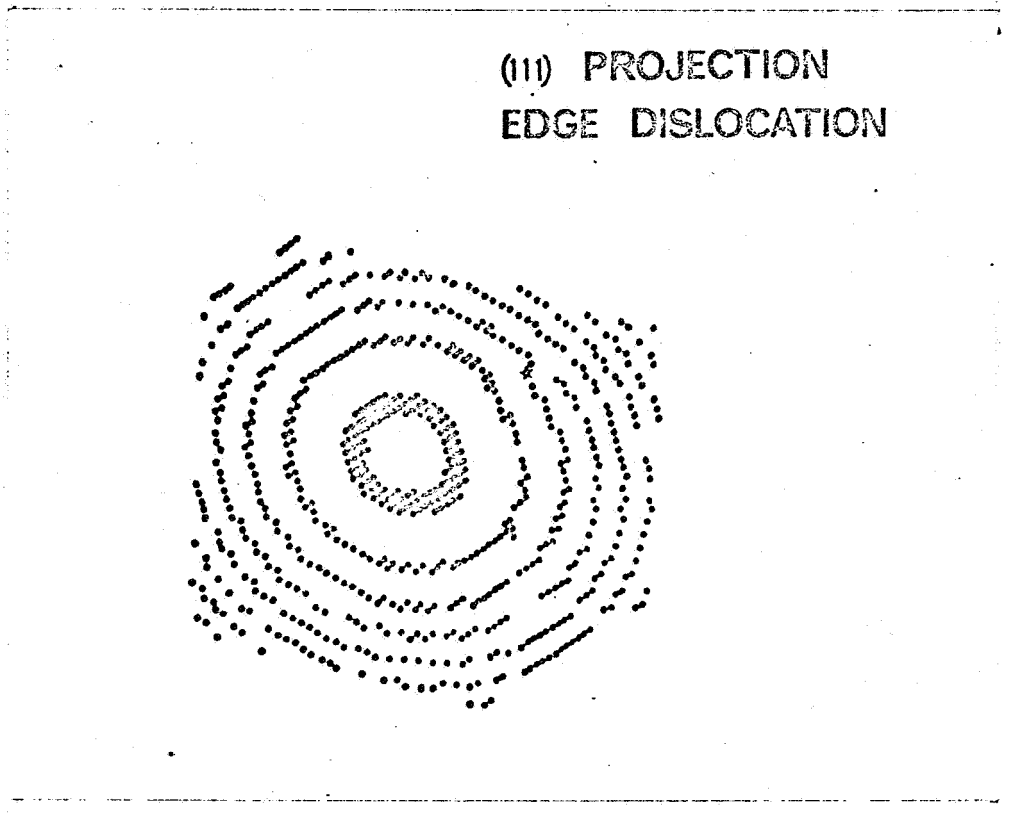

Figure 16.--Pure edge dislocation causing a single spiral on (204) plane edges.

emergence of the dislocations may be considered separately, with the result that the theory predicts spirals in opposite directions. Figure 17 illustrates possible configurations.

Single dislocations, dipoles, or total dislocation loops can be analyzed by inspection using the $\vec{g}\cdot\vec{b}$ criterion; at least the number possibilities can be reduced to a point where it is only necessary to determine the plane on which the dislocation lies in order to specify the Burgers vector. If the dislocation emerges at a point where two different sets of rings are disturbed (Figure 18), the spiral count will usually give a unique Burgers vector.

Loops bounded by partial dislocations present a different problem since $\vec{g}\cdot\vec{b}$ is not necessarily an integer. Partials have been found by computer analysis to cause various types of disturbances depending upon the location of the defect. For instance, high index planes appear to be split or sheared by the presence of a Frank loop, while a pinching type distortion occurs in low index regions of the field ion image. Thus, the $\vec{g}\cdot\vec{b}$ criterion does not seem to yield as much information for the case of partials. Hopefully, any obvious defect which cannot be interpreted in terms of total dislocations can be analyzed in terms of partial dislocations. For the case of a Frank loop, the bounding dislocation is a partial

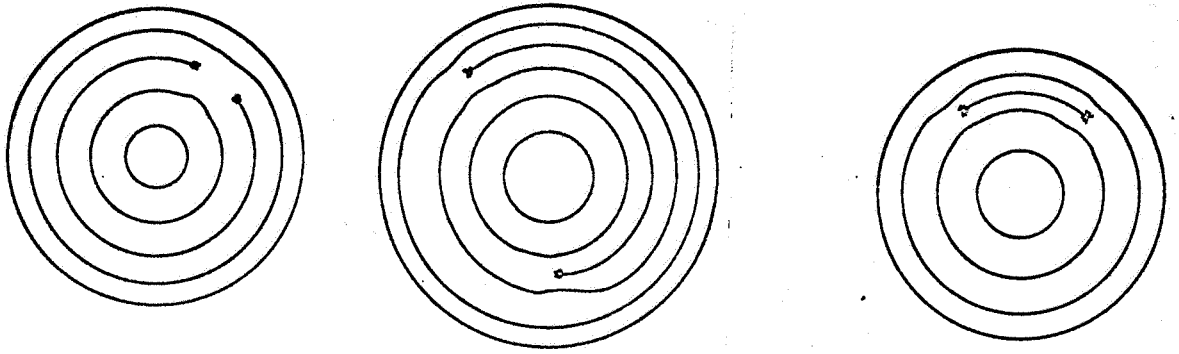

Figure 17.--Three possible spiral configurations resulting from the emergence of a dislocation loop. (a) Two dislocations, each producing a single spiral of opposite sense, yielding no long range effect. (b) Two dislocations equi-distant from pole, producing spirals of opposite sense. (c) Two dislocations producing spirals of opposite sense. Due to proximity of dislocations the effect is an extra plane segment.

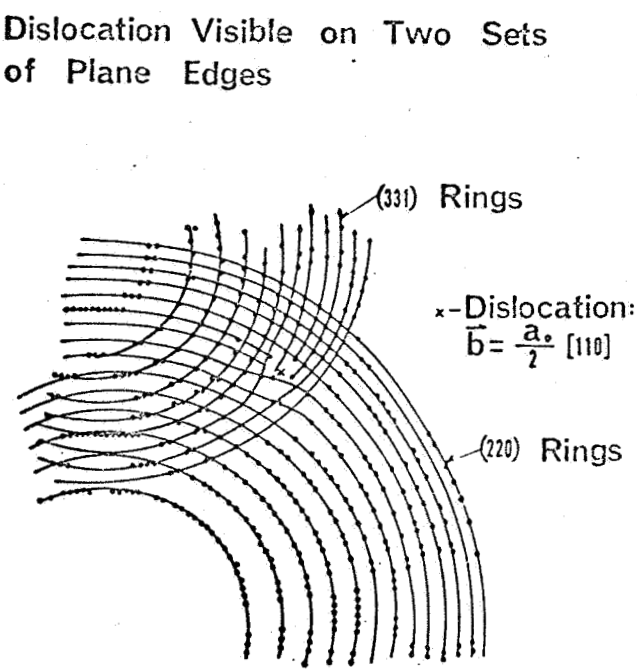

Figure 18.--Two sets of plane edges visible in the region of the defect. Note that $\vec{g} \cdot \vec{b}$ criterion is satisfied for each set of planes.

and $\vec{g}\cdot\vec{b}$ will normally predict a fraction of a spiral. Not only is this difficult to detect but it is also difficult to understand geometrically. Random choices of Frank loops which have been plotted by computer seem to indicate that streaks (Ranganathan *et al.* 1965) may form parallel to the fault plane. There is also evidence of ring distortion which is consistent with the concept of adding or removing a lattice plane to produce the fault.

Analysis of voids or large vacancy clusters is straightforward in that one must only determine size and shape. Polyhedral voids should be recognizable as such and should be amenable to geometric analysis employing the pseudo-stereographic projection mentioned above.

More complex defects, such as stacking fault tetrahedra and multilayer defects (Edington and West 1966), have not been considered to date, but should not present any particular difficulties since they are only dislocation arrays. It will probably be necessary to use computer analysis to determine their nature in the field ion image.

Effect of Stress

The applied electric field generates a hydrostatic tension, σ_N, normal to the surface of the specimen, given by Müller (1958a) as

$$\sigma_N = F^2/8\pi = 44.3\ F^2 \qquad (13)$$

where F is in volts/Å and σ_N is in kg/mm^2. A spherical specimen of an isotropic metal will experience a uniform dilitation and the shear stresses are therefore zero. For a hemispherical cap attached to a cylindrical shank, the tensile stress in the shank will be approximately σ_N, so that the maximum shear stress, τ, is given by:

$$\tau \simeq \sigma_N/2 \qquad (14)$$

These shear stresses are large enough to cause plastic deformation and may well be expected to have an effect on glissile dislocation configurations in the specimen. Unfortunately, it is not yet known whether there will be an increase or decrease in the probability of observing such a defect. The effect on sessile dislocations is equally uncertain but one would expect the hydrostatic component to aid motion by climb.

A cause for dislocation motion in the absence of a field is the force arising from the mirror dislocation outside the crystal (Cottrell 1953); an effect that can be quite important because of the small size of the crystal tip. Using equations developed by Bullough (1967), Hren (1967) has calculated this stress by treating the specimen as a stack of cylinders of decreasing radius.

The results indicate the equilibrium position for a screw dislocation to be along the specimen axis. The image forces will increase as the dislocation approaches the surface of the cylinder, but the increasing size of the successive cylinders makes it difficult to determine whether the entire dislocation will slip out of the crystal or whether it will reach a stable curved configuration, being "effectively pinned" at the wire axis somewhere up the shank (Figure 19). The superposition of the field stress can only confuse the issue further. In short, it is not known whether or not the sampling probability will be improved by the stresses on the tip.

Pimbley *et al.* (1966) have reported that the vacancy concentration in the {012} region of annealed platinum tips to be of the order of 10^{-2}, well above the 6×10^{-4} value Müller (1959) found in quenched platinum. The present author has observed a large number of single vacancies in platinum wire quenched from near the melting point and annealed at 500°C for 24 hours. Previous studies (Jackson 1965a) indicate that there should not be any appreciable quantity of isolated point defects after this treatment. It seems clear that these vacancies are stress induced artifacts as suggested by Pimbley *et al.*

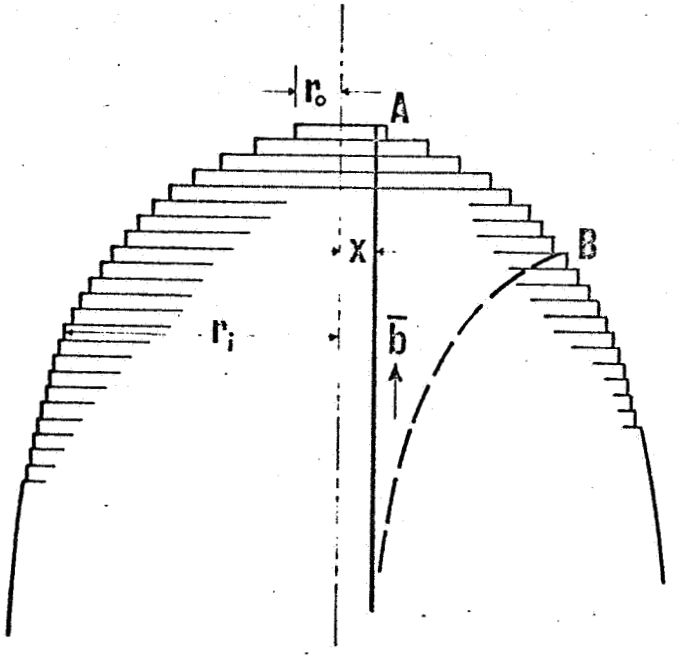

Figure 19.--Possible stable configuration for a dislocation line in a field ion specimen.

Thus, there is little doubt that stress effects can be important in field ion microscopy, and even though the stress distribution is not known, the possible results of such stresses must not be overlooked.

CHAPTER IV

EXPERIMENTAL EQUIPMENT AND PROCEDURE

The Field Ion Microscope

The basic design and operational characteristics of the field ion microscope were discussed in Chapter III. In this section further discussion will be limited to the instrument used in this investigation; a stainless steel, liquid hydrogen cooled microscope designed to operate in conjunction with an Air Products and Chemicals Inc. Cryo-Tip refrigerator. Design considerations for the construction of the microscope are discussed in Appendix II. A schematic drawing of the microscope is presented in Figure 20. As illustrated, the FIM body consists of an outer shell flanged at the bottom to mate with a 4" diameter viewing port and at the top to receive the flanged cryostat tube. The cryostat itself, is a Pyrex tube with two pairs of 0.050" tungsten wire leads at the bottom, and is graded to Kovar only 1-1/2" from the top flange to avoid any difficulty from low temperature phase transformations in the Kovar. Although the cryostat tubulation is designed for use with the Cryo-Tip, it may also be used by filling it with a cryogenic fluid. Suspended between the outer jacket and the glass cryostat is a stainless steel liquid

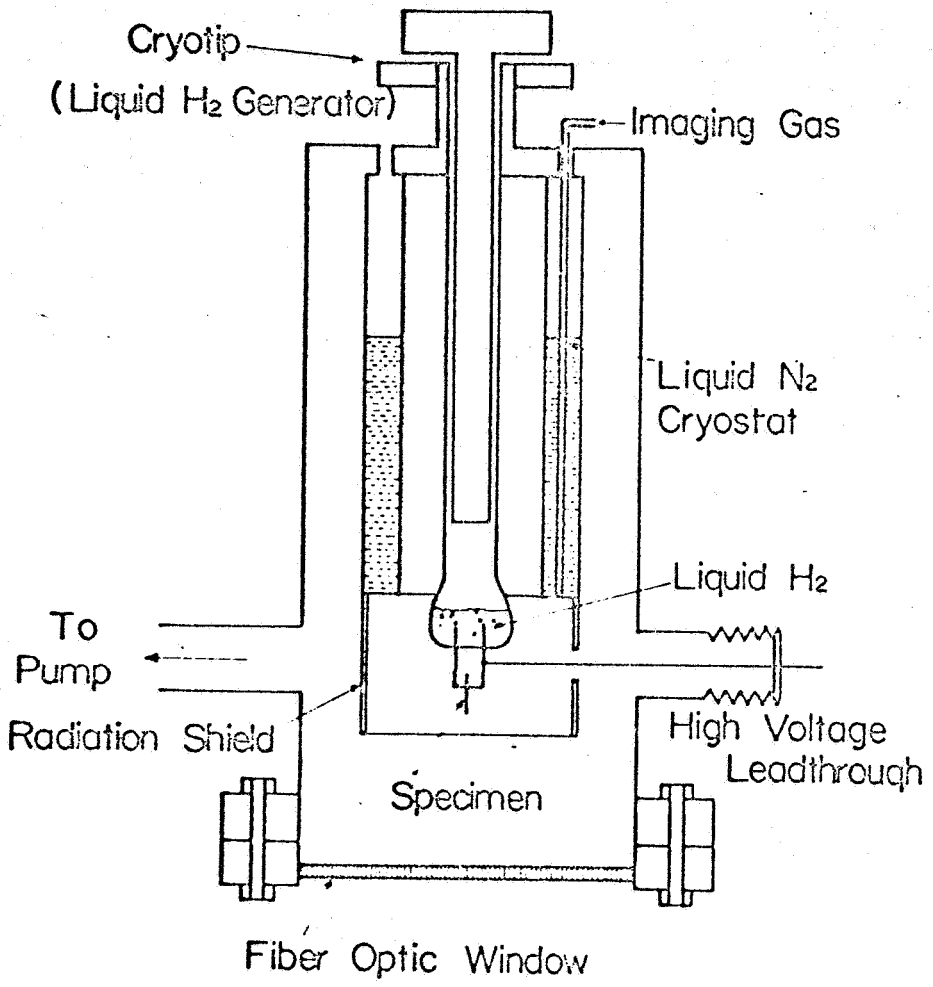

Figure 20.--Schematic drawing of the field ion microscope body. The microscope is constructed almost entirely of stainless steel, is designed for use at liquid hydrogen temperature, and incorporates a fiber optic viewing port.

nitrogen dewar which performs the dual role of radiation shield and cryopumping surface. To improve the shielding characteristics, the bottom of the dewar is made of copper, and an aluminum cylinder in thermal contact with the copper almost completely surrounds the specimen. Three 1-1/2" diameter ports extend radially from the specimen chamber (at specimen level) and are flanged to accept an ion gauge, a high voltage lead through, and a flexible bellows for making a connection to the vacuum system.

Normal photographic technique involves the use of high speed 35 mm film in specially fabricated camera bodies fitted with f/1 (or faster) lenses. However, this microscope has been fitted with a 4" diameter fiber optic faceplate permitting the use of direct contact photography, thereby eliminating the need for intermediate optics. This technique, its advantages and disadvantages are discussed extensively in the literature (Hren and Newman 1967).

The heart of the vacuum system (Figure 21) is a liquid nitrogen baffled 2" oil diffusion pump, backed by a 2 cfm fore pump. The system is capable of 10^{-8} mm Hg (without bakeout) within 1-1/2 hours of specimen change. Mild bakeout (300-400°C) results in pressures on the low end of the 10^{-9} scale of the ion gauge.

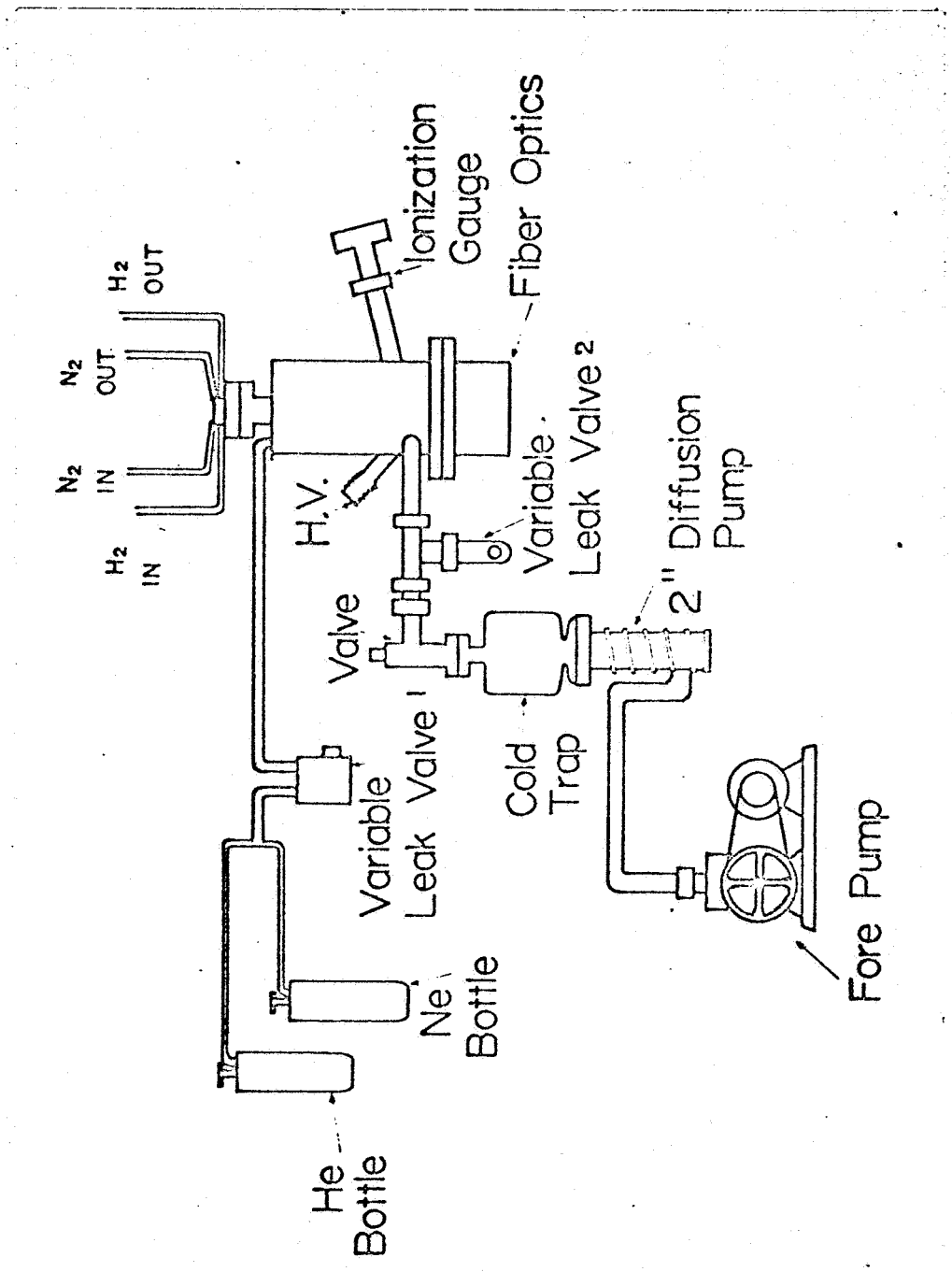

Figure 21.--Schematic drawing of the vacuum system for the field ion microscope.

The imaging gas system is presently set up to supply helium, neon, or a preset mixture of the two. The gas is bled in with the variable leak valve number 1 and then passes through the liquid nitrogen dewar into the specimen chamber. However, additional gases can be readily admitted to the system by means of the variable leak valve number 2. This is sometimes desirable for improving image quality in nonrefractory metals (Müller *et al.* 1965) or if one desires to study the effect of adsorbed gaseous impurities (Fortes and Ralph 1966).

The Electron Microscope

The electron microscope employed was a Philips EM 200 fitted with the new Goniometer Stage which permits full 360° rotation and ± 45° tilt of the specimen. In addition, a magnetic beam tilt device enables the operator to obtain high resolution dark field micrographs. The operating principle of the device is schematically illustrated in Figure 22 and the overall picture of the technique is illustrated in Figure 23. The normal operation of the microscope is as shown in (a); the incident beam makes an angle θ, the Bragg angle, with a set of diffracting planes in the crystal. The transmitted and diffracted beams intersect the Ewald sphere at reciprocal lattice points separated by the familiar

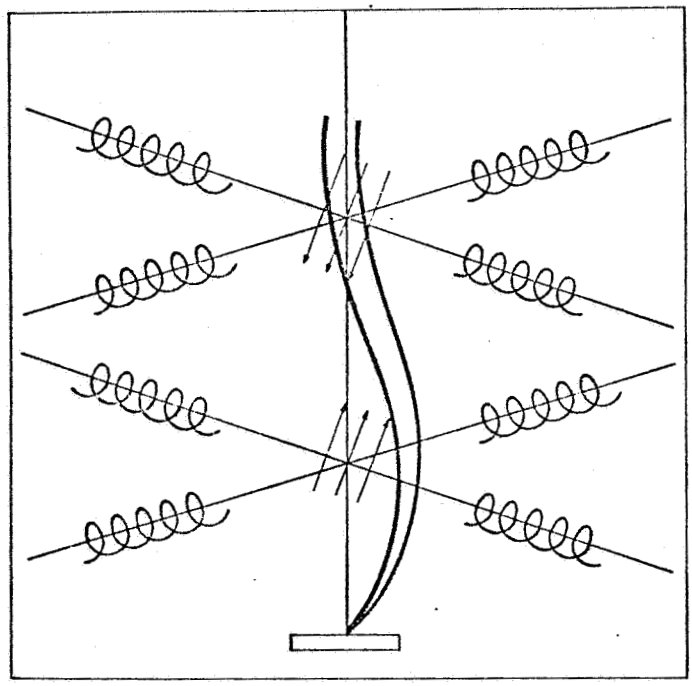

Figure 22.--Schematic illustration of the principle of operation of the magnetic beam tilt device.

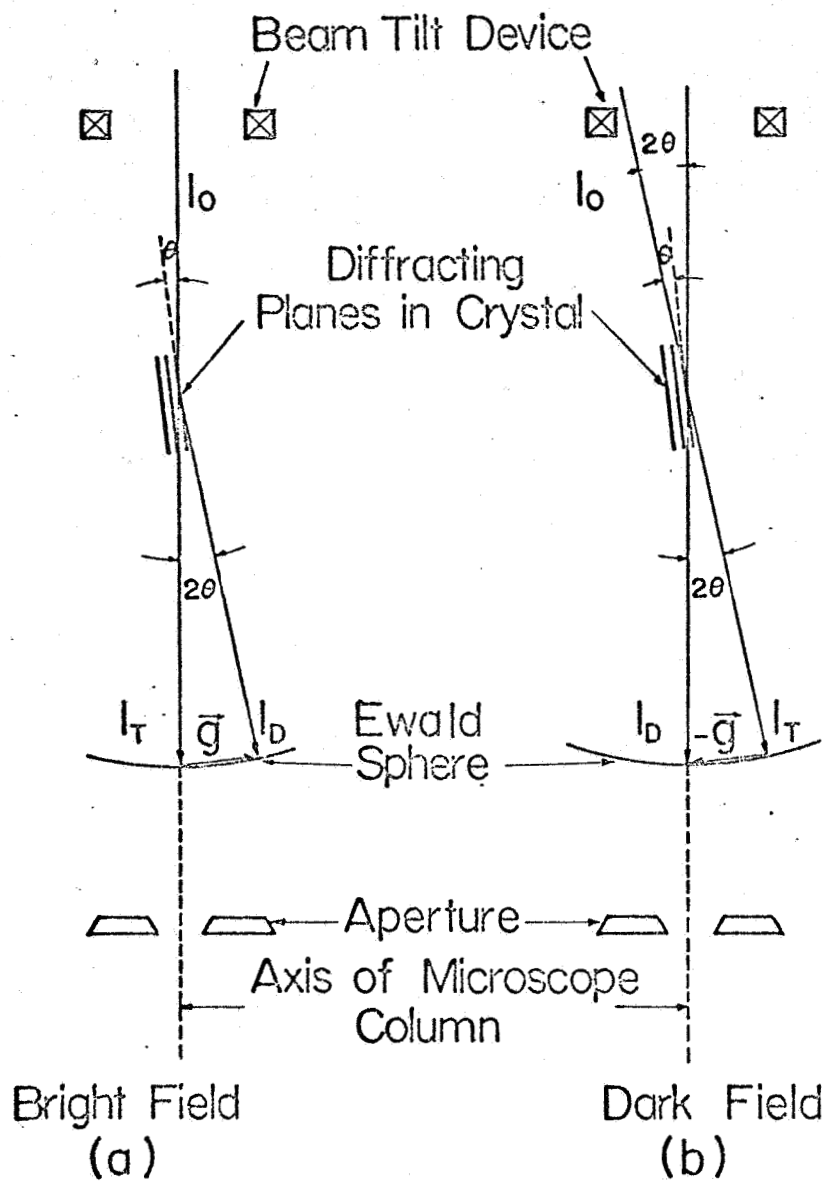

Figure 23.--Schematic drawing illustrating the principle of operation of the transmission electron microscope. (a) Operating under bright field conditions. (b) Operating under dark field conditions. (After Bell *et al.* 1965.)

vector $\vec{g}$. As mentioned earlier, the reflecting sphere (Ewald sphere) is almost planar for electron waves and coincides with the back focal plane of the objective lens of the microscope. Bright field images are obtained by inserting an aperture to eliminate all but the transmitted beam. Dark field images can be obtained by moving the aperture to allow passage of a selected diffracted beam but the spherical aberration of the magnetic lenses for any noncentral beam causes a great deal of astigmatism. As pointed out by Bell *et al.* (1965), to obtain a high quality dark field image from a strongly diffracting beam, the incident beam is tilted in the direction away from the operating reflection through an angle twice that of the Bragg angle. (For electrons, this is of the order of a few degrees.) Thus, the operating reflection in dark field is $-\vec{g}$. That is, the dark field image is actually due to reflection off the negative side of the planes which were favorably oriented for Bragg diffraction in bright field (Figure 23b). Without the magnetic beam tilt facility one must accomplish this tilt by reorienting the electron gun, an inconvenient operation at best, or be satisfied with an astigmatic image. A further advantage of the Philips device is that one can go from bright field to dark field with the flick of a switch. Because of the symmetry commonly found in electron diffraction patterns,

it is often possible to adjust the unit to permit a simple switching between bright field and either two or four consecutive dark field images.

The magnification and image rotation calibration data is presented in Appendix III.

Specimen Preparation

The platinum purchased from Englehard Industries was of 99.9% purity. Lengths of wire (6" × 0.005") and foil (6" × 1/4" × 0.0015") were heated electrically in air and quenched into brine at 0°C. The quenching temperature was estimated from two independent methods to be within 100°C of the melting point: (1) the voltage was increased until melting occurred in a dummy specimen and the remaining specimens were heated at approximately one volt less potential. (2) An optical pyrometer reading of 1680°C ± 50°C was obtained after correcting for emissivity and non-blackbody conditions. Short lengths were then cut from the original 6" length to be annealed for various times between 250°C and 600°C. No extensive table will be presented describing individual heat treatments, but instead, specimen history will be stated in the text as it applies to the overall discussion. The author feels that this is desirable in that the results are presented as general trends rather than as being due

to specific and/or involved quenching and annealing treatments.

Early in the investigation, field ion specimens were prepared from the wire by electropolishing in an aqueous potassium cyanide solution (Müller 1960). Sometime later, Dr. R. W. Balluffi informed us that his laboratory at Cornell had been successful in polishing platinum foils with an aqueous solution of calcium chloride maintained at -30°C (Ahlers and Balluffi 1967). This electrolyte was also found to work extremely well for preparing field ion specimens employing a platinum counter-electrode and a variable 0-15 volt A.C. power supply (Newman *et al.* 1967).

Electron transparent foils were initially prepared using the well-known window method, along with the above mentioned solution. Although satisfactory, an improved technique resulted from the persistence of Mr. E. J. Jenkins, the electron microscope technician. The method involves jet polishing a platinum disc that has been precut to fit the microscope specimen holder. The disc is placed on a platinum mesh screen and the cold $CaCl_2$ solution is allowed to flow in a small stream over the foil. A potential of 80-100 volts A.C. is impressed between the mesh and a platinum electrode immersed in the electrolyte

bath above the specimen. The apparatus is illustrated in Figure 24. This stage of the polishing procedure is continued until the center of the disc is noticeably thinner (i.e., "dimpled"). The final stage is carried out at 8-10 volts A.C. with the specimen immersed in the electrolyte bath until a hole appears. Large areas suitable for transmission microscopy are obtained in this manner. A final cleaning is accomplished by applying 20 volts D.C. for 30 seconds followed by a rinse in distilled water and then ethyl alcohol. The low temperature of the polishing solution insures that no annealing takes place during the preparation of the foil and the elimination of the need for stop-off lacquer reduces the occurrence of dirty foils.

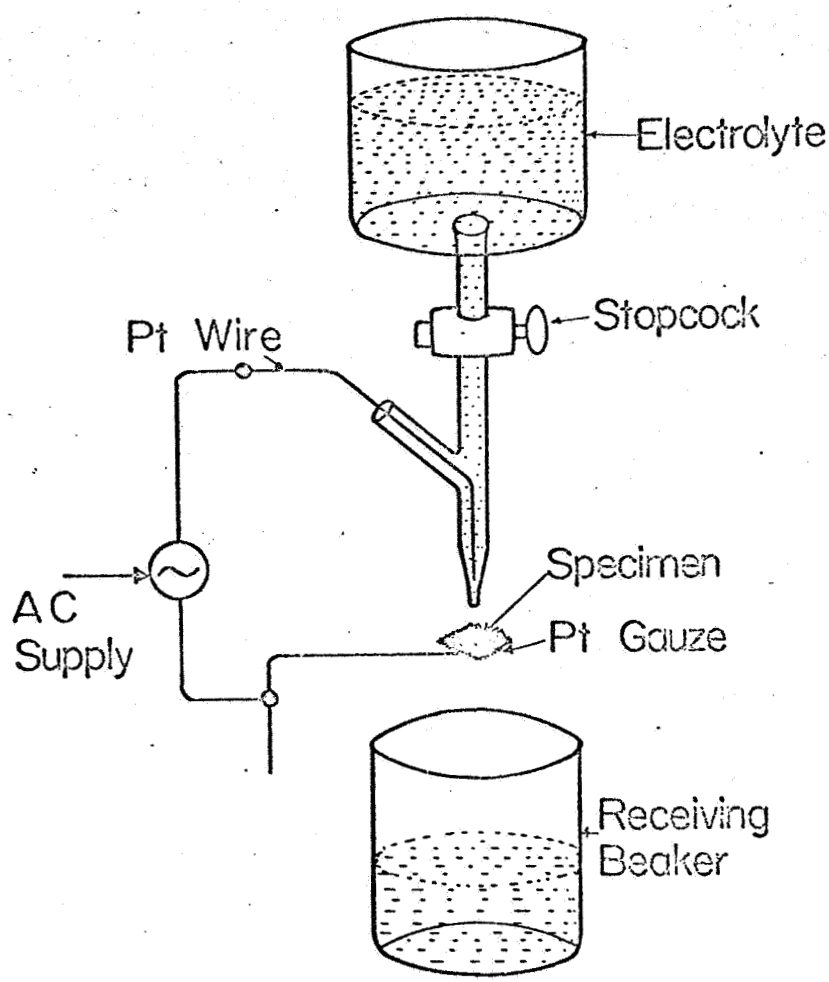

Figure 24.--Schematic drawing of apparatus employed for preparing electron transparent foils of platinum.

CHAPTER V

RESULTS AND DISCUSSION

Ruedl *et al.* (1962) found voids in heavily irradiated platinum foils upon pulse heating in the electron microscope, whereas irradiation followed by a mild anneal resulted in the formation of vacancy loops. Therefore, one might expect to find loops or voids depending upon the vacancy supersaturation. That is, it can be convincingly argued that an instantaneously high concentration of mobile vacancies would favor the formation of voids, while a lower vacancy concentration would favor prismatic loops. This is consistent with the present experimental observations in that either voids or loops are formed, but the two rarely occur in the same region. Furthermore, dislocations are almost nonexistent in areas of high void concentrations while large prismatic loops are generally found in the midst of heavily jogged dislocations. This is quite reasonable in light of the evidence for dislocations being efficient vacancy sinks. Thus, in some regions, small clusters and dislocations are competing for vacancies while in others, the clusters accumulate essentially all of the migrating point defects.

Void Analysis

A high concentration of large voids (cavities) was obtained by repeated pulse quenching in air followed by a one hour anneal at 500°C. Some of the cavities were more than 1000 Å in diameter, large enough to break through one or both surfaces of the foil, while the majority were of the order of 300 Å. This is in contrast to foils subjected to a single quench followed by a 24-hour anneal at 400°C. Under these circumstances the size distribution is more uniform and centered about a smaller diameter (i.e., 150 Å). Figure 25 is an electron micrograph of the pulse quenched and annealed foil after partial melting in the microscope. (This was accomplished by removing both condenser apertures while the specimen was under observation.) It is apparent that some voids are still present in areas within a micron of the melted edges, and it is thus reasonable to state that the void, once formed, is an extremely stable defect. This stability could well explain the presence of the large cavities in the pulse quenched specimen if one argues that the nuclei are formed during the first quench (a reasonable assumption since the air quench is relatively slow) and grow by vacancy absorption during each successive quench. This defect configuration is most likely the one contributing to the irreversible resistivity increment measured by Cízek (1967).

Figure 25.--Polyhedral voids in pulse quenched platinum foil after partial melting in the electron microscope. The average void size is approximately 300 Å.

Kiritani *et al.* (1964) have suggested that the voids in aluminum are regular octahedra with {111} faces, and a similar conclusion was drawn for the voids in gold (Yoshida *et al.* 1965). Clarebrough *et al.* (1967) have just published a rather complete study of voids in quenched copper, silver, and gold. (The author would like to acknowledge receipt of their manuscript prior to publication.) Although Clarebrough *et al.* found a few voids that closely approximated regular octahedra, the majority are better described as octahedra truncated by {111} and/or {100} and an occasional {110}. However, these voids were much larger and the authors concede that they may have been regular at smaller sizes. To remain as such after growth, the vacancy flux would have to be uniformly distributed over the surface of the defect.

The voids in platinum are definitely polyhedral in shape, but the facet configuration seems to be somewhat variable. By and large the resolvable voids can be described as {100} truncated octahedra (Figure 26) which, because of the associated strain fields, may appear spherical. On the other hand, there are instances where it is necessary to use more complex truncations involving only single sets of {100} as in (b) or {111} planes as in (d). Clarebrough *et al.* have suggested the truncations pictured in Figure 27.

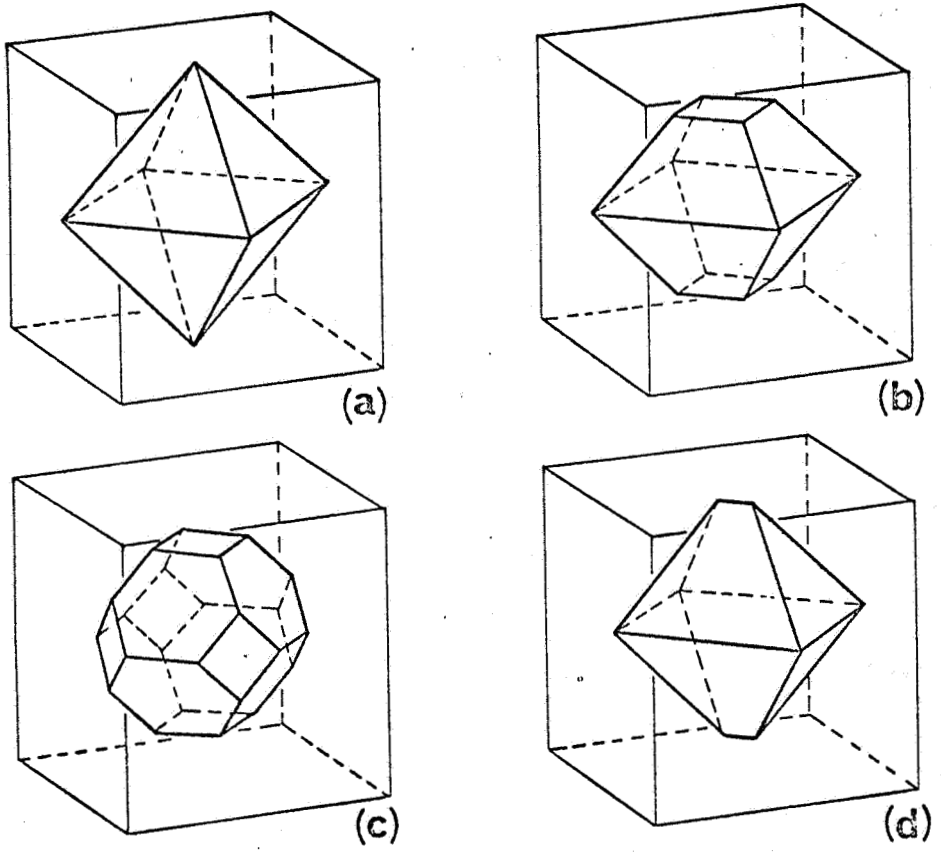

Figure 26.--Schematic drawing illustrating various void shapes. (a) Regular octahedron. (b) Octahedron singly truncated by {100} planes. (c) Octahedron multiply truncated by {100} planes. (d) Octahedron truncated by intersecting {111} planes.

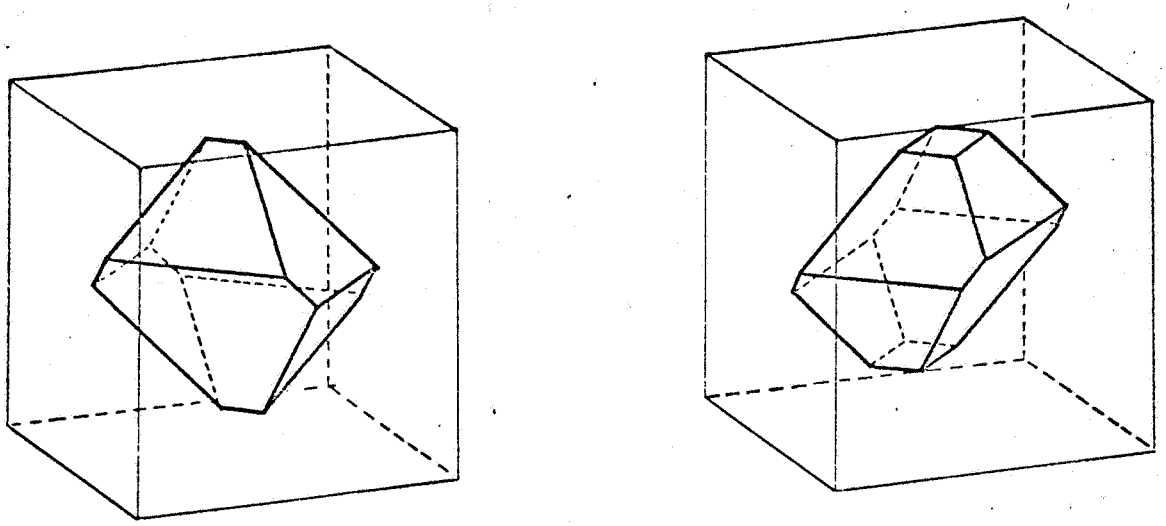

Figure 27.--Schematic drawing illustrating various void shapes. (a) Octahedron truncated by parallel {111} planes. (b) Octahedron truncated by parallel {111} and {100} planes. (After Clarebrough *et al.* (1967).)

Unfortunately, the analysis is not so straightforward for platinum since the voids are as much as an order of magnitude smaller than those observed in copper and aluminum, and the strain fields, although small, generally tend to obscure the boundaries of the defect. Figure 28 is a singular case where a clear fringe pattern was observed. It is postulated that the fringes (arrowed) occur as a consequence of the wedge-shaped nature of the defect. Only with low order reflections would the extinction distance be short enough to give rise to contours. Figure 29 is the same area with the defects exhibiting strain contrast. In agreement with the Ashby and Brown theory (1963a), the line of no contrast is normal to the operating $\vec{g}$-vector. Strain must also be responsible for the black patch contrast sometimes observed at various points within the confines of the void. Additional experimental evidence for the existence of a strain field around a void in platinum is presented in Figure 30. The dislocation line is apparently pinned at the void, and where the strain fields overlap, the perimeter of the void is invisible. Note that this void can also be seen in Figure 28 at the point X. Under these diffraction conditions the entire void is visible.

It can also be seen that the edges of the voids in these micrographs are parallel to projected <110> directions.

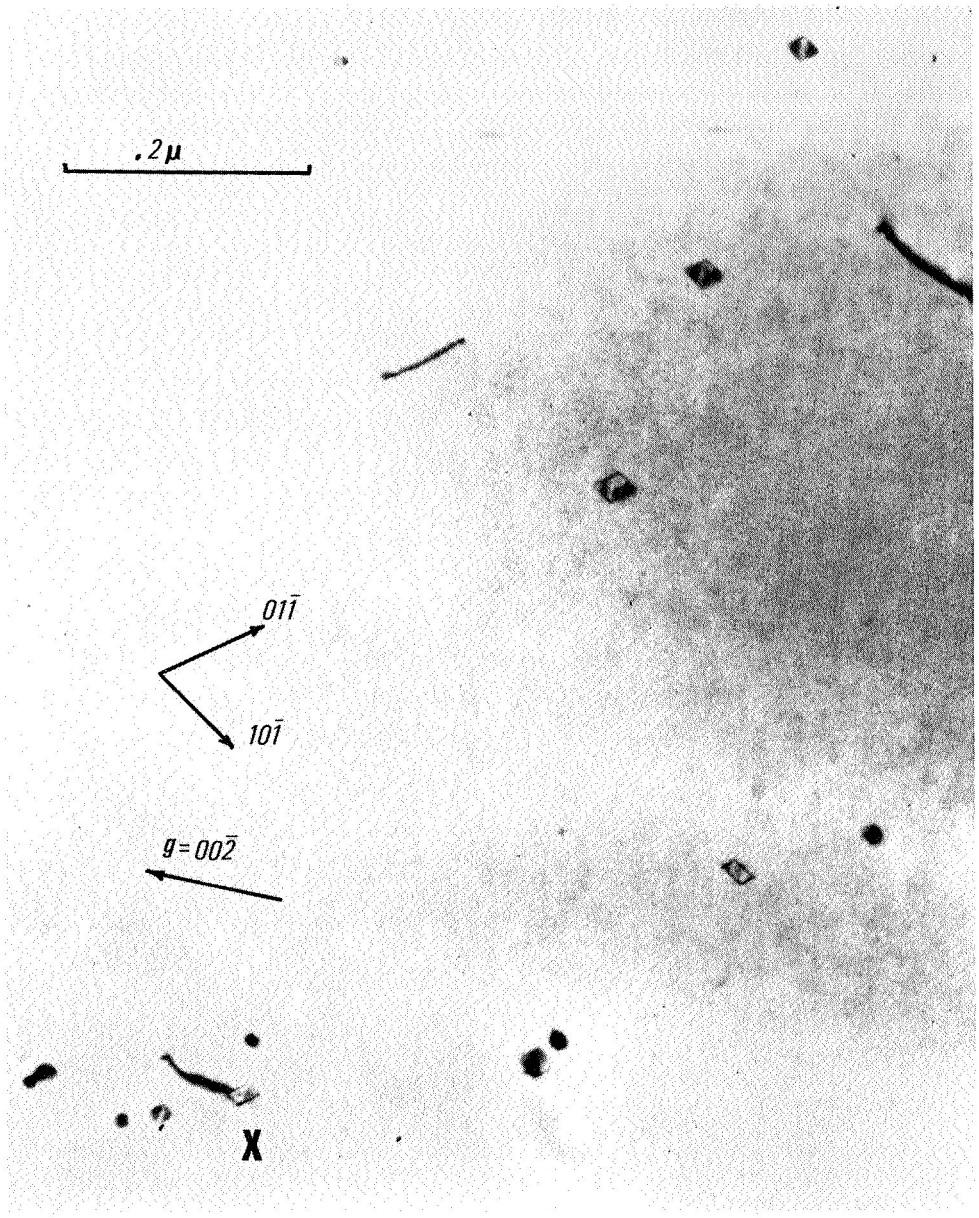

Figure 28.--Voids in platinum foil exhibiting fringe contrast. The specimen was quenched from near the melting point and annealed at 400°C for 24 hrs.

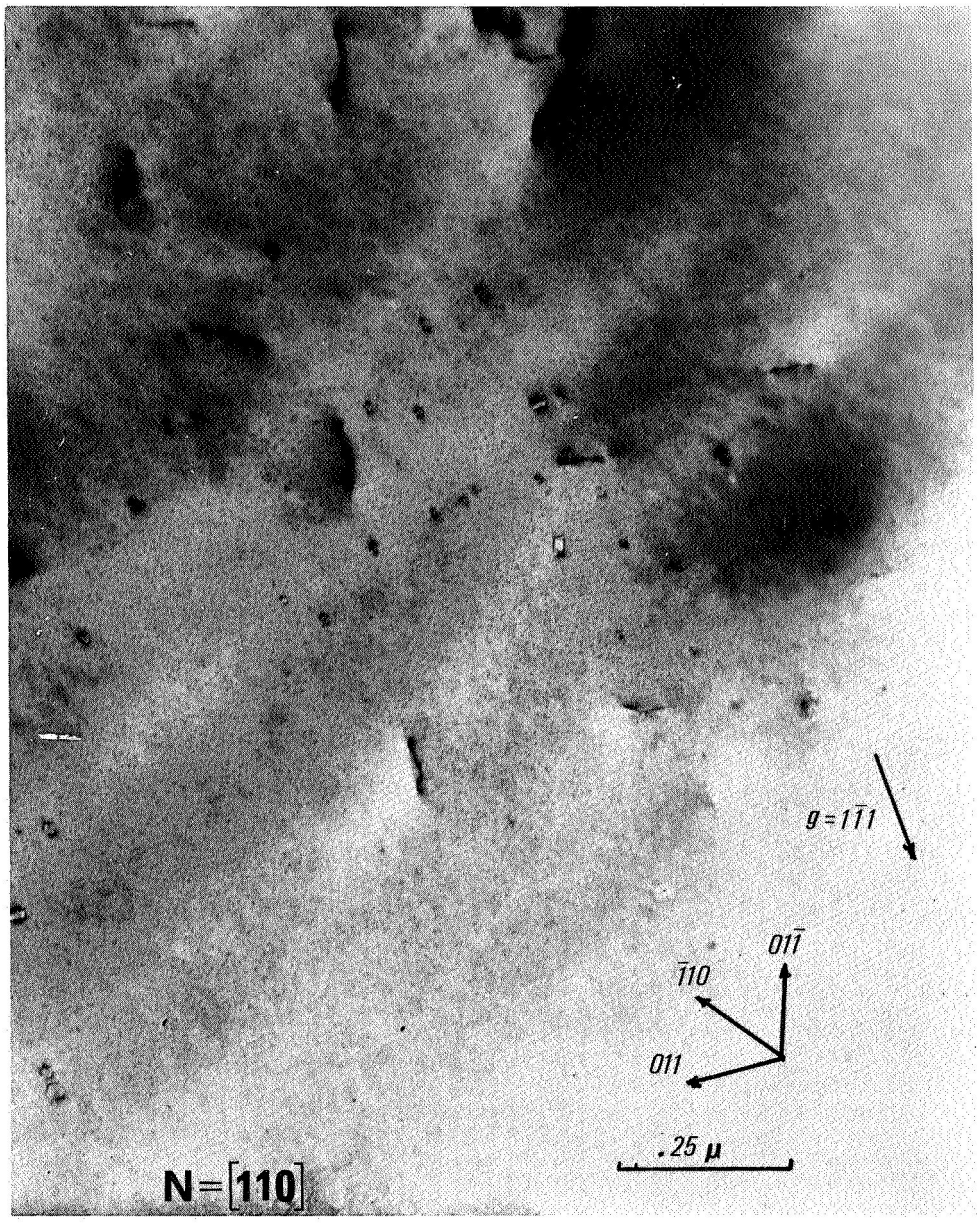

Figure 29.--Voids in the same platinum foil imaging by strain contrast. Note that the small voids which appeared as black spots in the previous figure can be recognized as hexagonal in cross section.

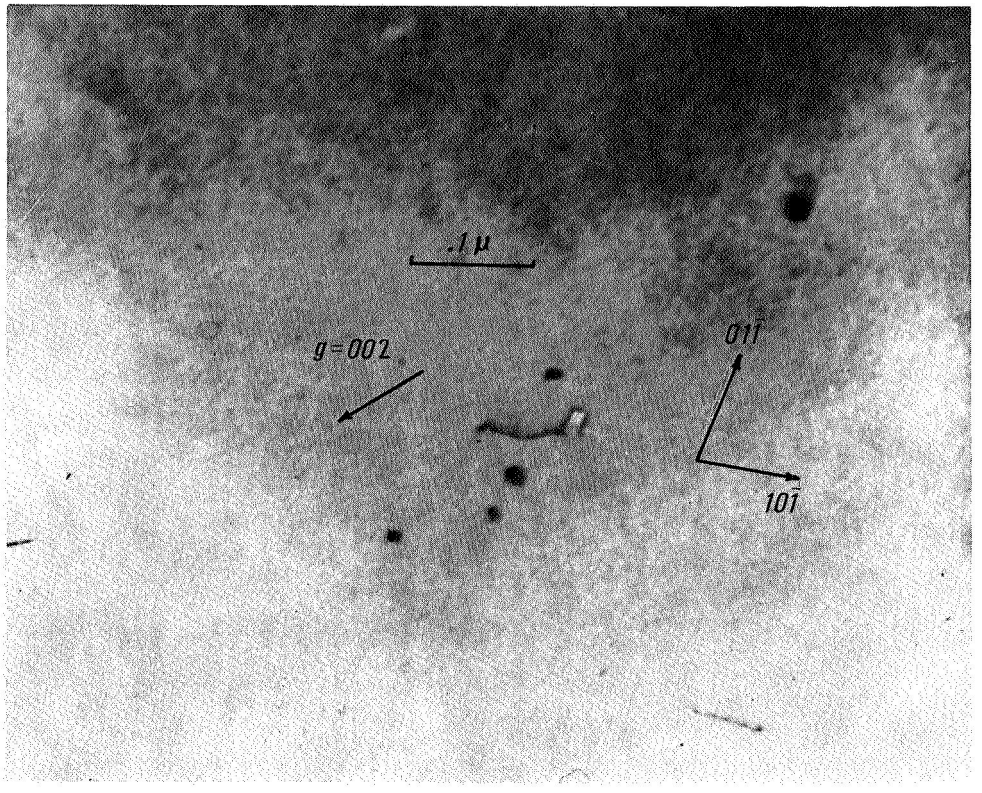

Figure 30.--Electron micrograph of a dislocation pinned at a void. The overlapping strain fields apparently cancel one another.

Initially this was misleading, for it was presumed that the rhomboidal defects were prismatic loops and that the hexagonal ones were Frank loops. However, they do not exhibit the behavior expected of dislocation loops. Making full use of the new Goniometer Stage obtained during the latter part of this investigation, tilting of the specimen through large angles revealed the three dimensional nature of the defects. Figures 31 and 32 illustrate quite well the negligible change in shape of the voids after 35° of tilt. Note, however, the marked difference in contrast between the two photographs. This is the type of behavior van Landuyt *et al.* predict for void contrast. The variables here for any one void are foil thickness, extinction distance, operating reflection, and excitation error $\vec{s}$. Although direct experimental evidence is lacking, one might speculate as to the reason for the string of voids at the top of the micrograph. The only logical explanation that comes to mind is that these particular cavities lie along a low angle boundary. Since the boundary would be a preferential sink for vacancies, this model would explain the relatively large size of these voids. The contrast behavior in bright and dark fields (Figures 33 and 34) indicates that these voids lie on the surface rather than on a line. That is, contrast reversal of some

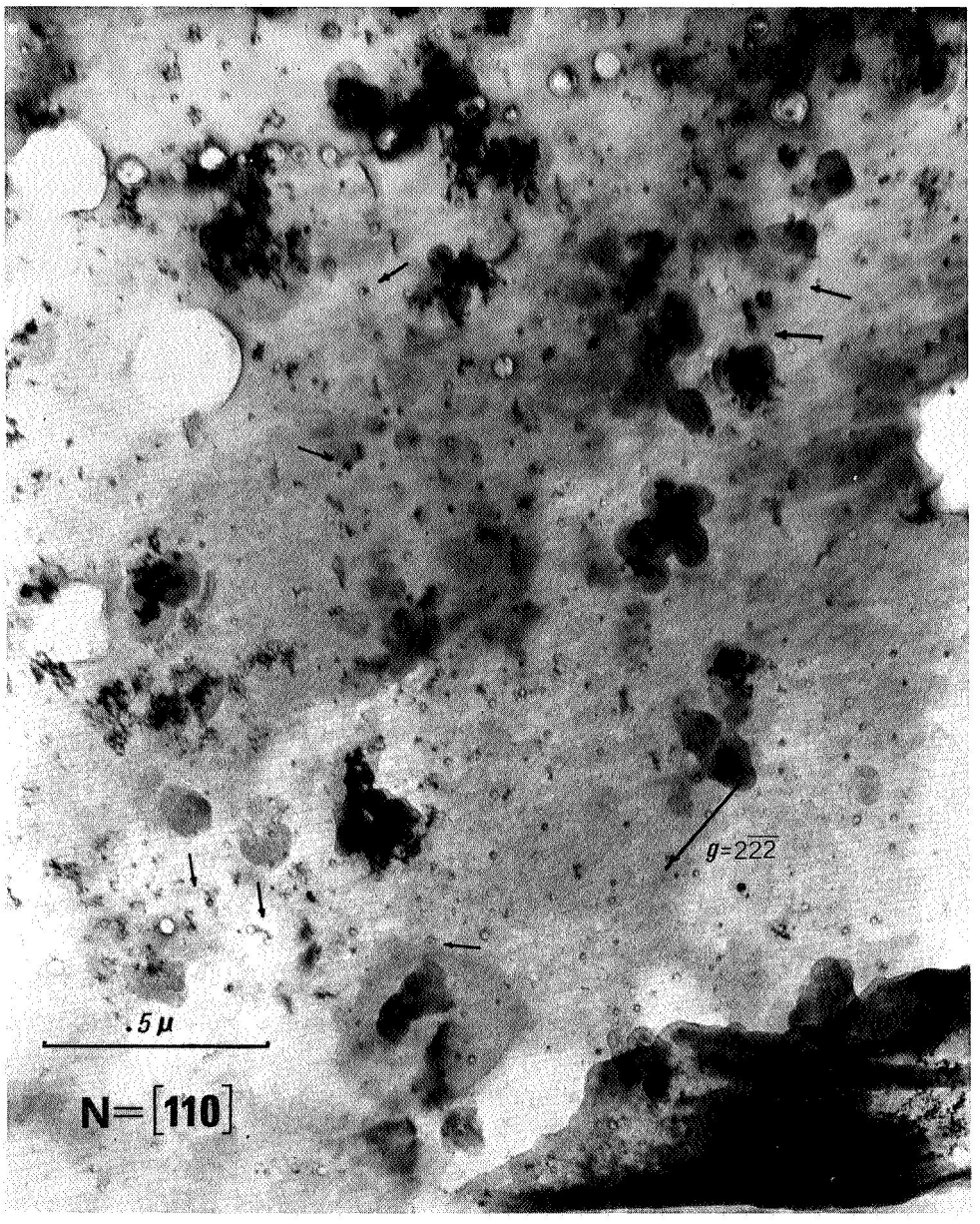

Figure 31.--Bright field electron micrograph of polyhedral voids in a [110] oriented foil. The specimen was annealed for 24 hours at 400°C. Void density is $7 \times 10^{14}/cm^3$, with an average diameter of 150 Å.

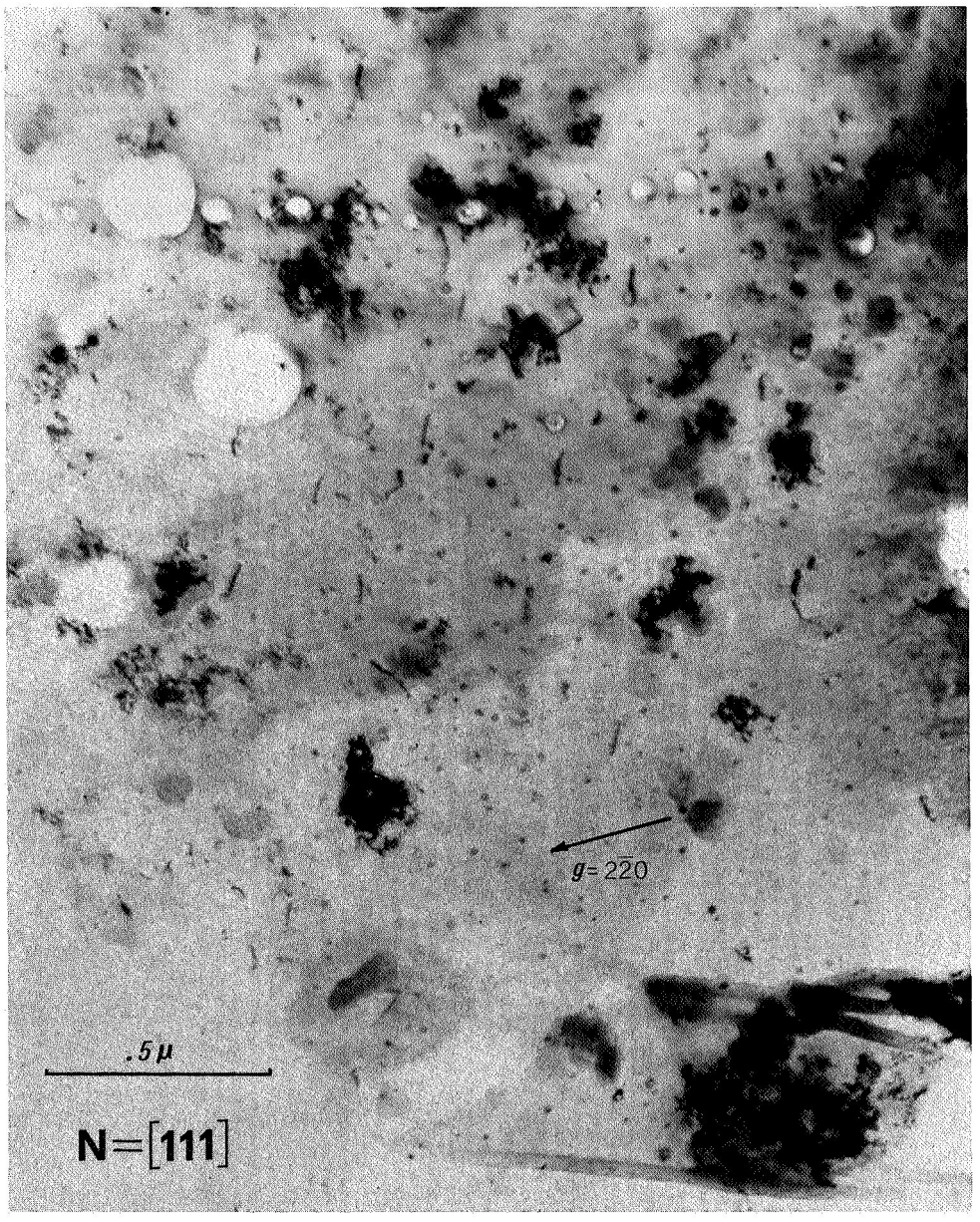

Figure 32.--Bright field micrograph of the same region after 35° tilt. New orientation is [111]. Although there is some change in contrast, the voids have not changed significantly in shape.

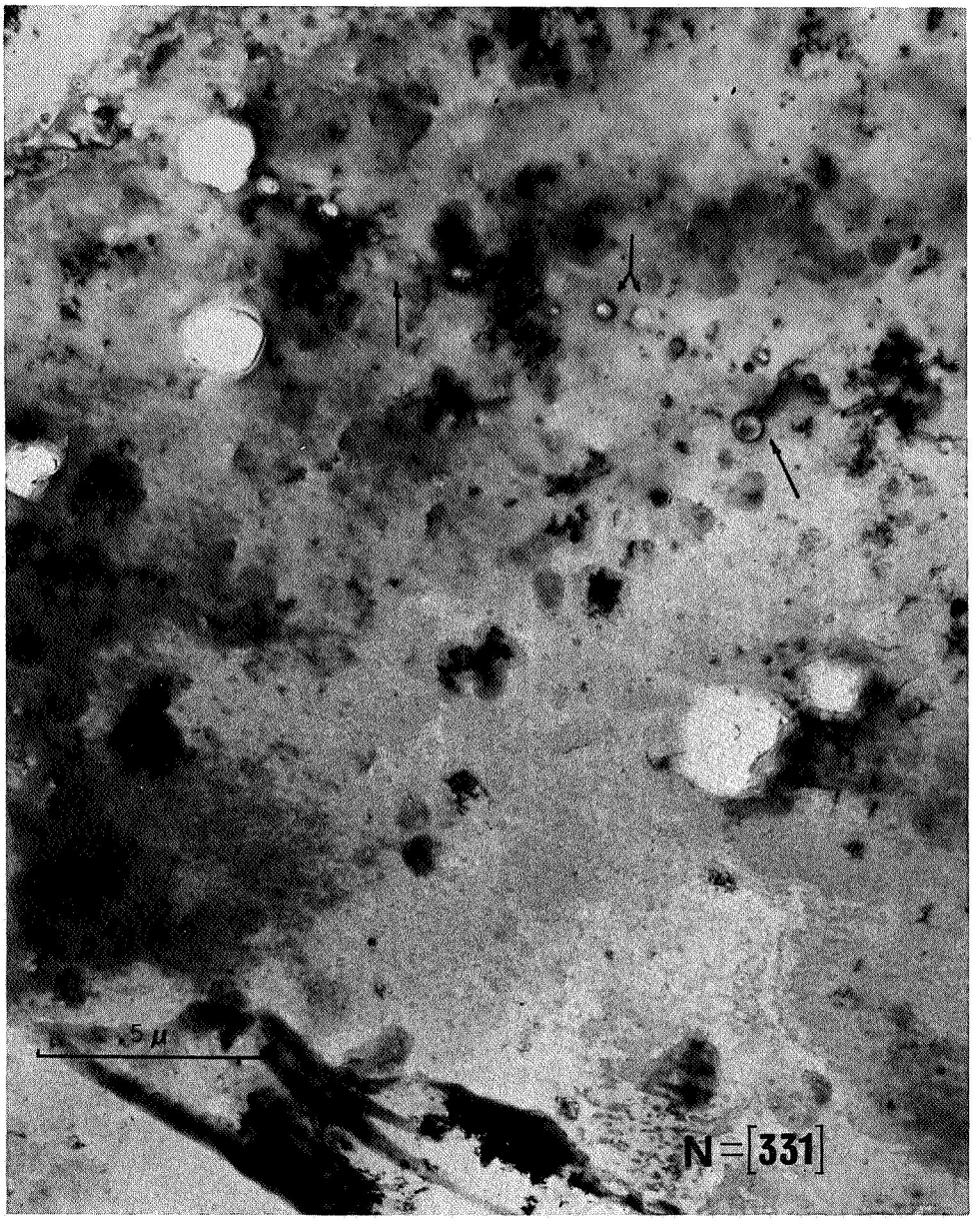

Figure 33.--Bright field micrograph of the same region after tilting to [331]. Many of the voids are seen only in residual contrast.

Figure 34.--Dark field micrograph of the same area illustrating the contrast behavior of the voids along the low angle boundary.

but not all of the defects means that they lie at different levels in the foil. Note also the increased contrast in the dark field image.

Other features of interest in these four micrographs are worth pointing out. Many of the voids, particularly in Figure 31, exhibit dark patches within the confines of the void. There are several instances of interaction between voids and dislocations, and there appears to be enhanced contrast at the point of contact. An extremely interesting feature which is quite difficult to explain is the contrast arising from the dislocation-void complexes along the low angle boundary.

Observations to date indicate that voids occur in all quenched specimens annealed between 250° and 600°C, with the highest density at 400°C after 24 hours. However, annealing at 500°C for 70-100 hours produces isolated colonies (one or two per specimen) containing a high density of large spherical voids (~ 300 Å) as shown in Figure 35. Almost without exception, the lower the concentration of voids, the more regular they appear (i.e., tending toward a simple octahedron). Figure 36 is such a void viewed along two crystallographic directions, [100] and [112]. The appearance of the void is in quite good agreement with what Kiritani *et al.* (1964) predict for an octahedral void in this orientation. Although not

Figure 35.--Isolated colony of voids in a foil that was annealed for 100 hours at 500°C. Average void diameter is 300 Å.

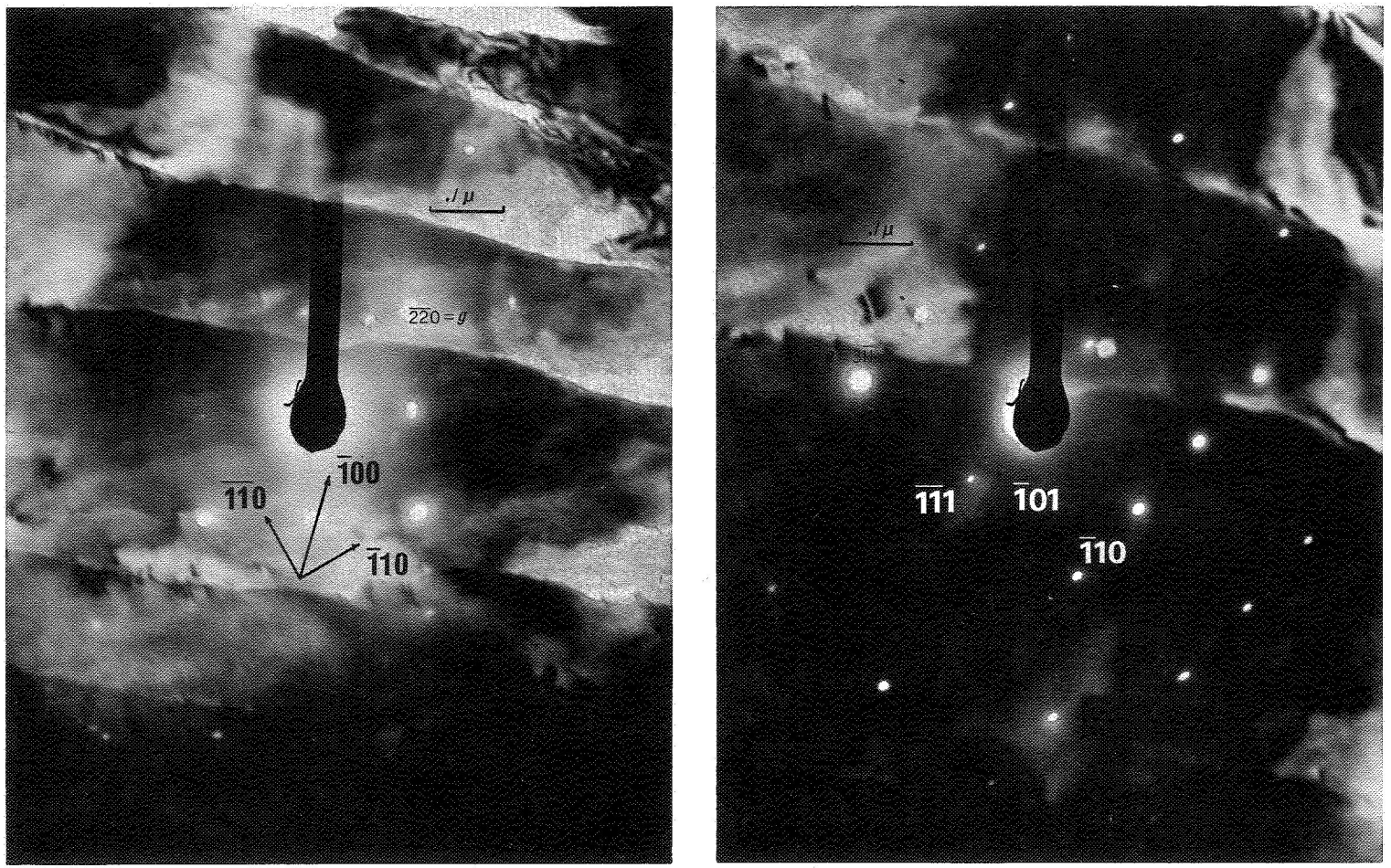

Figure 36.--An octahedral void viewed along two crystallographic directions. (a) Beam direction is [100]. (b) Beam direction is [112].

apparent in the micrograph, a small square was visible, under direct observation, at the "bottom" of the void in (a). This can be attributed to a {100} truncation of a regular octahedron as illustrated schematically in Figure 26. In general, the isolated, regular shaped voids are of the order of 300 Å.

While on the subject of void size, it would be appropriate to discuss the density of defects and the concentration of vacancies required to obtain this density. Estimating the foil thickness to be 1000 Å from the projected length of dislocation line, the void density is calculated as 7×10^{14} voids/cm^3. This figure does not take into account either the large cavities which extend through the foil or the ones that have formed along the low angle boundary. Taking an average void radius to be 80 Å, the volume fraction of void in Figure 31 is found to be 1.5×10^{-3}. Assuming the volume occupied by a vacancy cluster to be equal to the volume occupied by an atom cluster, we can estimate the retained (quenched-in) vacancy concentration at 1.5×10^{-3} which is in good agreement with the value given in Table 1. If the vacancy volume is assumed to be 0.25 of the atomic volume (Mukherjee 1966), the initial vacancy concentration would be 6×10^{-3}. Since there will be some relaxation, but not as much as at a single vacancy, a realistic value

is probably somewhere between these two. A value of 2.5×10^{-3} will be assumed. Each void requires approximately 2×10^{5} vacancies and therefore drains the matrix of all vacancies within a 500 Å radius. This calculation assumes that all voids are visible which, according to theory, is not necessarily true, nor does it include the very large voids. However, the number which are completely invisible will be quite small, not more than a few percent.

Studies involving various quenching atmospheres reveal a strong influence on void size and density (Clarebrough *et al.* 1967, Siedman 1967). No attempt was made to study the effect of quenching atmosphere in the present work, but it is entirely feasible that oxygen content could be a factor since the wires were heated in air. It is doubtful, however, that there would be enough gas present to account for the void concentration in Figure 31. Ruedl *et al.* (1962) explained the presence of voids in α-irradiated platinum as being due to accumulated helium gas which was certainly not present in this investigation. Furthermore, the void density in this specimen has been calculated at 10^{14} to $10^{15}/cm^{3}$, several orders of magnitude higher than that observed by Clarebrough *et al.*

There is a possible explanation for the rather high calculated vacancy concentration, which again brings

us to the problem of strain contrast. If the void strains the surrounding lattice and if the void images by some form of strain contrast, the size of the defect will be overestimated, since the strain must occur outside the actual cavity. If instead, the cavity is defined by the inner radius of the black circles, the vacancy concentration could be lower by as much as a factor of four. This estimate is in much better agreement with that in Table 1, but still does not account for the vacancies that are tied up in the larger voids.

The strain images of voids in platinum are strikingly similar to micrographs of internally oxidized Cu-Si slowly cooled to room temperature (Ashby and Brown 1963b); from this the authors calculate the strain to be approximately 10^{-3}. If it is then assumed that the strain in the platinum matrix due to the presence of the void is the same order of magnitude, an equation can be developed to approximate the surface energy of platinum.

Bullough (1967) has suggested that γ should be estimated from the equation for the internal energy of a void inclusion. If a sphere of radius r_o is removed from the matrix and the hole is allowed to shrink to a radius r', then the state of the strain is given by

$$u_r = \varepsilon \frac{r_o^3}{r^2} \qquad r \geq r_o$$

$$u_r = \varepsilon r \qquad r \leq r_o$$

where $\varepsilon = \dfrac{r' - r_o}{r_o}$ (15)

We are interested in the case for which $r = r_o$. In other words, we want to find the energy at the surface of the void. To find the self-energy of the void, we must evaluate the work done to form the void. Assuming linear elasticity theory to hold

$$E_1 = \frac{1}{2}\int_s \sigma_{rr} u_r ds \tag{16}$$

where, according to Bullough (1967),

$$\sigma_{rr} = 4\mu\varepsilon \tag{17}$$

where μ, the shear modulus, is given by Darling (1966) as 6.22×10^{11} dynes/cm^2. At the surface of the void (i.e., at $r = r_o$) σ_{rr} and u_r are constant, so that

$$E_1 = 2\mu r_o \varepsilon^2 \int_s ds \tag{18}$$

or

$$E_1 = 8\pi\mu r_o^3 \varepsilon^2 \tag{19}$$

Taking into account the surface energy of the void

$$E_2 = 4\pi r'^2\gamma = 4\pi r_o^2(1 + \varepsilon)^2\gamma$$

$$E_2 \simeq 4\pi r_o^2(1 + 2\varepsilon)\gamma \qquad (20)$$

Thus, the total energy of the void inclusion is the sum of these two parts:

$$E = 8\pi\mu r_o^3\varepsilon^2 + 4\pi r_o^2(1 + 2\varepsilon)\gamma \qquad (21)$$

Now since the energy is constant, $dE/d\varepsilon = 0$, and we find

$$\gamma = -2\mu r_o\varepsilon = -\frac{2\mu r'\varepsilon}{1 + \varepsilon} \qquad (22)$$

Substituting Darling's values for the elastic constants of platinum, recognizing that ε is negative because the matrix collapses, and assuming that $\varepsilon = 10^{-3}$,

$$\gamma = 6.25 \times 10^3 \text{ ergs/cm}^2$$

Thus, we find the value of the surface energy to agree with that of Blakely and Mykura (1962) to within a factor of two (i.e., $\gamma = 3 \times 10^3$ ergs/cm^2).

It has been suggested (Jackson 1962) that the surface energy of a small void should be evaluated in terms of the formation energy of the vacancies contained

in a defect and its surface area. It is interesting to note that a calculation of this type, assuming spherical voids, gives a value of the surface energy in good agreement with that obtained above for voids up to approximately 20 Å in diameter (i.e., of the order of 10^4 ergs/cm^2). For much larger voids, the value of γ becomes unreasonably high, and we must assume that the approximation is no longer valid.

Field ion microscope investigations may shed some light on this problem. Large polyhedral voids have not been found in field ion specimens, but small vacancy clusters have been observed with some frequency. Figure 37 illustrates two kinds of cluster configuration that have been encountered. The first is a rather disorganized cluster, whereas the second has a definite geometric shape. The straight edges can be indexed consistently with {111} planes, in which case the cluster can be interpreted as tetrahedral in nature. A field evaporation sequence through another void of this type (Figure 38) places its size in the neighborhood of 25 Å. Note that this defect would more than likely have appeared as a black spot in TEM. A larger void (~ 100 Å) appears in the last two photographs in this sequence. It has evidently reached a size level where it is no longer possible to retain the equilibrium configuration. In other

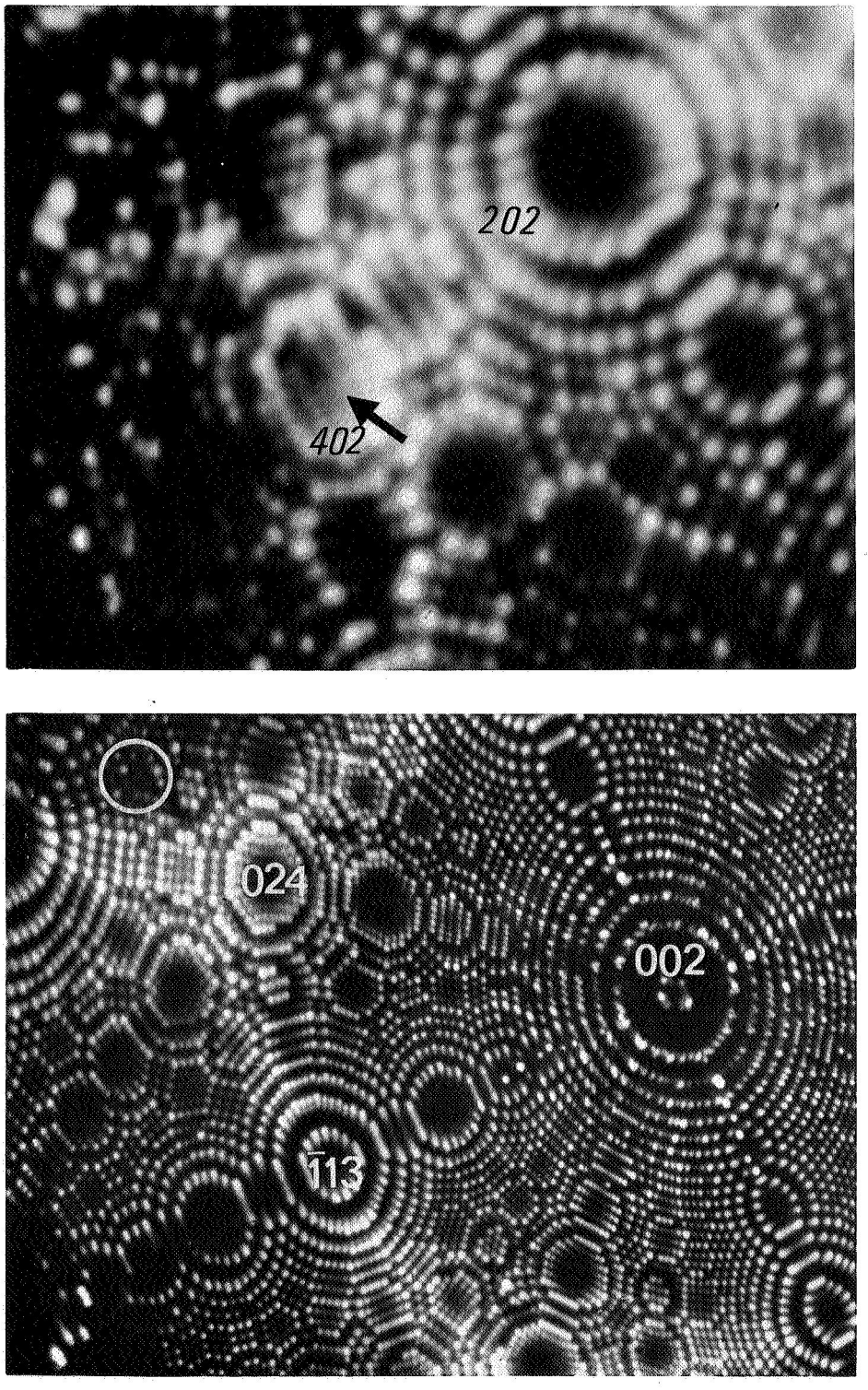

Figure 37.--Field ion micrographs of vacancy clusters in platinum. (a) An irregular cluster on a {420} plane. (b) A tetrahedral cluster near {220} plane. Both defects are about 25 Å in diameter.

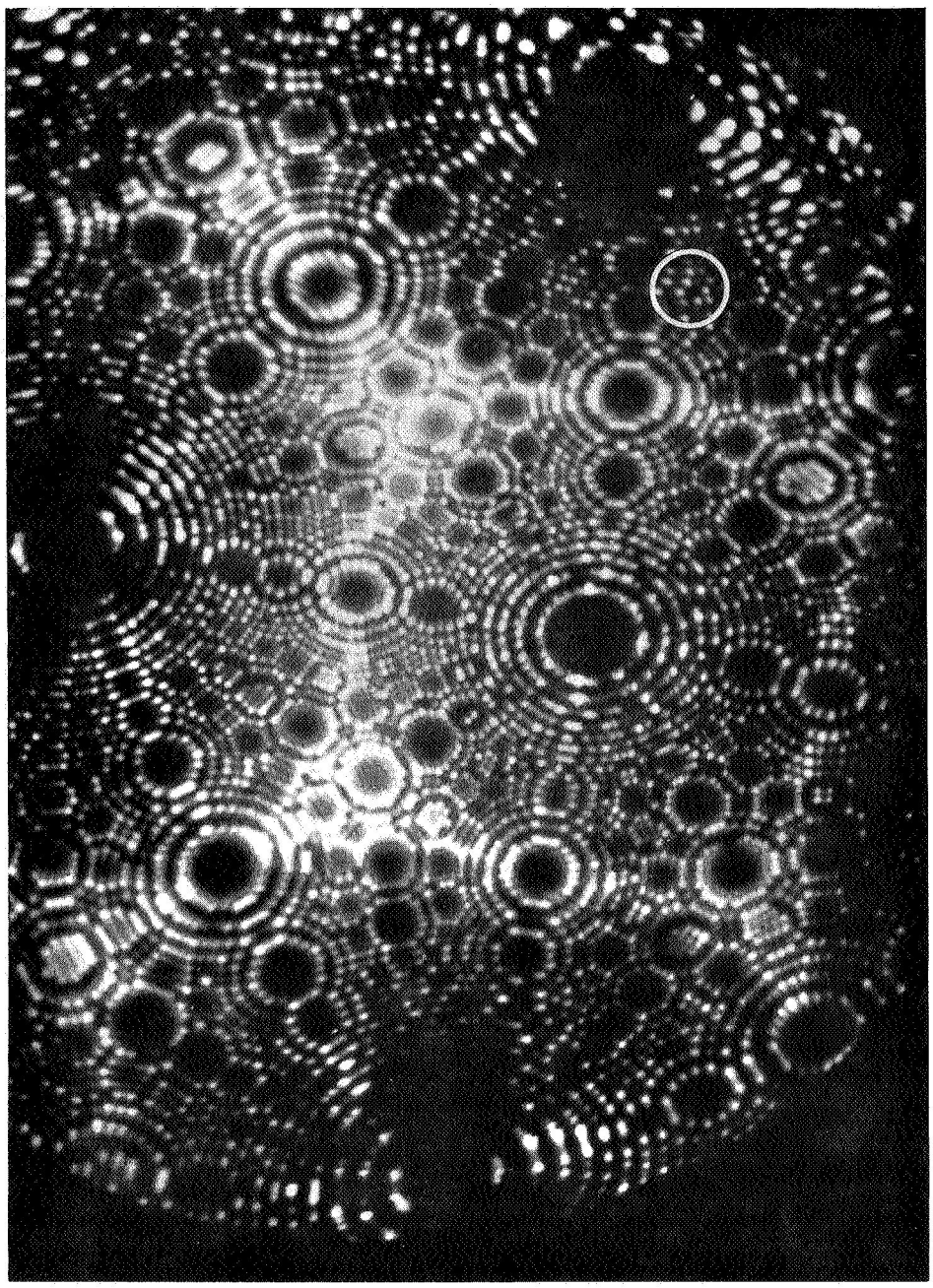

Figure 38.--A field evaporation sequence through a 25 Å diameter tetrahedral void near the ($\bar{2}24$) pole. (a) 240 layers into the specimen.

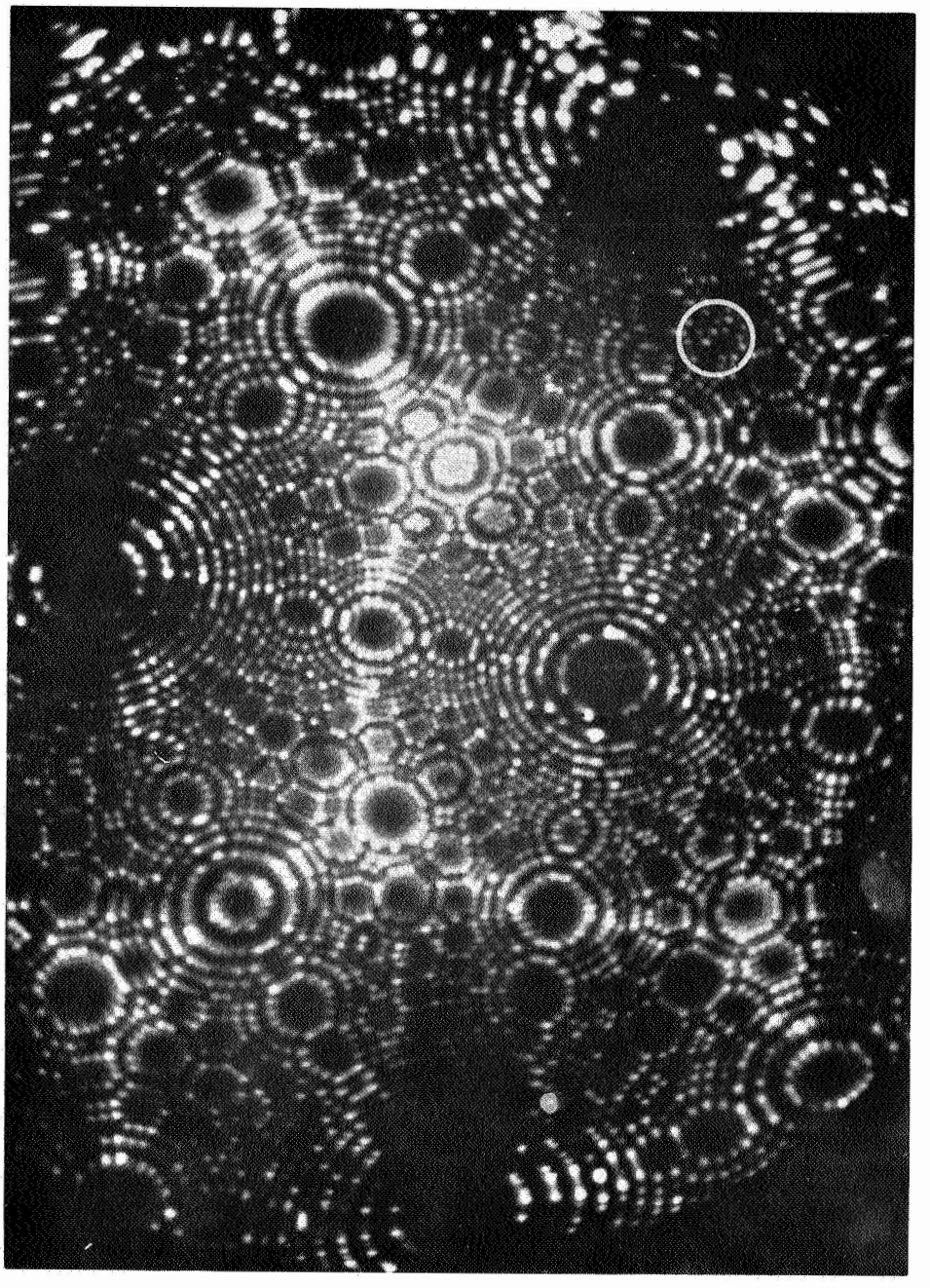

Figure 38.--(b) Same specimen after removing a single (002) plane. Note that the void is somewhat larger.

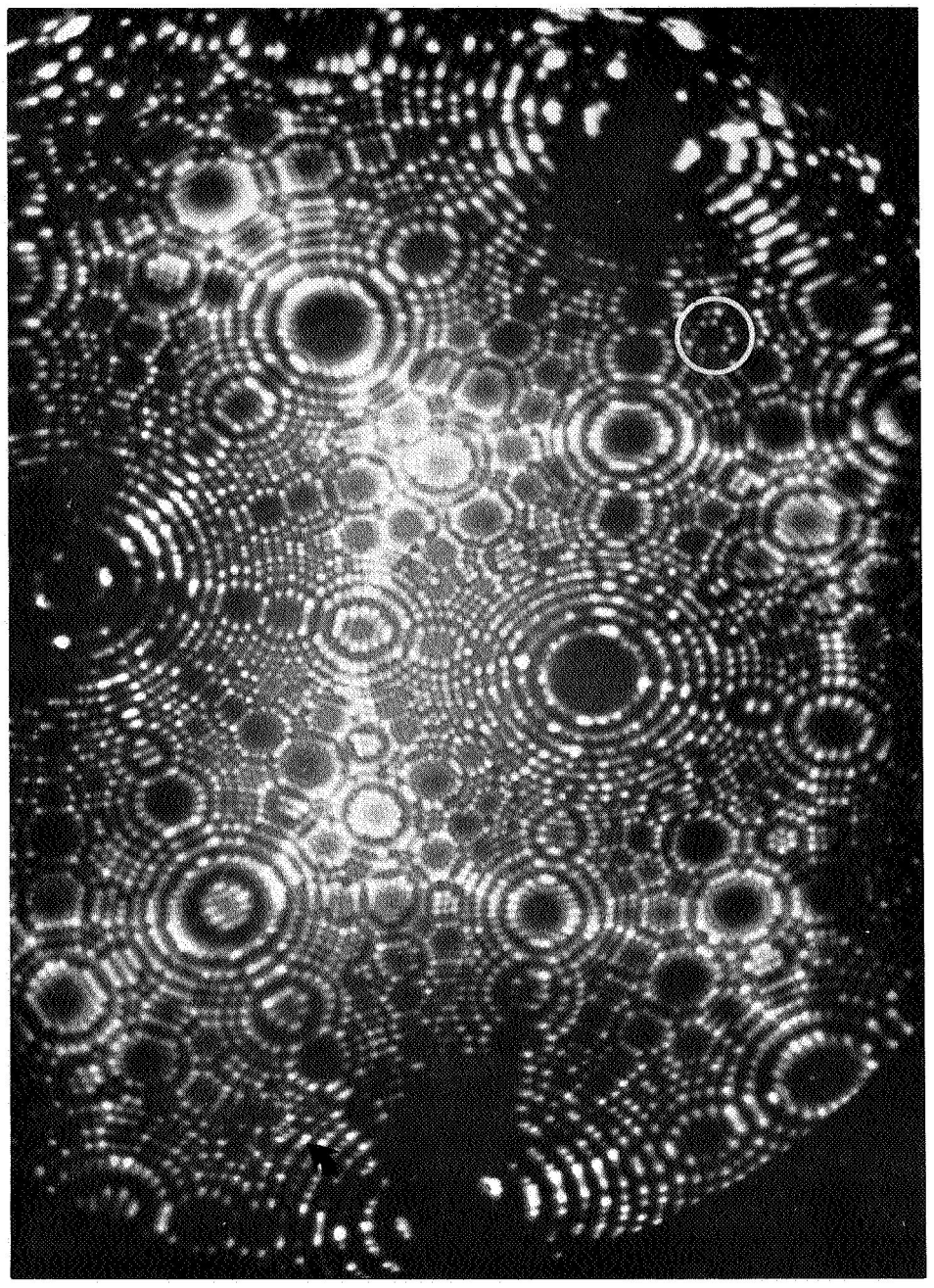

Figure 38.--(c) Same specimen after evaporating a second (002) plane. A large void has appeared near the [1$\bar{1}$1] pole.

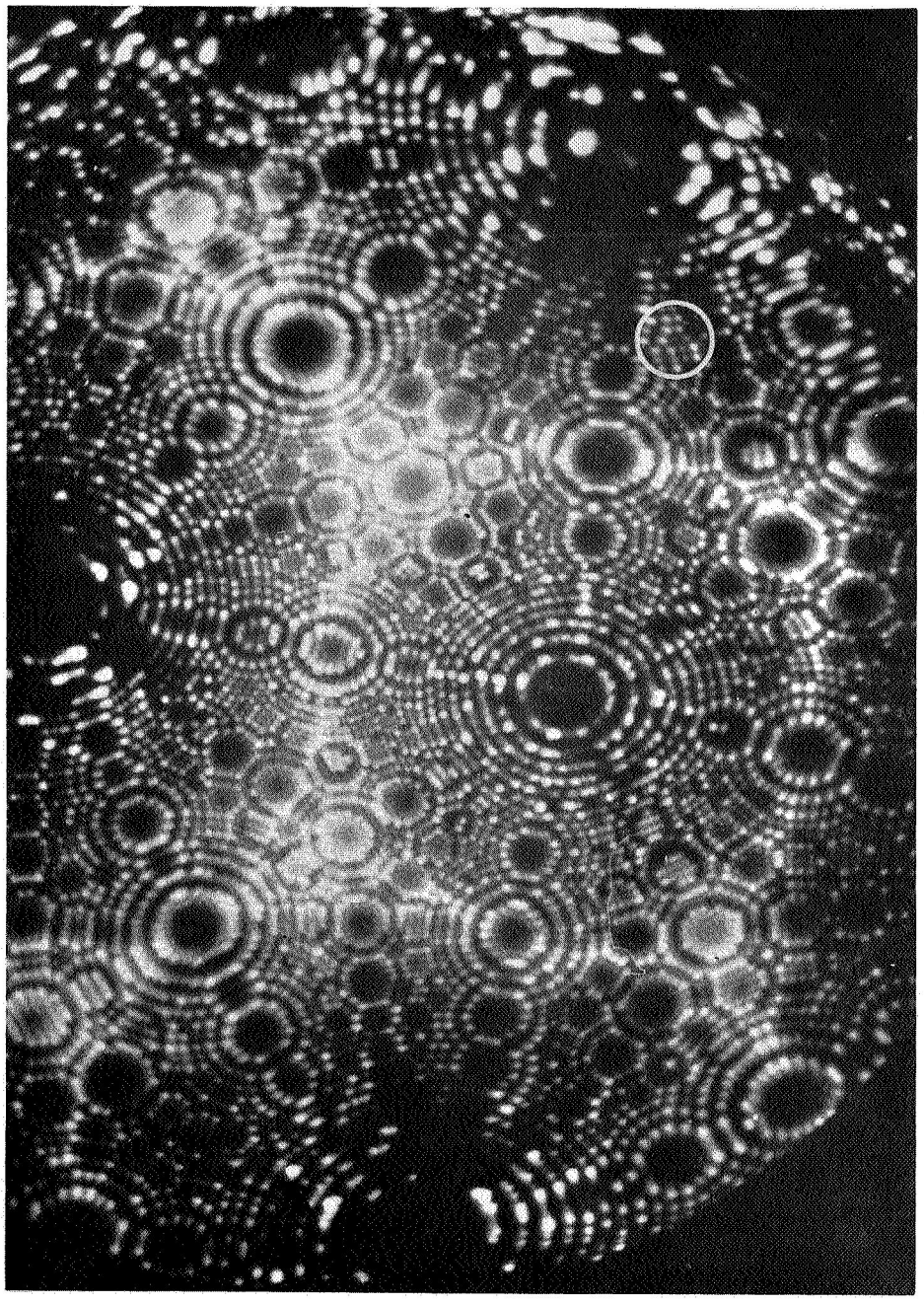

Figure 38.--(d) Same specimen after evaporating a third (002) plane. The void has decreased in size. The large void has become quite irregular.

words, the stresses have become so large that the matrix collapses when the void is intersected by the surface, and preferential field evaporation occurs. It may be that the imaging stresses inherent in the field ion microscope will prove a disadvantage when one is studying large cavities. Images of irradiated tungsten and iridium always display irregular cavities and one wonders if the irregularity is real.

There is a region of uncertainty but it seems clear that the nuclei for the polyhedral voids observed with TEM are tetrahedral, and remain so shaped up to at least 25 Å diameter. In the vicinity of 100 Å diameter, the defects become polyhedral, i.e., truncated octahedra. This transformation requires that the void increase, by a factor of two, its {111} type surfaces by a mechanism which cannot be easily explained. However, Figure 39 is a sketch of the relation between a tetrahedron and an octahedron. Suitable {111} truncation of the tetrahedron at the four apices will transform the shape into an octahedron, a process which can occur either by atomic migration over the inner surface of the void or a change in the growth pattern as vacancies are absorbed. If it is assumed that the surface energy plays a major role, then the size at which the transition occurs may well

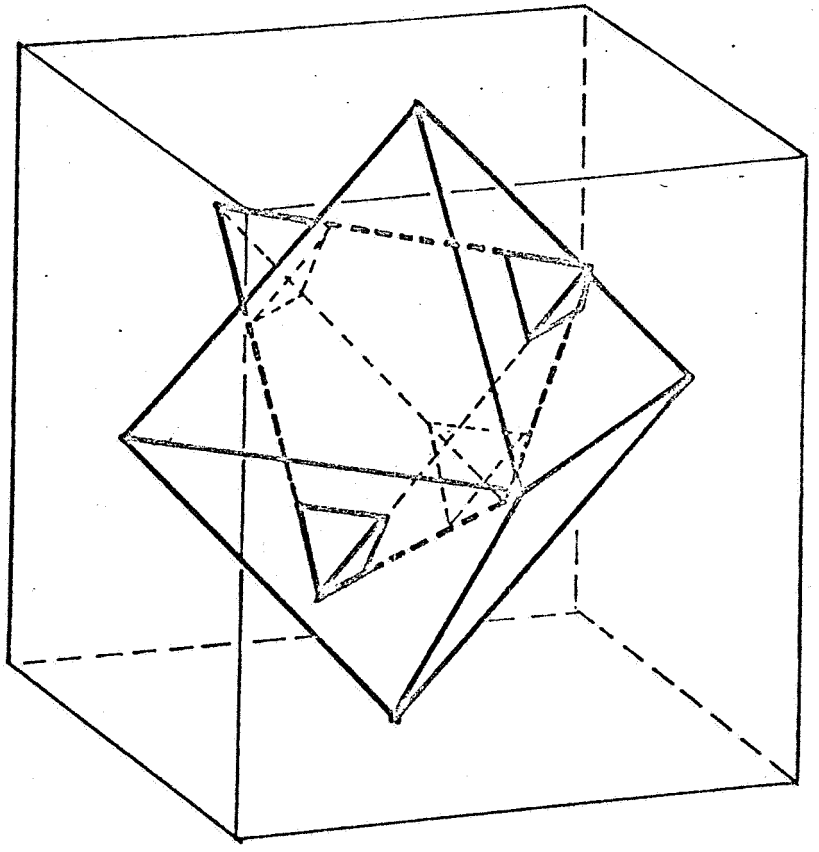

Figure 39.--Schematic drawing illustrating the relationship between the surfaces of a tetrahedron and an octahedron. The latter can be obtained by truncating the apices of the former.

define the point where the concept of surface energy becomes meaningful. Thus, at smaller than this critical size, some means other than the classical surface energy must be used to determine stability of the defect configuration. It is quite possible that the use of vacancy formation energy is appropriate in this region. These small tetrahedral clusters are undoubtedly the nuclei for the larger voids, and it is relatively safe to say that these clusters will co-exist with both voids and dislocation loops, as there will naturally be a size distribution regardless of the vacancy concentration. It is postulated that the small clusters (tetrahedral) are the nuclei for loops as well as voids; the factors determining the final defect configuration are the number of vacancies available for growth and the rate at which these vacancies can be supplied to the growing defects.

Dislocation Loops

Large resolvable dislocation loops have occasionally been observed in quenched and annealed platinum, but the majority appear in the form of black spot defects. The maximum concentration of the latter is at the limit of making a reasonable estimate, ~ $10^{13}/cm^3$, and occurs after 2 hours at 500°C. Even this figure may be somewhat uncertain, because the very nature of the black spot

defects makes identification somewhat ambiguous. Clearly, as seen in the last section, some small voids appear as such, while others may be Frank loops, tetrahedra, or both. The most convincing TEM evidence that at least some of these defects are prismatic loops is the fact that they have been observed to oscillate while under observation, probably due to local electron beam heating. Figure 40 is a sequence of micrographs showing a particular black spot defect in three different positions. This loop was observed to oscillate and then occassionally moved several hundred Angstroms along its glide cylinder.

Determining the foil normal to be [112], the slip trace at B (Figure 41) is (111). The possible Burgers vectors for this system are $\pm$ a/2 $[\bar{1}10]$, $\pm$ a/2 $[0\bar{1}1]$, or $\pm$ a/2 $[\bar{1}01]$. The dislocations at C must lie on $(\bar{1}11)$, since the imaginary trace made by these dislocation would be approximately $[\bar{1}\bar{3}2]$. (See Figure 42.) Thus the possible Burgers vectors are $\pm$ a/2 [110], $\pm$ a/2 [101], and $\pm$ a/2 $[0\bar{1}1]$.

The projected direction of oscillation, X, of the defect at A in Figure 41 is contained in the zone given by the solid line in Figure 42. Now, since only dislocations lying in (111) or $(\bar{1}11)$ could have this Burgers vector, it follows that the defect must be a small prismatic loop moving on its glide cylinder. That is,

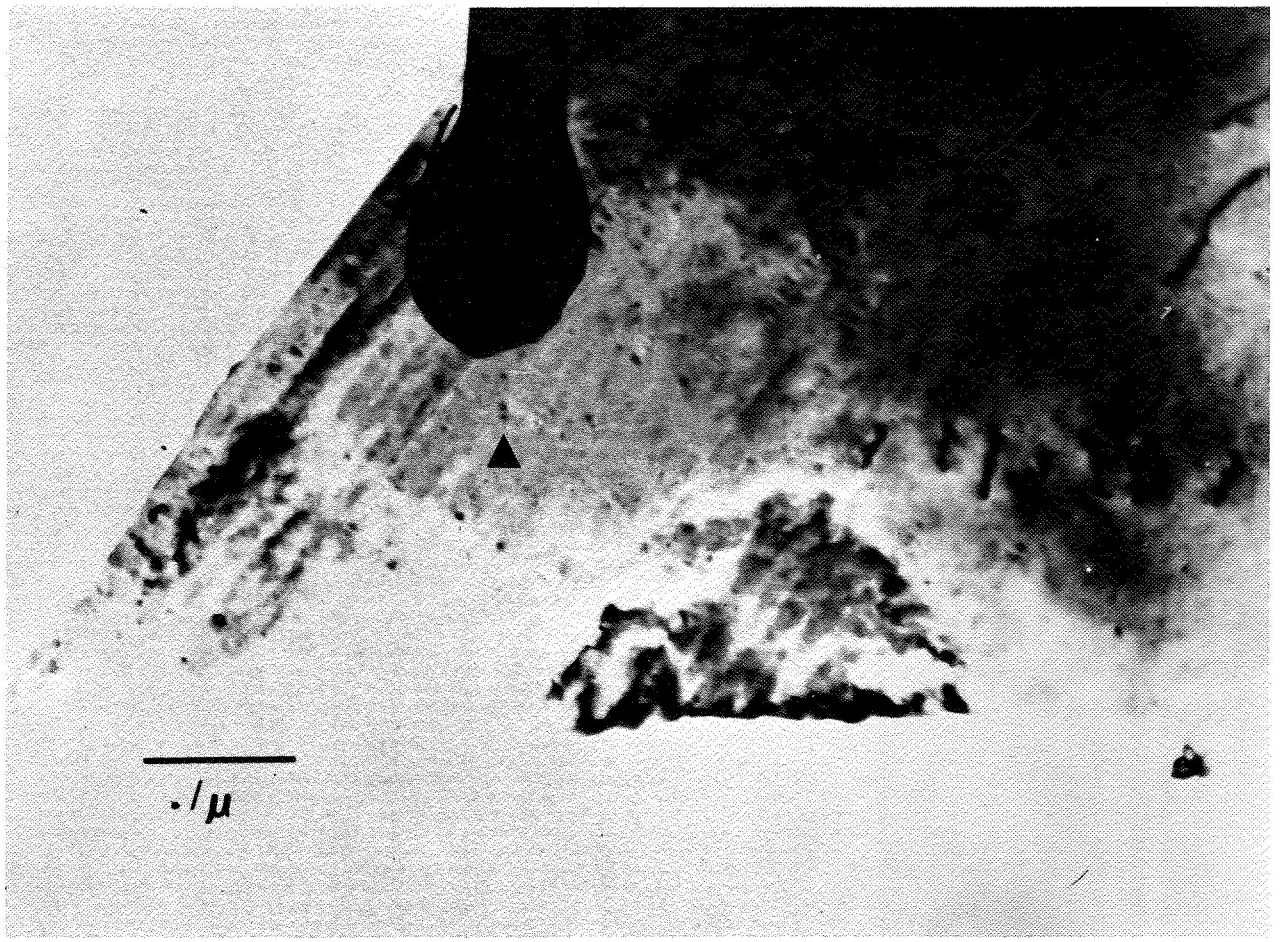

Figure 40.--A sequence of three electron micrographs showing a prismatic loop moving on its glide cylinder. (a) Two defects can be seen below the beam stop.

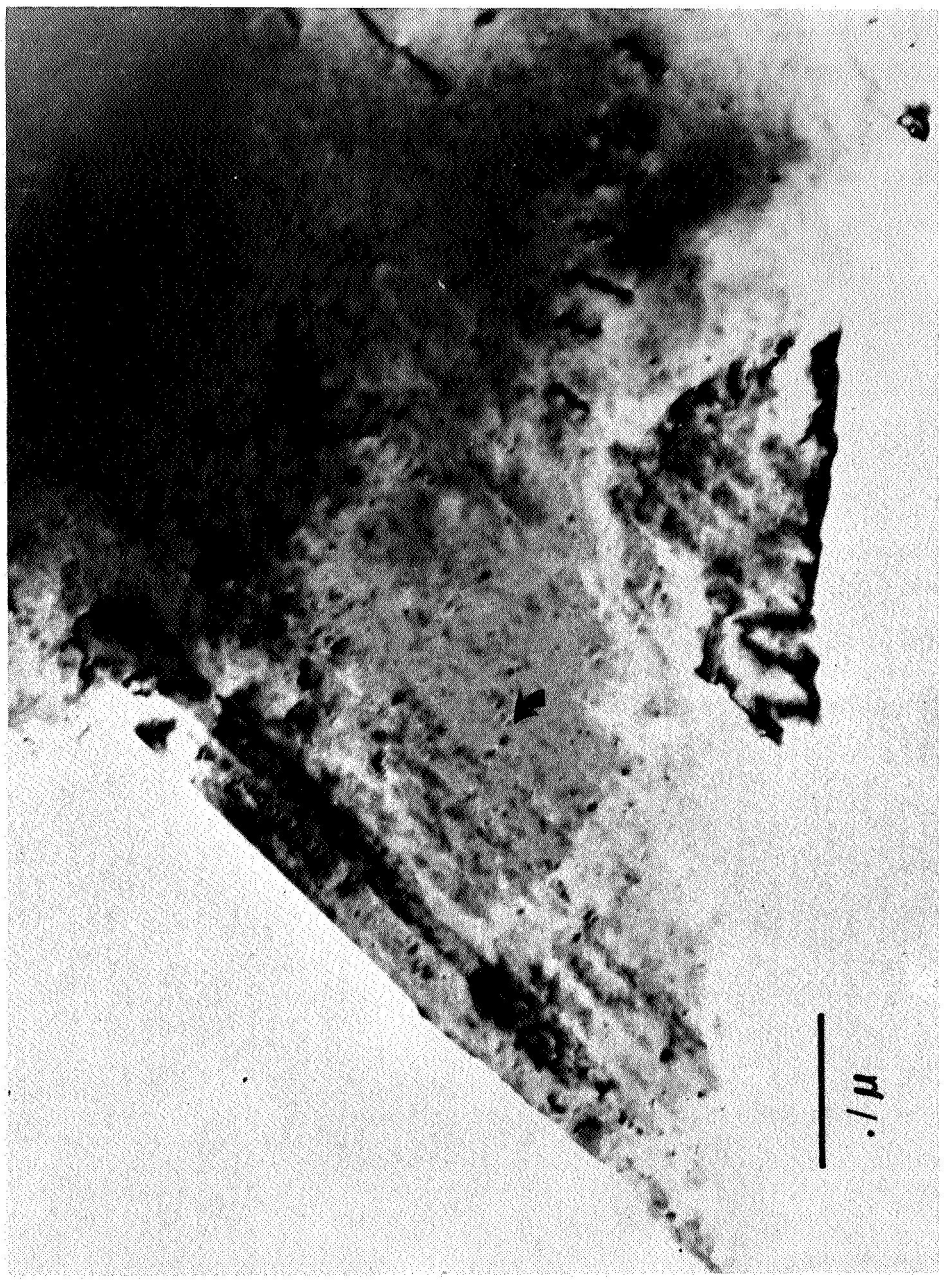

Figure 40.--(b) Same area. The lower of the two defects has moved some 100 Å to the right.

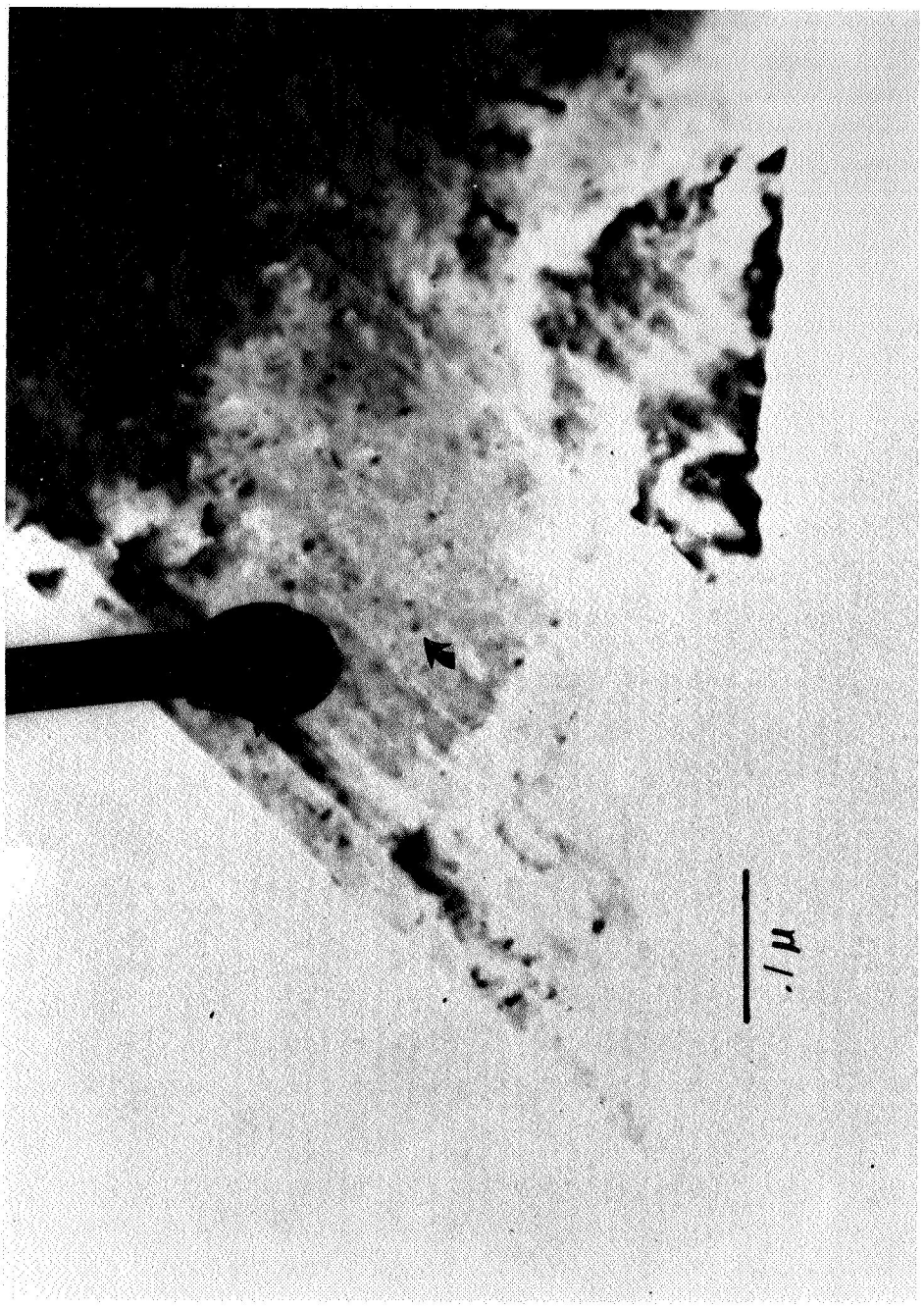

Figure 40.--(c) Same area. After some seconds the loops has moved to the left more than 200 Å.

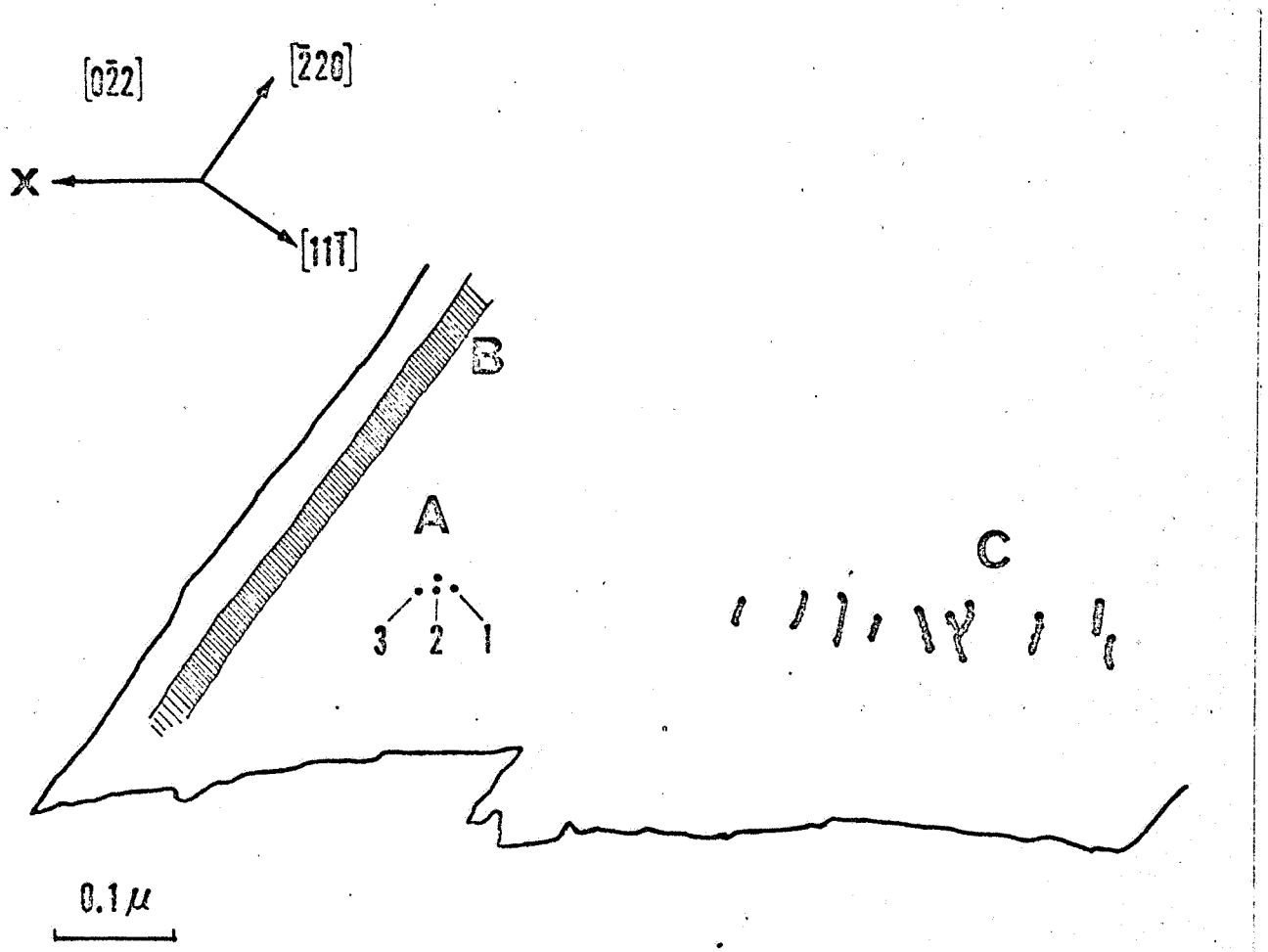

Figure 41.--Schematic drawing combining the information from the three electron micrographs of Figure 40. The oscillating defect is at A, the slip trace at B, and the dislocation array at C.

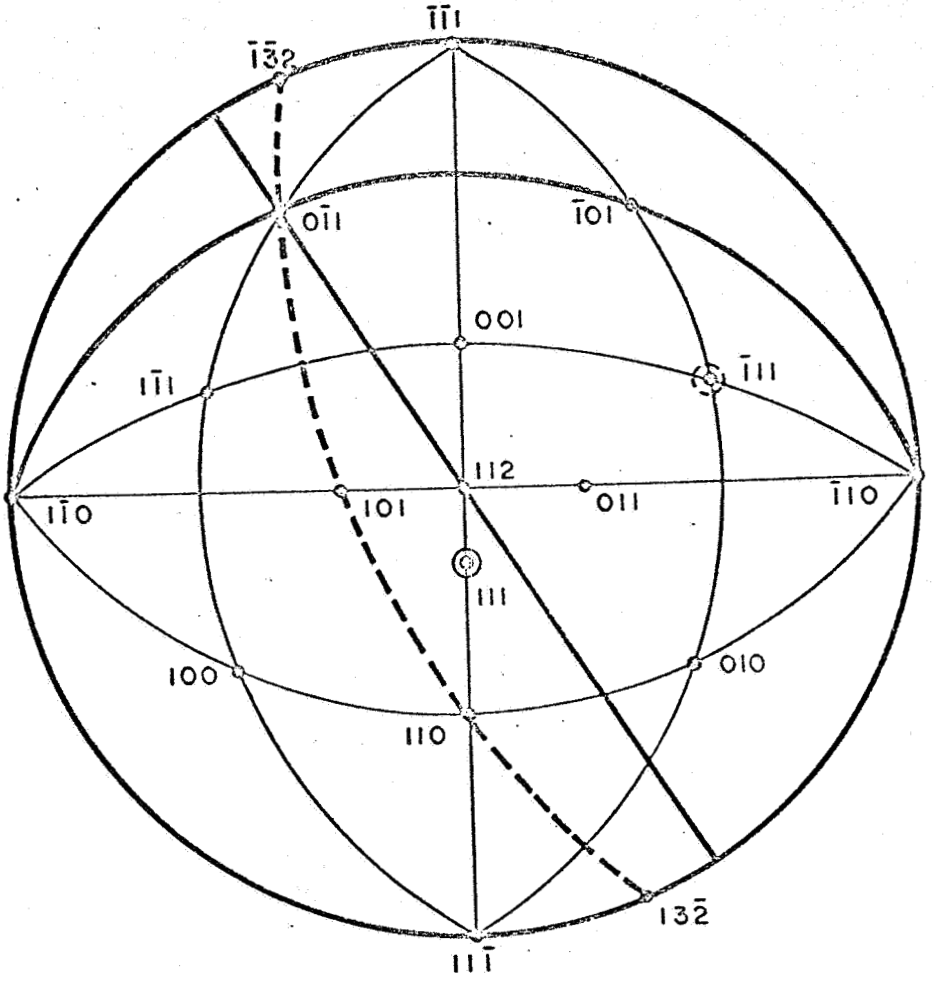

Figure 42.--Stereogram used for the analysis of the oscillating defect.

it has clearly been shown that dislocations lying in either of these two planes have length, thereby eliminating the possibility of the defect being an "end-on" dislocation.

Figure 43 is a micrograph of a resolvable prismatic loop which oscillated in a direction normal to the line of no contrast. This is in agreement with theoretical predictions for the line of no contrast being normal to the operating reflection, $\vec{g}$ = [022] in this case, and for the loop to move in its glide cylinder which must be ± [011]. The only pictorial evidence for oscillation is the fuzziness of the loop contrast. The loop was out of contrast for $\vec{g}$ = [11$\bar{1}$], which is also consistent with a Burgers vector of ± a/2 [011].

The FIM evidence is perhaps even more convincing in that the loops can be atomically resolved. Employing the $\vec{g}\cdot\vec{b}$ criterion described earlier, the two defects in Figures 44 and 45 can be identified as prismatic dislocation loops. Indexing the disturbed pole in Figure 44 as (313), the only Burgers vectors which will produce a single spiral are a/2 [1$\bar{1}$0] and a/2 [0$\bar{1}$1]. The local radius of the specimen in the (202) region is approximately 800 Å. Using the equation d = MRθ, we find the loop diameter to be 40 Å. Field evaporation through the defect sets an upper limit of about 50 Å for the dimension

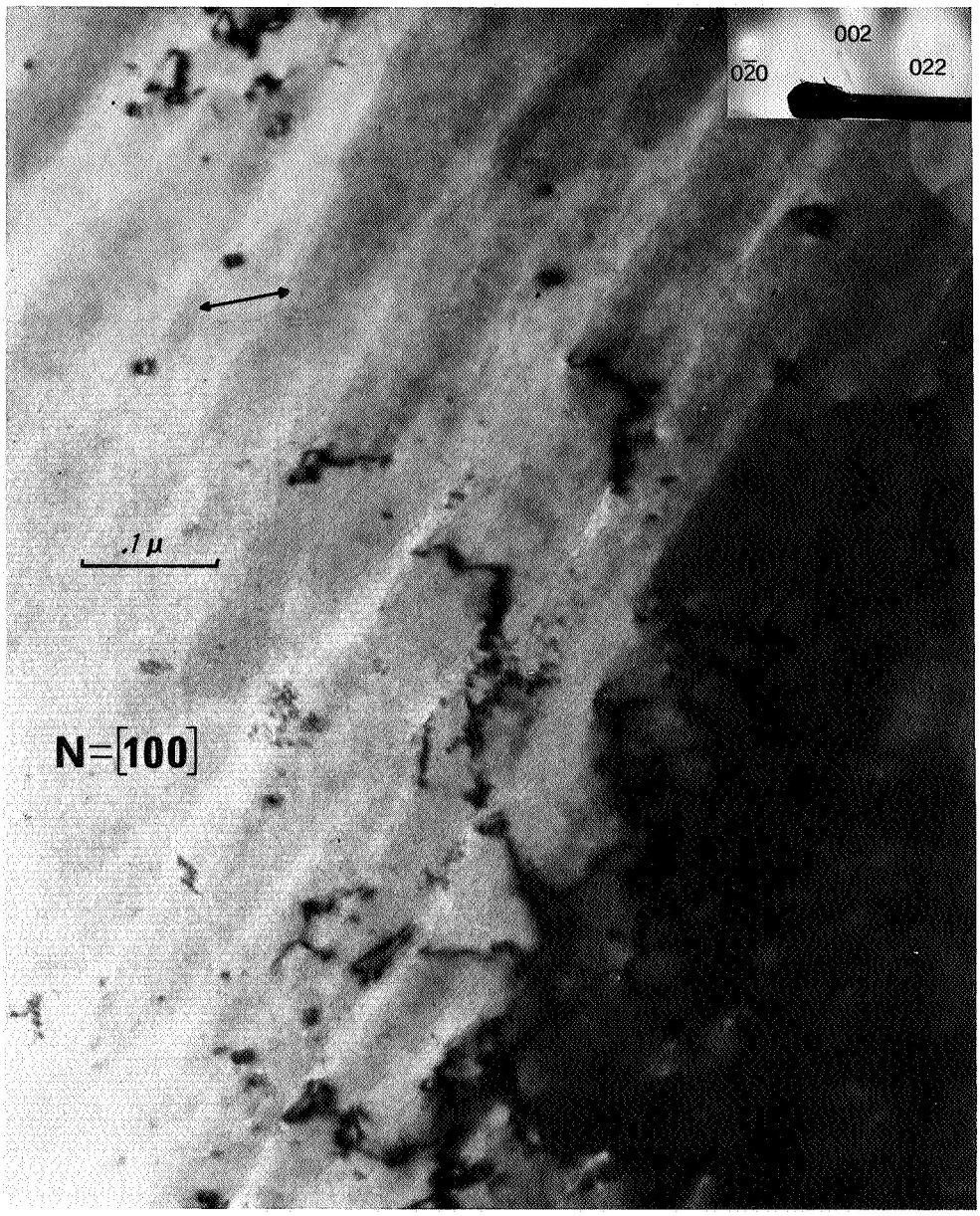

Figure 43.--Electron micrograph of a large prismatic loop. The defect was observed to oscillate normal to the line of no contrast.

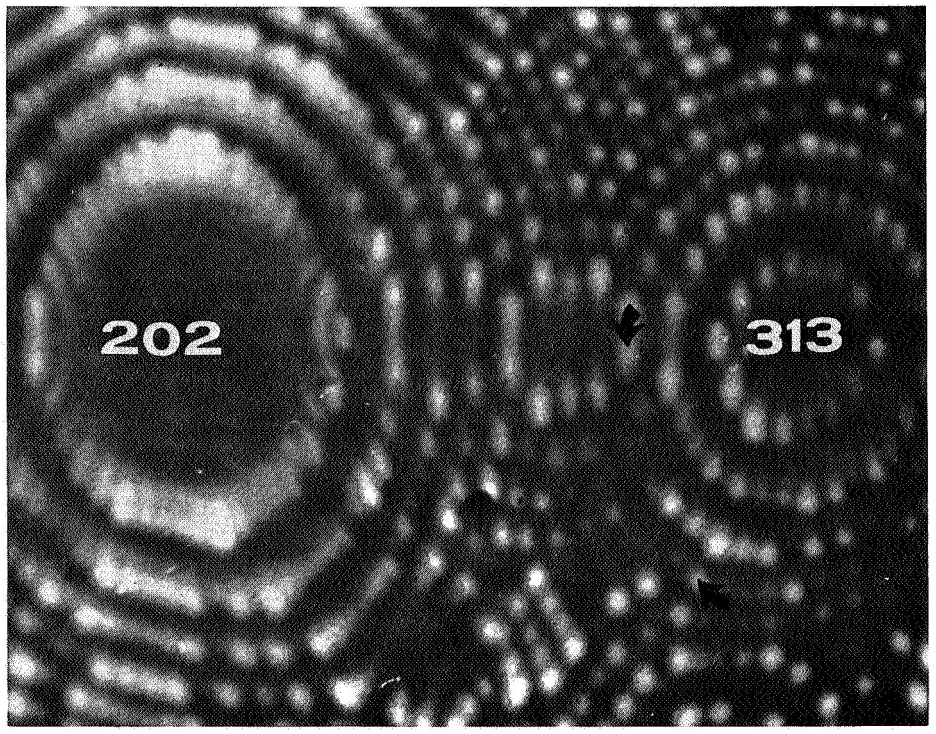

Figure 44.--Field ion micrograph of a prismatic loop intersecting the (313) plane edges.

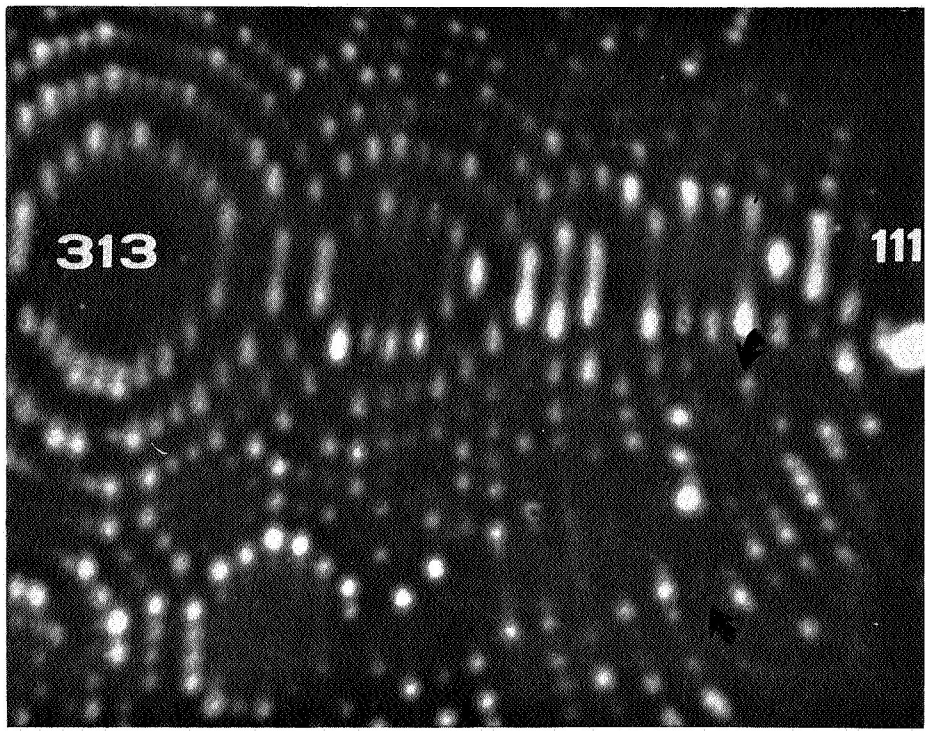

Figure 45.--Field ion micrograph of a prismatic loop intersecting the (111) plane edges.

normal to the tip surface. Because of its small size and the limited field evaporation data, it is not possible to determine the habit plane of the loop.

Figure 45 is another loop in the same tip, but some 50 to 100 Å deeper into the specimen. This loop intersects the surface in the vicinity of the (111) pole and is about 75 Å in diameter. In this case a/2 [110], a/2 [101], and a/2 [011] are all acceptable Burgers vectors for the defect. If we further assume that the loop originally formed on the $(1\bar{1}1)$ plane, a reasonable assumption considering the orientation of the defect, the a/2 [101] type defect can be eliminated since it does not lie in $(1\bar{1}1)$. It is not necessary to require that the loop remain in its habit plane and, in fact, it may well have rotated as far as the (202) plane. The original habit plane could not have been (111), since there are no a/2 <110> type displacements in that plane that can give rise to a single spiral on the (111) plane. This, of course, is a consequence of the geometry of the $\vec{g}\cdot\vec{b}$ criterion.

Other instances of prismatic loops have been observed in the FIM, but none quite so clear and unambiguous as those just described. Unfortunately, as evidenced by TEM, the defect density is extremely low and the stress fields on the FIM tip probably cause many

of these highly mobile defects to slip out of the surface. At any rate, they will most likely migrate to the edge of the image where the stresses are considerably lower.

In Figure 46 a streak is circled that has been attributed to the presence of a Frank dislocation loop. If it is assumed that the streak connects the two intersections with the surface of the bounding partial dislocation (i.e., coincides with the stacking fault), then the loop must lie on the (111) plane and have a Burgers vector a/3 [111]. Figure 47 is an enlargement of this same region, with lines defining the plane edges to aid interpretation. Calculating the average radius in the region of the (31$\underline{1}$3) plane to be 1050 Å and employing the usual d = MRθ relation, the length of the streak is 50 to 60 Å.

The computer was employed to simulate this region of the specimen, and two defects were introduced into the model (Figure 48). The defect in (a) is the Frank loop discussed above. There is good agreement with experiment here, particularly as regards the collapsing of the (002) plane edges around the defect. Also important is the way the spiral configuration merges into the streak, rather than showing a clear beginning and end as did the prismatic loops pictured previously. To remove any ambiguity, a prismatic dislocation loop with Burgers vector a/2 [0$\bar{1}$1]

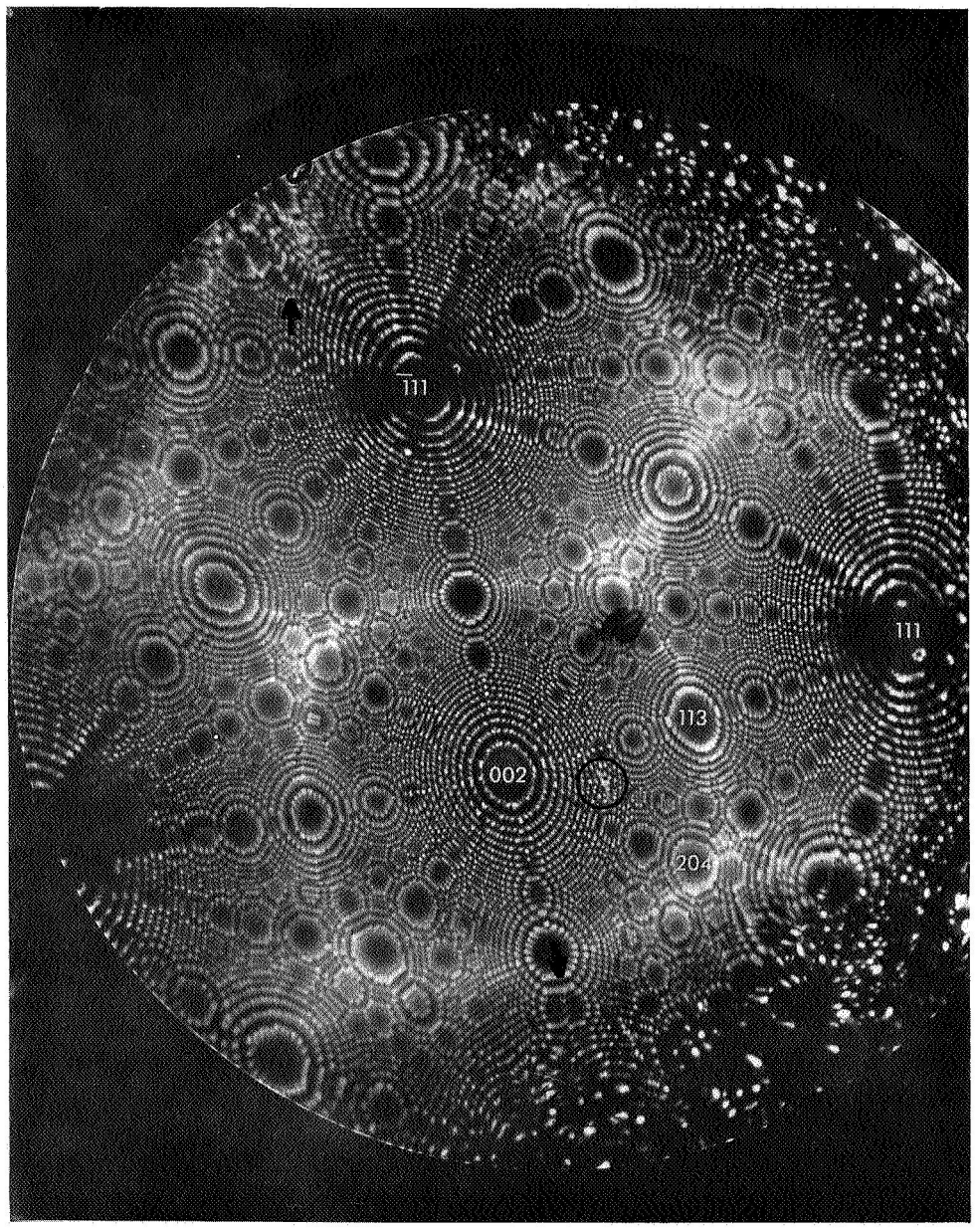

Figure 46.--Field ion micrograph of a Frank sessile dislocation loop. The plane of the fault is (111) and it intersects the surface in the (002) region.

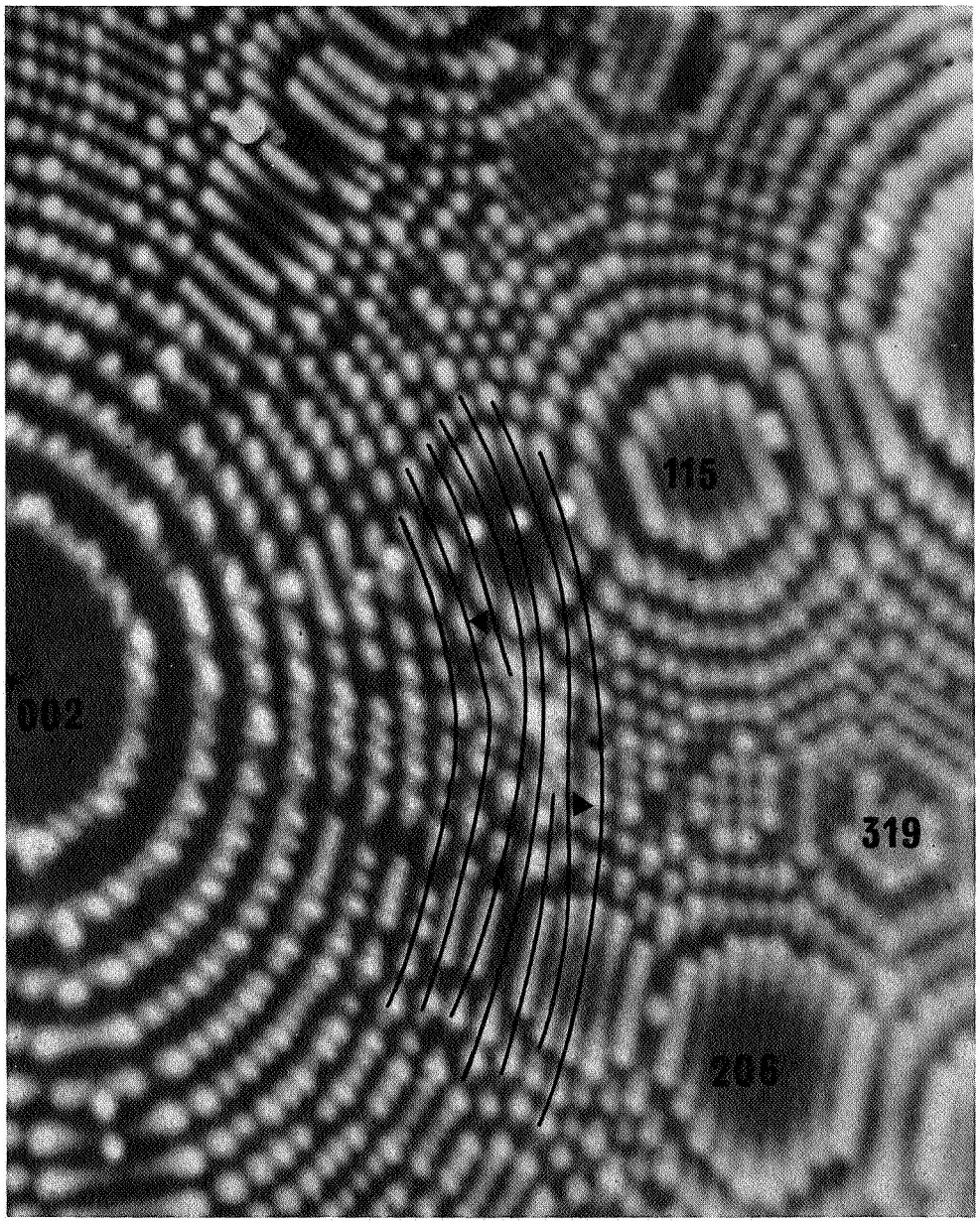

Figure 47.--An enlargement of the (002) region in the previous micrograph. The plane edges have been emphasized to aid interpretation.

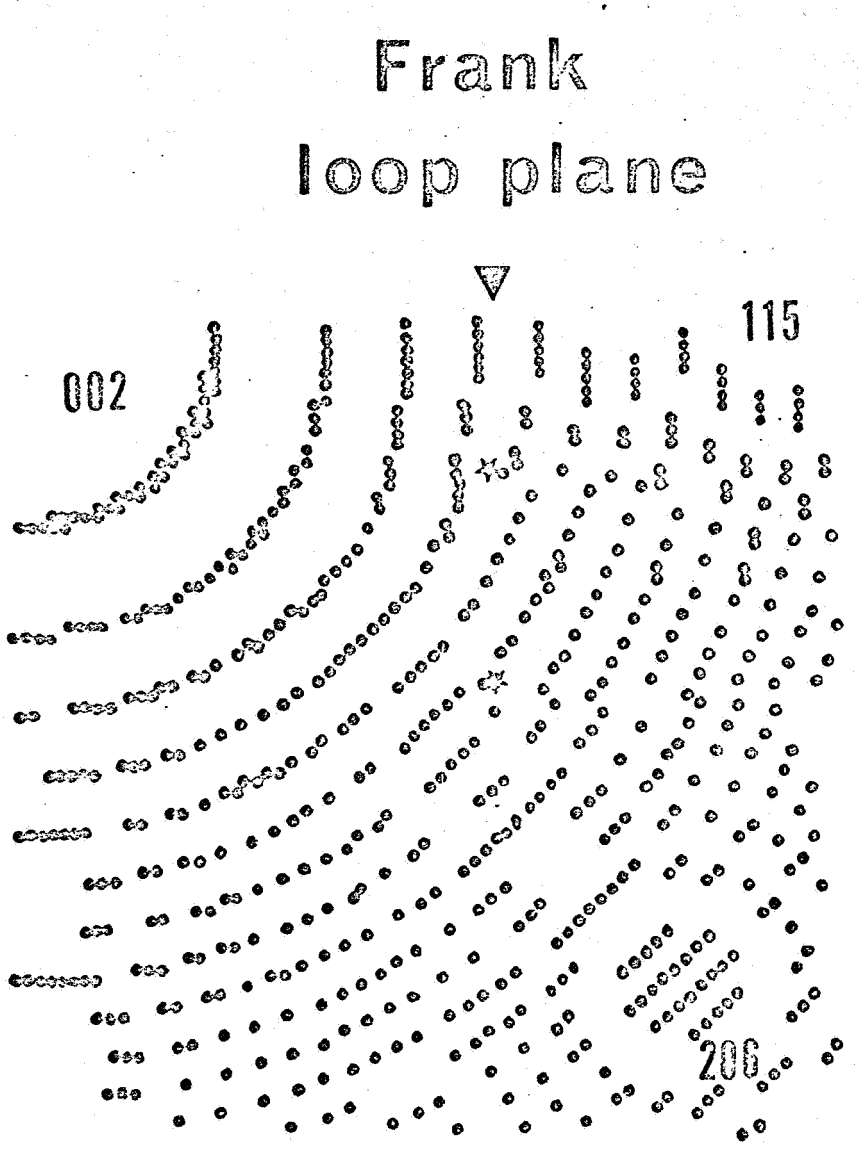

Figure 48.--Computer simulation of the region containing the defect in the previous micrograph. (a) The presence of a Frank loop has been simulated.

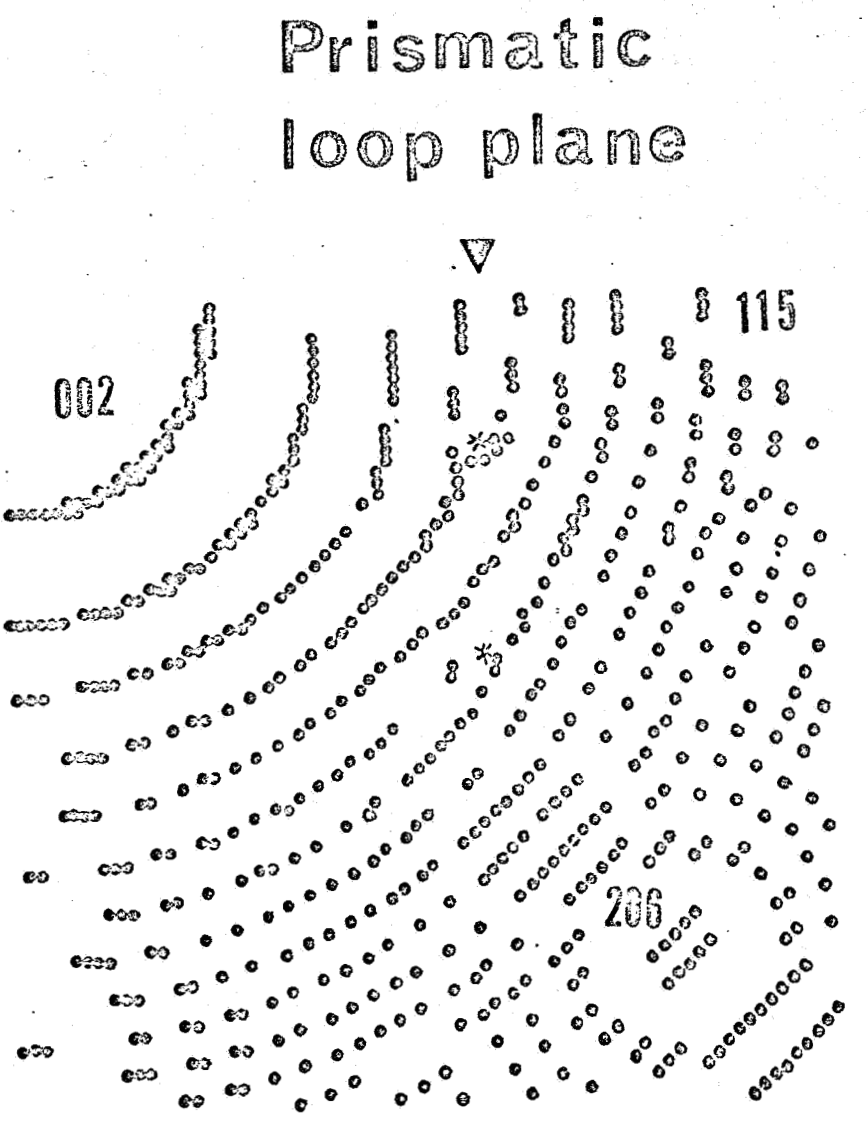

Figure 48.--(b) Same region, only the presence of a prismatic loop has been simulated.

was introduced into the same region. The dislocation a/2 $[\bar{1}01]$ also lies in (111) and would give the same result, whereas a/2 $[1\bar{1}0]$ is in the (002) plane and would therefore be invisible. Figure 48b is the result. The important difference between the two simulated images is the absence of any collapse of the (002) rings near the a/2 $[0\bar{1}1]$ defect. The evidence is much in favor of interpreting the loop as being sessile in nature. That is, the defect is in a high-stress region of the tip, and if it were glissile it would not be stable there. Furthermore, all previous work both experimental and computer, indicates that streaks are associated with stacking faults. Stacking faults will be discussed later in this chapter.

Figure 49 illustrates the behavior that one would expect if all quenched-in vacancies were annihilated at dislocations, as has been suggested by Jackson (1965a). However, this type of structure has been noted in only two regions in two different foils, both of which were annealed for 24 hours at 500°C. The efficiency of dislocations as vacancy sinks is treated extensively by Kuhlmann-Wilsdorf *et al.* (1960). Briefly, the authors assume dislocations to be classified into two groups, old and new. New dislocations are those which formed or moved at fairly low temperatures and not subjected to any elevated temperature treatment. Conversely, old

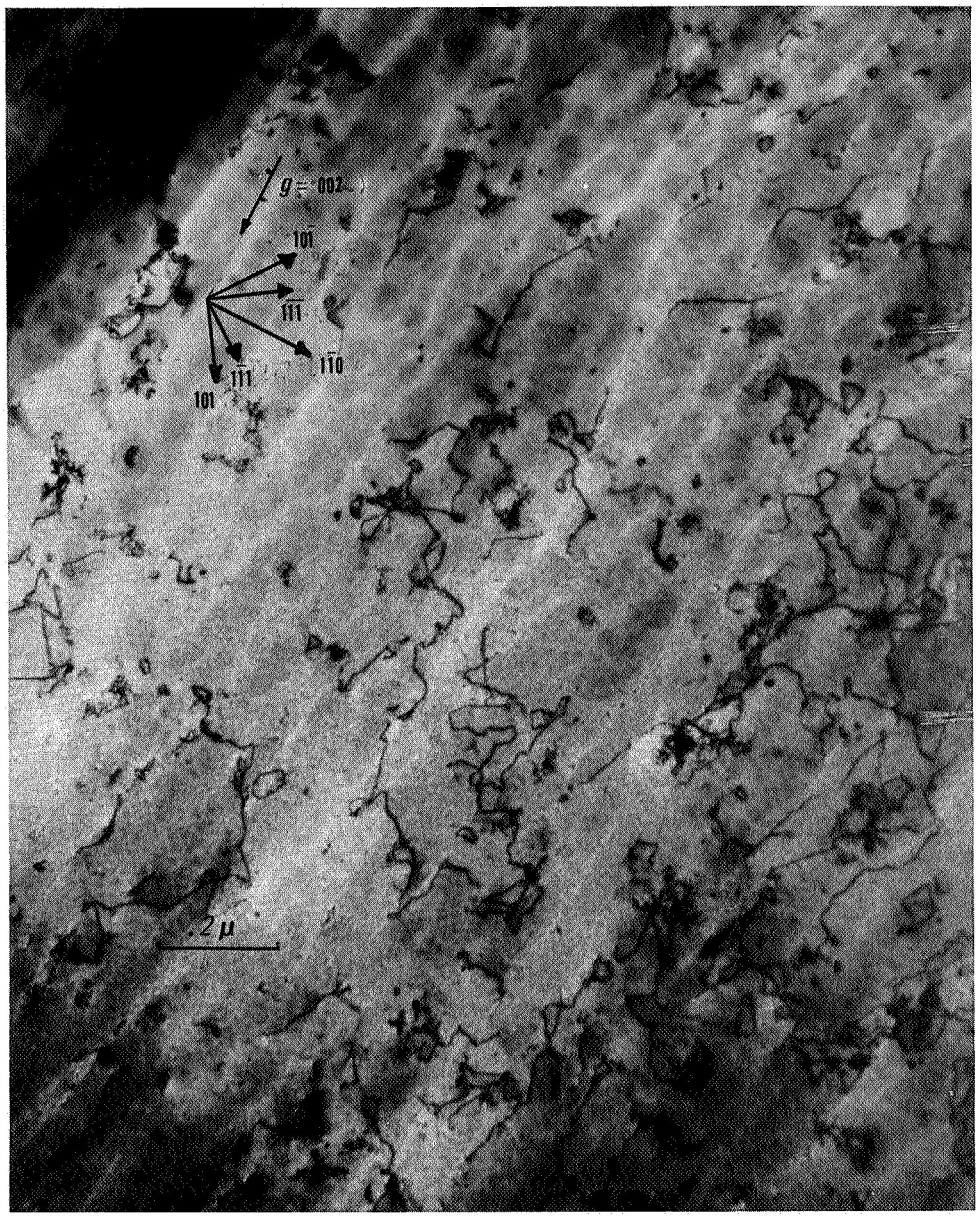

Figure 49.--Electron micrograph of a foil containing large prismatic loops and heavily jogged dislocation lines. Note the preponderance of line segments lying along projected <110> and <112> directions.

dislocations are described as those which have undergone annealing while stationary. Experimental evidence indicates that new dislocations climb by the Bardeen-Herring mechanism, i.e., simply absorbing point defects, whereas old dislocations absorb vacancies by nucleating superjogs. The electron micrograph shown here is a classical example of superjogs. Note that there is a preponderance of dislocation segments along projected <110> and <112> directions, indicating that a large number of the jogs and pinched-off dislocation loops lie on {111} and {110} type planes.

Figures 50 and 51 are dark field micrographs of the same area with the operating reflection reversed while $\vec{s}$ is held constant. In other words, the foil is tilted approximately 1° to bring the same region into good contrast with the new operating reflection. The procedure is carried out entirely under dark field conditions. The micrographs illustrate two important points. First, the small spot defects exhibit a clear black-white contrast which is characteristic of the strain fields around small vacancy or interstitial defects such as dislocation loops. The direction of the white end of the contrast is known to be a function of the depth into the foil as well as the character of the defect. From the history of these foils one would hardly expect to find interstitial defects,

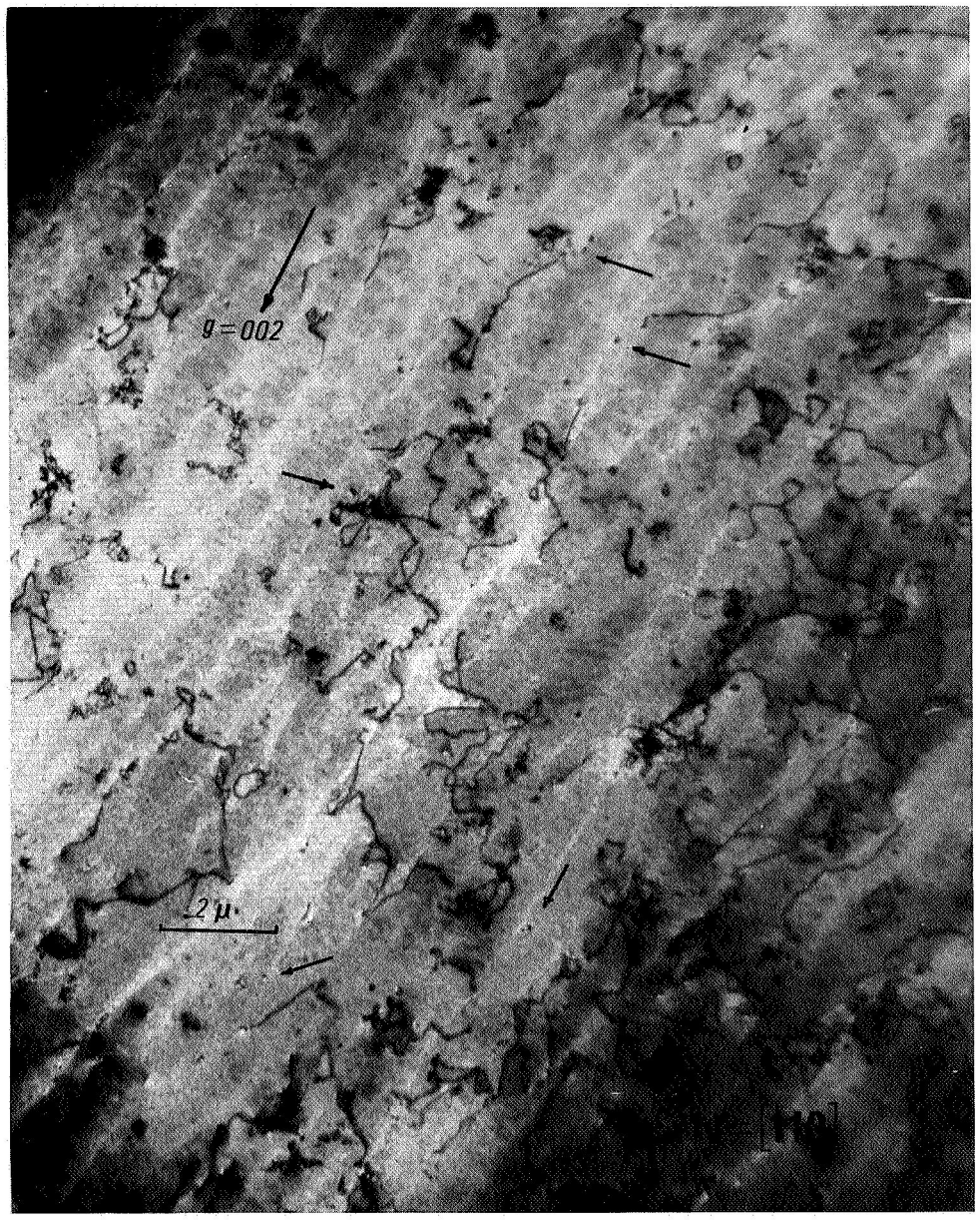

Figure 50.--Dark field electron micrograph of the same region with $\vec{g}$ = (002). Defects exhibiting black-white contrast are arrowed.

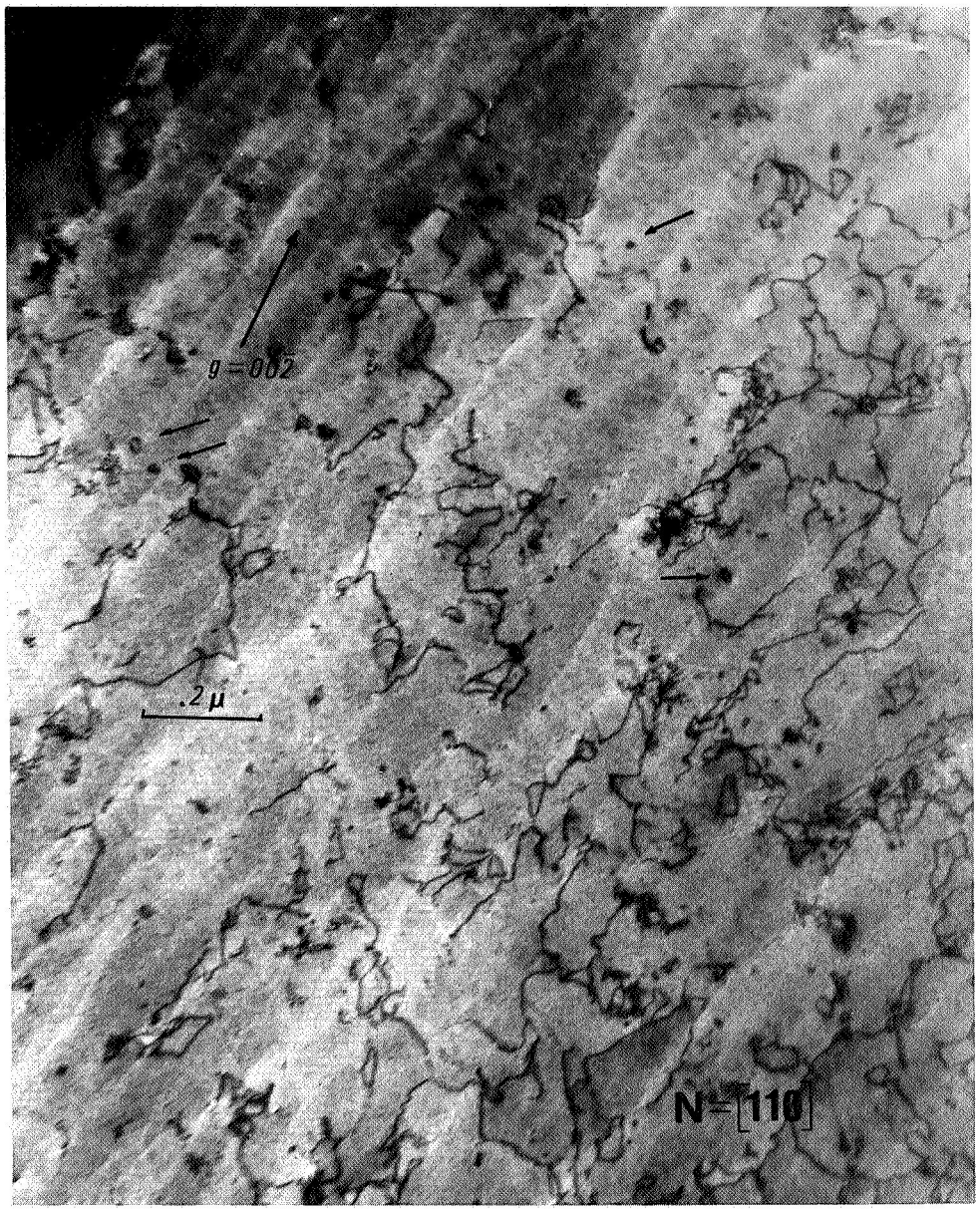

Figure 51.--Dark field electron micrograph of the same region with $\vec{g} = (00\bar{2})$. Loops exhibiting a size change are arrowed.

so the black spots are undoubtedly vacancy loops. This can be verified experimentally but requires precise depth measurements using a stereo technique.

Also of significance is the fact that there are numerous examples of loops changing size upon reversing $\vec{g}$. As mentioned in the chapter on electron microscopy, this is positive evidence for a/2 <110> prismatic loops.

Stacking Faults

At present there is no definite TEM evidence for the existence of Frank loops (i.e., imperfect prismatic loops). However, FIM work indicates that these faulted defects do exist. Computer simulation studies (Sanwald 1967) reveal that stacking faults with their associated partial dislocations are the only planar defect capable of producing a streak in a field ion image. Referring again to Figure 46, it can be seen that there are several instances of streaking. In at least one of these cases the streaks can be deduced as lying on a {111} plane. Many such cases have been observed in images of quenched and annealed platinum, and these streaks always occur at the edges of the specimen. It is possible that the stresses set up in the field ion microscope are sufficient to cause dislocations to split into partials. As pointed out by Ruedl *et al.* (1962) the occurrence of Lomer-Cottrell

barriers (Figure 52) implies a dissociation into partial dislocations.

The point of this discussion is the following: The generally accepted value of the stacking fault energy for platinum is 95 ergs/cm^2. The value for aluminum is approximately 200 ergs/cm^2 and that for nickel has been reported to be anywhere from 150 to 450 ergs/cm^2. Loretto *et al.* (1966) have shown that faulted loops occur in quenched aluminum, and more recently Humble *et al.* (1967) have observed faulted dislocation loops and stacking fault tetrahedra in zone refined nickel. It would therefore seem quite reasonable that, under the proper conditions, these more complex defects involving stacking faults should be present in quenched platinum. While transmission microscopy has not produced any such evidence, this author maintains that faulted defects have been observed in quenched platinum by means of field ion microscopy. It is only a matter of time before the conditions will be met to make them visible in the electron microscope. Suggestions will be presented in the following chapter.

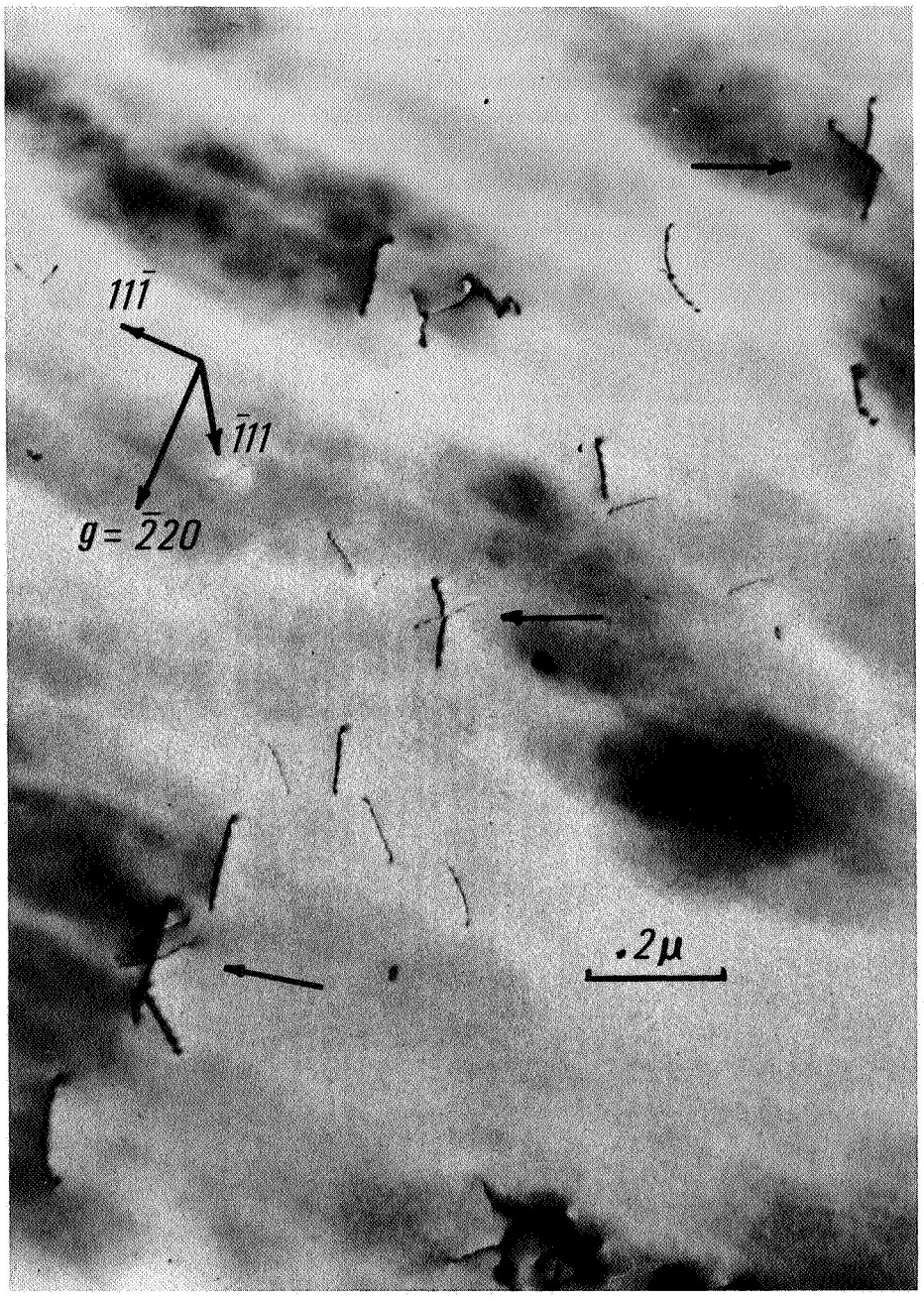

Figure 52.--Electron micrograph of dislocation intersections resulting in the formation of Lomer-Cottrell barriers.

CHAPTER VI

CONCLUSIONS AND SUGGESTIONS FOR FURTHER STUDY

The picture is by no means complete, but several points have been clarified. Direct evidence has been presented for the clustering of vacancies in quenched and annealed platinum. It has been shown via TEM and FIM that at least some of these clusters collapse to form prismatic dislocation loops, while others grow into polyhedral voids. The latter defect is felt to be the cause of the irreversible change in resistivity measured by Cízek (1967). It is entirely possible that many of the black spot defects are Frank sessile dislocation loops and there may even be some stacking fault tetrahedra, although no evidence for the latter has been found.

The author does feel, however, that the field ion micrograph in Figure 46 along with additional features observed in both TEM and FIM is convincing evidence for the presence of faulted loops and Shockley partial dislocations. The field ion microscope could well be a useful tool for determining stacking fault energies for materials having a relatively high value of this parameter. Of course this will require that more be understood about the imaging stresses than is presently known. Perhaps the

experiment could be performed in reverse to study the field stresses in the specimen.

The maximum size of a particular defect is felt to have a fundamental meaning in terms of the energy of the matrix material and the component dislocations or surfaces comprising the defect. Certainly the shape change between 25 Å voids and 150 Å voids is significant. As mentioned in the text, one would like to obtain accurate values of the surface energy from these types of data. It is suggested that a strain analysis (Ashby and Brown 1963a,b) be carried out to obtain an accurate measure of the lattice strain around the void.

The sequence in which the void surfaces facet has been found to be consistent with the values of McLean and Mykura (1966) for the surface energy anistropy of platinum. That is, the {111} plane is the most stable, with {100} and {110} following in that order. Although the "spherical" voids in platinum have been interpreted by this author to be truncated only by {100} planes, the analysis is not unambiguous. In other words, {110} facets may also be present, but the strain in the lattice and the small defect size does not permit identification.

One method to further investigate this question is to employ field ion microscopy on large voids. A study of this type is now in its early stages but has yet to provide

any useful results. The difficulty at present is that the larger voids appear as a depression in the surface, with a considerable amount of lattice collapse and/or distortion of the image (Figure 38). This behavior is more than likely due to preferential field evaporation of the atoms around the perimeter of the intersection of the void with the surface, rather than being due to local lattice strain. If this is the case, then techniques such as hydrogen promotion (Müller *et al.* 1965) may be useful. Recent developments in the theory (Müller 1967) of hydrogen promotion and the findings of Swanson *et al.* (1967) that xenon in the imaging gas also reduces the field necessary for imaging are encouraging. Techniques such as this may be the key to determining the precise atomic geometry of the polyhedral void in quenched platinum.

Figure 53 is a qualitative plot of the densities of the two types of defects observed in this investigation. Sampling can be a problem in field ion microscopy, since the surface area viewed is on the order of 10^{-10} cm^2. If one field evaporates through 1000 Å, the total volume sampled is only 10^{-15} cm^3. It is therefore obvious that the defect density should be at least $10^{15}/cm^3$.

A program is now being set up whereby the defects will be introduced via electron, proton, and/or α-particle irradiation. It is felt that this treatment will increase

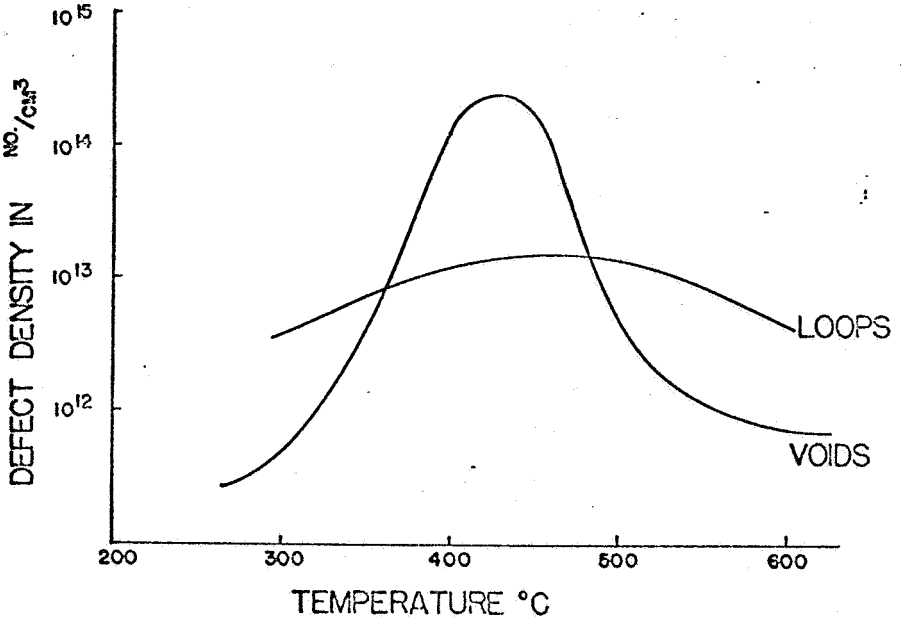

Figure 53.--Qualitative plot of the observed defect density versus annealing temperature. The maximum concentration of voids occurs at 400°C while the maximum density of black spot defects occurs at a slightly higher temperature.

the defect density and, according to Ruedl and Amelinckx (1963), both intrinsic and extrinsic dislocation loops are formed after quenching, irradiating with α-particles, and annealing platinum foils. A study is being proposed which would combine transmission electron microscopy, field ion microscopy and computer simulation in order to test this thesis. There is little doubt that intrinsic defects can easily be differentiated from extrinsic defects in simulated images, but it remains to be seen if the differences can be detected experimentally. If it is possible, FIM will certainly be a useful tool to this end, particularly since TEM requires exacting conditions to distinguish between the two. Indeed, there is still a great deal of controversy as to the nature of these defects in neutron irradiated copper. See, for example, McIntyre (1967) and Rühle and Wilkens (1967).

It is further suggested that any studies involving a correlation between field ion microscopy and electron microscopy be carried out on the same starting material. Although wire may be rolled to obtain foil specimens, it is perhaps wiser to prepare field ion tips from the foil. Rao and Thomas (1967) have only recently reported a successful technique for preparing specimens from molybdenum foil.

In summary, the author feels that this preliminary study of quenched and annealed platinum clearly demonstrates that FIM in conjunction with TEM can provide the researcher with a powerful tool for studying the defect structure of metals. This is particularly true for imperfections which are at or beyond the resolution capabilities of the electron microscope; but the technique is not necessarily limited to these. Furthermore, it appears that the field ion microscope can provide independent measurements of such parameters as stacking fault energy and surface free energy, if one is imaginative in the design of the experiment. The possibilities are many.

APPENDICES

APPENDIX I

INDEXING FIELD ION MICROGRAPHS

Derivation

Assuming a constant local radius, r, between any two poles separated by a curvilinear distance, S_t, along the surface of a tip:

$$S_t = r\theta \qquad \text{(I-1)}$$

and the corresponding length along the surface of a projection sphere of radius R is (Figure 54):

$$S_s = R\theta \qquad \text{(I-2)}$$

If a projection point is now chosen such that the projected length X_p is equal to the arc length, S_s, we have for any zone line passing through the center of the image:

$$X_p = R\theta \qquad \text{(I-3)}$$

This is not any standard type of projection since the projection point must vary with the angle θ in order to satisfy equation I-3.

In general, the length R is not equal to the specimen-screen distance, but the relationship of equation I-3 can be maintained by orthographically projecting the information on the projection plane to the screen. Thus,

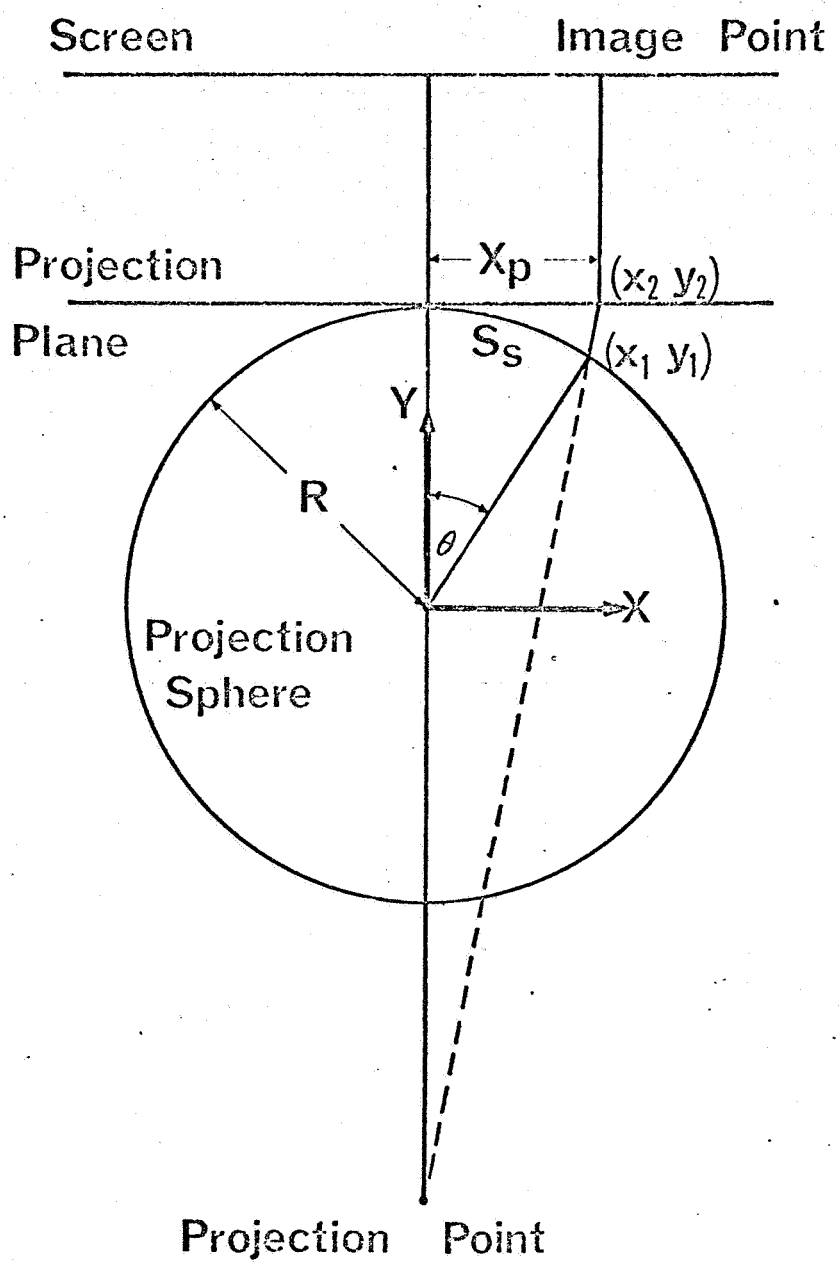

Figure 54.--Projection of a random direction onto a planar surface with the projection point chosen so that $X_p = S_s$.

the linear distance d on the micrograph is related to the length X_p on the projection plane (or the screen) by the expression:

$$d = M_L M_p X_p = M X_p \qquad \text{(I-4)}$$

where M_L is the magnification of the camera optics and M_p is the magnification introduced during the printing of the photographs. Therefore, equation I-3 becomes simply:

$$d = MR\theta \qquad \text{(I-5)}$$

While the choice of these three projections (gnomonic, pseudo-stereographic, and orthographic) appears arbitrary, it is not invalid to assume that the three straight line segments approximate the actual ion trajectories proposed by Drechsler and Müller (1952). The justification for the nature of the intermediate projection is that it has the desirable property of maintaining a one to one correspondence between radial distances before and after projection.

Discussion

It is interesting to calculate precisely what type of projection is required to satisfy equation I-3. Knowing the points (x_1, y_1) and (x_2, y_2) in Figure 54, it is a simple matter to determine the coordinates of the projection point. Thus:

$$\frac{y}{R} = \frac{\theta \cos \theta - \sin \theta}{\theta - \sin \theta} \qquad \text{(I-6)}$$

In the limit as $\theta \to 0$, $y \to -2R$. Choosing $\theta = 60°$ as an upper limit, we find $y = -1.890R$. Thus the projection point is approximately two radii behind the tip--the same as that proposed by Brandon.

This result suggests that it may be meaningful to compare equation I-5 with Brandon's (1964) equation for a projection from the center of the second sphere:

$$d = R\frac{3 \sin \theta}{2 + \cos \theta} \qquad \text{(I-7)}$$

where $R = MR$ of equation I-5 and θ has the same meaning as in equation I-5. Taking the first two terms of the series expansion of sin θ and cos θ, equation I-7 reduces to equation I-5 exactly. In fact, the difference between the calculated d-values is less than 1% over the angular range of a field ion image.

Brandon has already shown that the pseudo-stereographic projection is inherently more accurate than either the orthographic or stereographic projections. He also mentions that for any given projection, local variations in tip radius (Müller 1958b) will result in a variation of the radius of the projection sphere. This is probably the major source of error in determining the angle to any one

pole but appears to be minimal when averaged over the entire micrograph.

It can also be shown using spherical trigonometry and projective geometry that the present method may be employed to compute angles between poles, both of which are considerably displaced from the image center. In fact, the linear distance (e.g., measured on a micrograph) between two points both of which are 45° from the center is only 10% larger than the actual curvilinear distance on the projection sphere for small angular separations. This error drops to zero at 90° separation. Therefore, it can be confidently stated that cross checks on pole indexing can be made from any place on the image within 45° of the center.

Experimental Procedure

Since the projection sphere is not tangent to the microscope screen due to the focusing of the ion beam (Drechsler and Müller 1952; Müller 1960), R must be chosen by a trial and error method analogous to that used for indexing an x-ray Laue pattern. That is, one must make use of symmetry and knowledge of specimen history to make an assumption as to the indices of the central pole, to be used as a reference, and at least one other pole. Strictly speaking, the reference pole should be located

at the geometric center of the image where, for a symmetrical tip, the projection sphere is tangent to the projection plane. However, it is sufficient to use the pole nearest the center of the photograph. Using the appropriate value of θ in equation I-5, a corresponding value of the product MR is obtained. (It is usually unnecessary to separate these two parameters.) Then using this MR, equation I-5 is solved for θ using a d-value for a third unknown pole. This θ is then compared with tabular values of angles between various planes and the reference pole. It may be necessary to make several choices for the second pole in order to obtain a value of MR that will give self-consistent values of θ for the third, fourth, etc., poles. Once an appropriate value of MR is obtained, equation I-5 is solved repeatedly until the entire micrograph is indexed. When indexing any micrograph using this method, one must keep in mind that, due to the geometry of the surface, only those planes which satisfy the conditions analogous to Bragg diffraction will appear (Drechsler and Wolf 1958, Ranganathan 1966b). For example, in an FCC crystal, it is the {002} planes (h, k, l, unmixed) which are visible as concentric rings--not the {001} planes as is sometimes stated.

APPENDIX II

DESIGN CONSIDERATIONS IN CONSTRUCTING THE FIELD ION MICROSCOPE

There are essentially five subsystems in the field ion microscope discussed here: (1) a cryostat, (2) an ultra-high vacuum system, (3) a controlled source of pure imaging gas, (4) an adjustable high voltage source, and (5) a phosphor screen for viewing and recording the image. Figure 55 is a photograph of the entire system.

Cryostat

In cryostat design, one must be aware of the low heat capacity of cryogenic fluids that necessitates extreme care be taken to avoid any large heat leaks to the cryostat. Since radiation becomes a significant means of heat transfer at these temperatures, it is desirable to shield the liquid hydrogen cryostat from the room temperature surroundings. This has been accomplished by means of a liquid nitrogen dewar which almost completely surrounds the cryostat and specimen.

Convection is a small, but real problem since the microscope body must be back-filled with an imaging gas. In order to minimize heat transfer by this mechanism, the

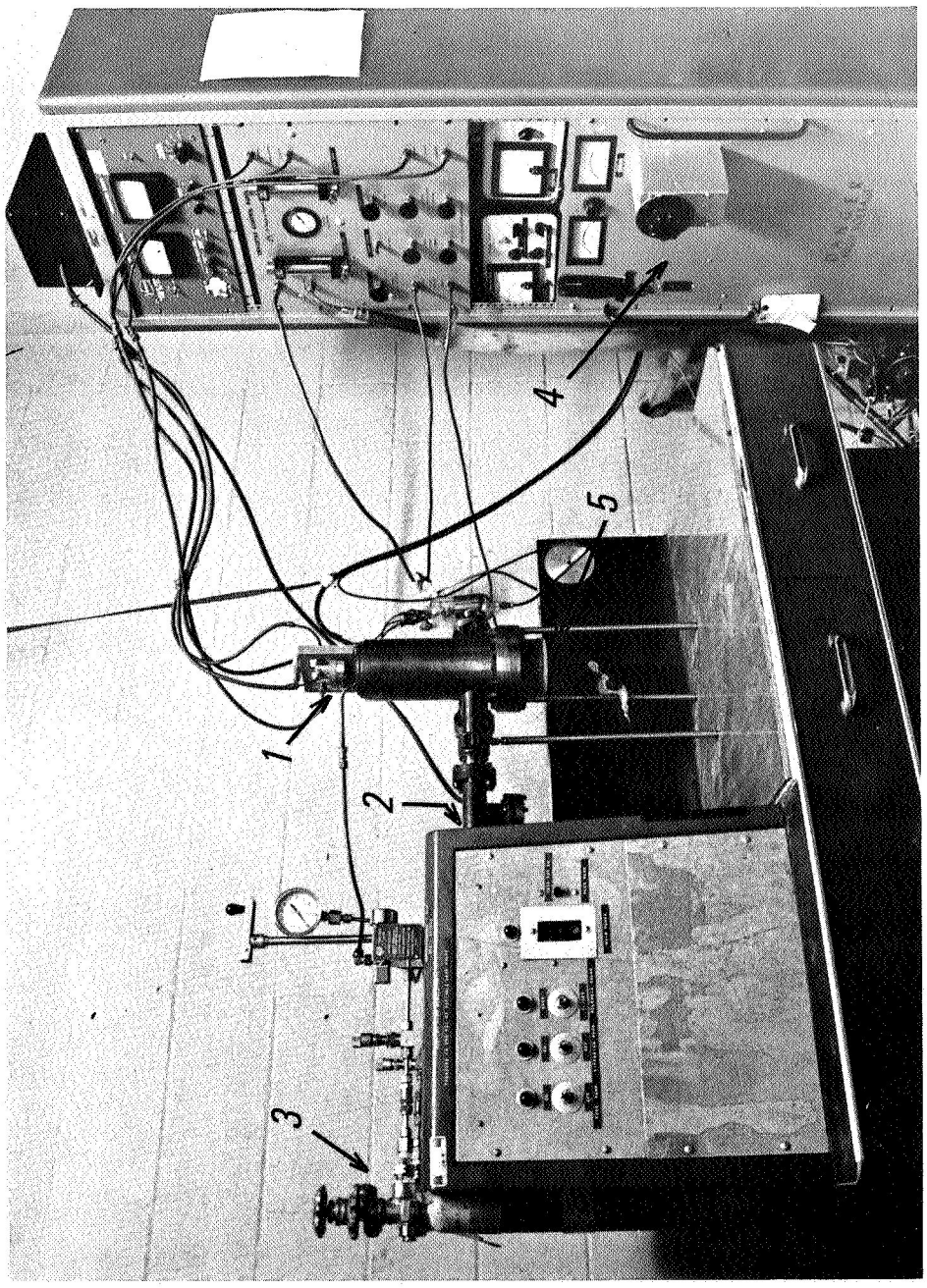

Figure 55.--Photograph of the field ion microscope. The five subsystems are arrowed. 1. cryostat; 2. vacuum system; 3. imaging gas supply; 4. high voltage generator; 5. viewing port.

gas is precooled in the liquid nitrogen dewar before it passes into the specimen chamber.

Conduction is perhaps the most difficult mechanism to deal with. This is particularly true when dealing with a metal FIM body where a high voltage connection must be made to the specimen, must be electrically insulated from the body, and must not be too large a heat leak. This has been accomplished using 0.015" diameter Nichrome wire for making the electrical contact between the high voltage feedthrough and the specimen. This wire is sheathed in a Pyrex capillary, over most of its length, to prevent discharges between it and the FIM body.

A major problem is encountered in making the connection to the specimen itself. It is absolutely imperative that the specimen assembly not be thermally shorted to room temperature, so one must be clever in making this connection. Figure 56 illustrates how this was done. By having the tungsten leads re-entrant through the liquid hydrogen bath, the cryostat is admittedly shorted to room temperature. More important, however, is the fact that the specimen is still thermally connected only to the liquid hydrogen.

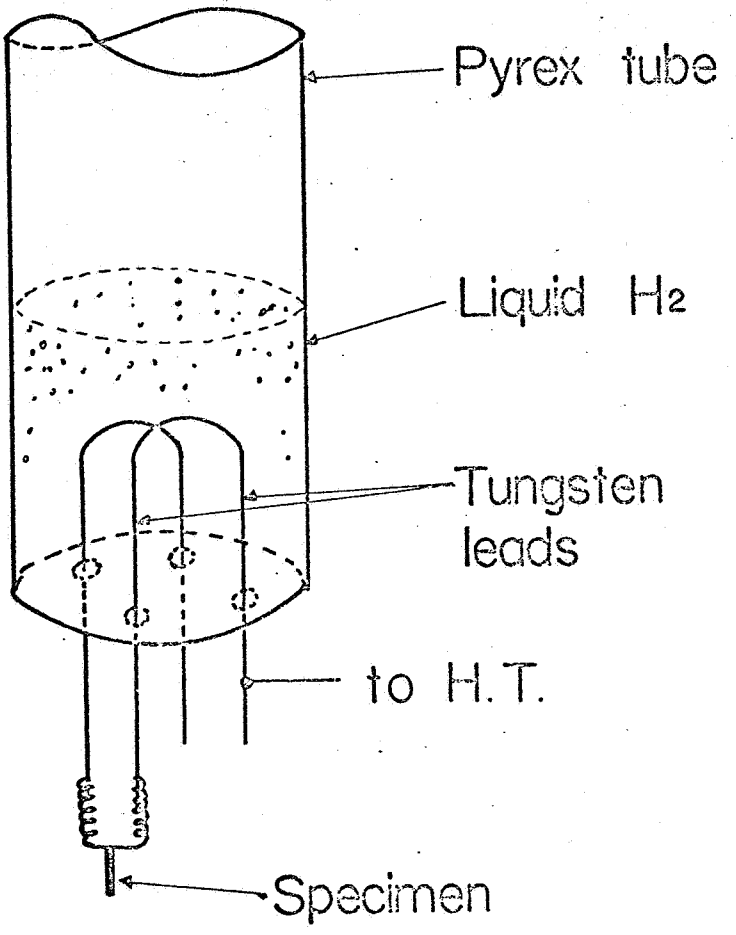

Figure 56.--Schematic drawing of the liquid hydrogen cryostat. The 0.050" thick tungsten leads are glass coated inside the cryostat. The high voltage connection is 0.015" thick Nichrome wire. The liquid hydrogen bath is maintained between 16 and 21°K.

Vacuum System

The most important consideration in designing the vacuum system is that it be capable of 10^{-8} to 10^{-9} Torr and that this pressure be attained in a reasonable length of time. This system employs a liquid nitrogen-trapped, 100 liter/sec, 2" oil diffusion pump which is capable of 10^{-8} Torr within two hours of specimen change. With mild bake-out, 10^{-9} Torr is attainable. The small diffusion pump can be quenched and exposed to air some ten minutes after shut-down, which eliminates the need for a roughing line.

Imaging Gas

The imaging gas supply has only one unique feature other than the mixing capability mentioned in Chapter IV. That is, the gas line passes through the liquid nitrogen shroud and is therefore precooled before entering the specimen chamber. It is believed that this increases thermal accommodation between the gas and the specimen.

High Voltage Generator

The high voltage power supply has continuously variable voltage control and provides up to ± 30 kV. The supply is extremely stable (0.01% ripple) and can compensate for up to 10% change in line voltage with only 0.005%

change in output voltage. This is an absolute necessity since slight variations in applied potential can easily cause a tip to flash. In order to eliminate the danger from high voltage discharges, a 5×10^8 ohm resistor is placed in series with the generator and specimen assembly. With a maximum current output of 1 ma, the maximum supply in the vicinity of the operator is 10^{-4} amp or 3 watts.

Viewing Port

Normally, a Pyrex or 7052 glass viewing port is used in field ion microscopes. The glass window is made electrically conducting by evaporating stannous oxide on the surface. A layer of Willemite is then deposited on the glass to provide a fluorescent screen. While this is quite suitable for viewing the image, it is not very efficient for photographically recording the image, without the use of image intensifiers. However, a fiber optic faceplate has been incorporated into this microscope which enables the operator to record the image by placing a photographic emulsion in intimate contact with the outer surface of the window. In other words, it is not necessary to focus a lens system onto the phosphor which is on the vacuum side of the window, as is the case with a Pyrex viewing port. Rather, with the fiber optics, the image is transmitted through the glass fibers (15 microns in diameter)

to the outer surface of the plate. Since the image is in focus to within the resolution of the individual fibers, it can be recorded directly. It has been observed experimentally that the exposure times are reduced by an order of magnitude over 35 mm techniques, and the quality of the final micrograph is much improved because the 4 × 5 negative need not be enlarged as much as the 35 mm film.

APPENDIX III

CALIBRATION OF THE ELECTRON MICROSCOPE

As the current in the intermediate lens of an electron microscope is increased, not only is the magnification increased, but the image also undergoes a rotation about the column axis. Before any quantitative work can be accomplished on defects in metals, the variation of these two parameters with lens current must be measured. This information is presently available for the Philips EM 200 fitted with a Rotating Tilting Specimen Stage (Feltner and Sefton 1964); however, the data is not valid for the newly acquired Goniometer Stage. All calibrations have been carried out with the intermediate, objective, and condenser I and II lenses set at negative (-) polarity and the magnification selector switch (MSS) set at position (2). The fine adjust knob of the intermediate lens control was set at full clockwise.

Magnification Calibration

The magnification at 100 kV, as given in Table 5, was determined at each position of the intermediate lens control by photographing a replica of a ruled grating (5.48×10^4 lines/inch) and measuring the line spacings

TABLE 5

MAGNIFICATION CALIBRATION OF PHILIPS EM 200 WITH THE GONIOMETER STAGE

Intermediate Lens		Magnification			
Position	Current (ma)	Plate	8×10 Print	35 mm	8×8 Print
1	60	. .	. .	. .	. .
2	80	13,150	32,880	5,480	36,520
3	100	23,020	57,550	9,590	63,920
4	110	29,590	73,960	12,330	82,200
5	125	37,490	93,730	15,620	104,120
6	150	59,180	147,950	24,660	164,380
7	160	65,760	164,400	27,400	182,640
8	170	74,980	187,450	31,240	208,240
9	190	84,170	210,430	35,070	233,780
10	210	97,320	243,300	40,550	270,300
11	240	109,820	274,550	45,760	305,040

from the 35 mm film and the glass plates. For completeness, the magnification after printing full-frame is also given. Since the lens current may vary slightly with specimen position, lens current has been plotted versus plate magnification in Figure 57.

Rotation Calibration

When going from a diffraction pattern to a bright field image, the intermediate lens current is changed giving rise to a relative rotation between the diffraction pattern and the image. Before crystallographic directions from the diffraction pattern can be transferred to the image, this rotation must be accounted for. Groves and Whelan (1962) pointed out that there is an additional 180° rotation between the diffraction pattern and the image because the intermediate lens is not energized when viewing the diffraction pattern. However, with the Goniometer Stage, the MSS set at position (2), the intermediate lens at (1), and the fine adjust turned full clockwise, *the intermediate lens is on.* Therefore, there is no additional 180° rotation for this set-up.

The rotation measurements were made by photographing the intersection of two slip traces in a platinum foil oriented so that the beam direction was [110]. Knowing this, and the width of the two slip traces, indices could

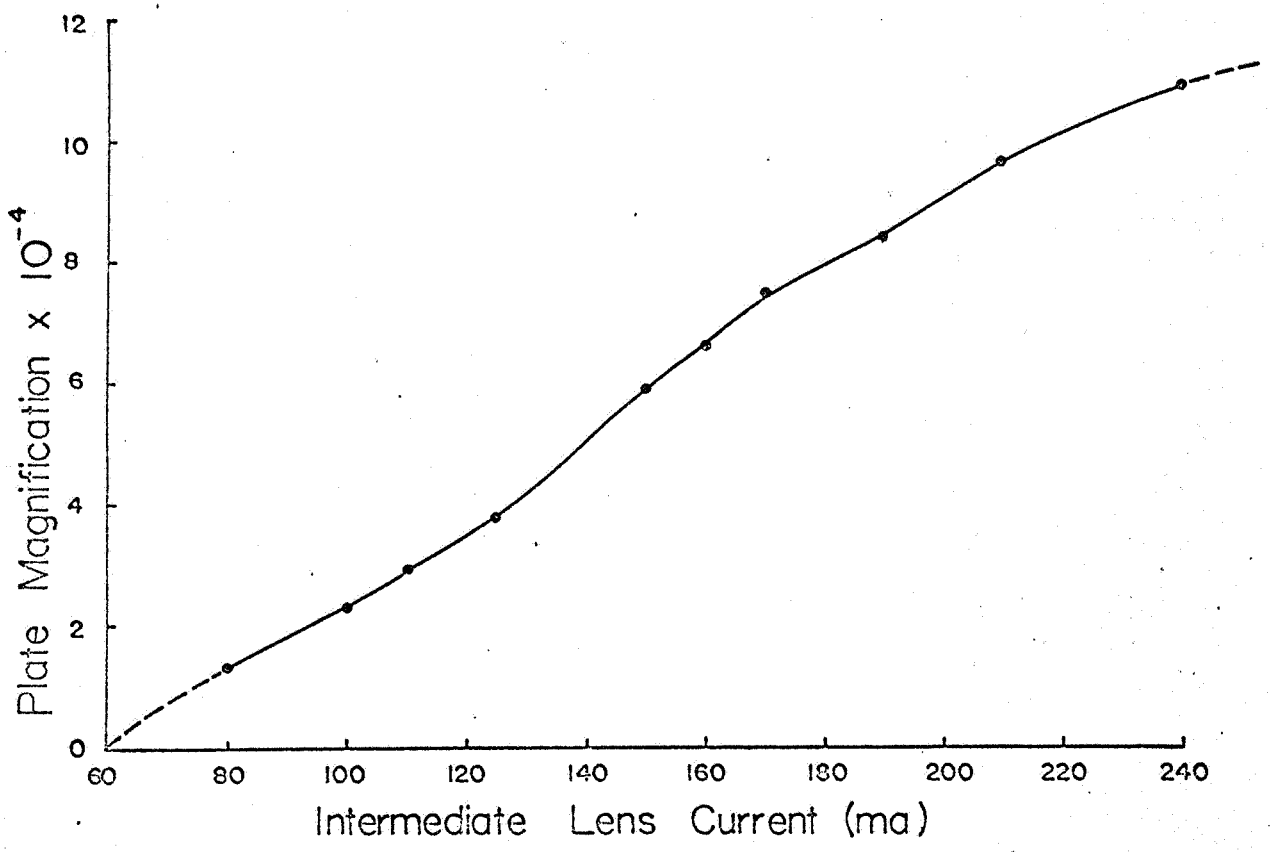

Figure 57.--Plot of intermediate lens current versus magnification for the Philips EM 200 fitted with the Goniometer Stage.

be assigned to the slip planes. As the magnification is increased, the image rotates counterclockwise through an angle as plotted in Figure 58. This, then, is precisely the angle through which the diffraction pattern must be rotated (also counterclockwise) in order to make the two coincident. The rotation has been found to decrease slightly as the diffraction lens current increases.

Position of the Tilt-Axis

The Goniometer Stage has been designed so that the tilt axis is always defined by the direction of motion of the image when the left hand stage control knob is rotated. Therefore, the tilt axis can be determined quite accurately while the specimen is under observation. It can be measured photographically by double-exposing a plate, before and after moving the specimen stage with the left hand control only. The line joining a single feature in the double-exposure is the tilt axis.

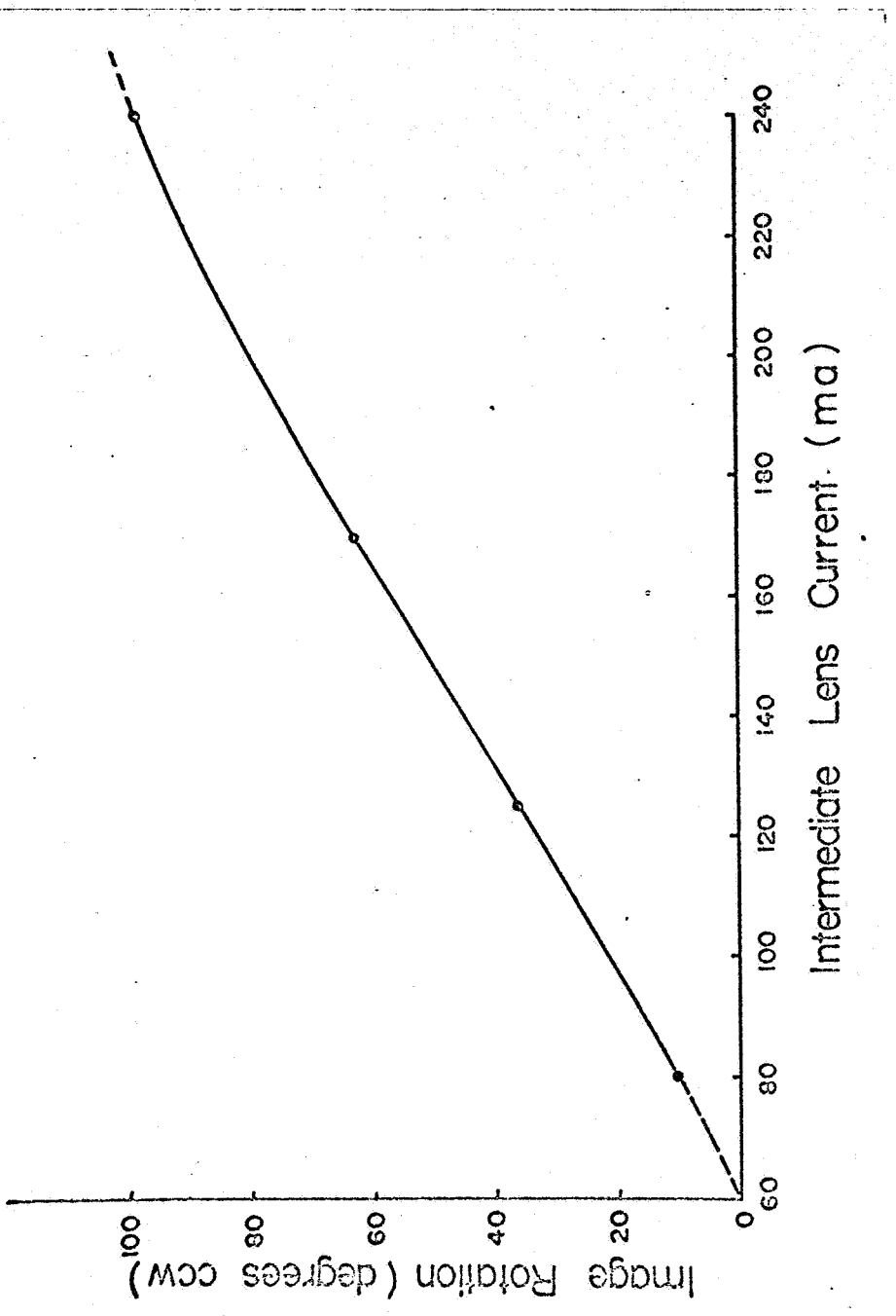

Figure 58.--Plot of intermediate lens current versus image rotation in the Philips EM 200 fitted with the Goniometer Stage.

BIBLIOGRAPHY

Ahlers, C. T. J., and Balluffi, R. W., 1967, *J. Appl. Phys.*, 38, 910.

Amelinckx, S., 1964, *The Direct Observation of Dislocations* (New York: Academic Press).

Ascoli, A., Asdente, M., Germagnoli, E., and Manara, A., 1958, *J. Phys. Chem. Solids*, 6, 59.

Ashby, M. F., and Brown, L. M., 1963a, *Phil. Mag.*, 8, 1083.

Ashby, M. F., and Brown, L. M., 1963b, *Phil. Mag.*, 8, 1649.

Bacchella, G. L., Germagnoli, E., and Granata, S., 1959, *J. Appl. Phys.*, 30, 748.

Bauer, W., and Sosin, A., 1966, *Phys. Rev.*, 147, 482.

Bell, W., Maher, D. M., and Thomas, G., 1965, *Lattice Defects in Quenched Metals* (New York: Academic Press), p. 739.

Bell, W. L., and Thomas, G., 1966, *Phil. Mag.*, 13, 395.

Bilby, B. A., Bullough, R., and Smith, E., 1955, *Proc. Roy. Soc.* A, 231, 263.

Blakely, J. M., and Mykura, H., 1962, *Acta Met.*, 10, 565.

Bowkett, K. M., Hren, J., Ralph, B., 1964, *Proc. Third Eur. Reg. Conf. for Elect. Micr.* (Prague: Publishing House of the Czechoslovak Academy of Sciences), p. 191.

Bradshaw, F. J., and Pearson, S., 1956, *Phil. Mag.*, 1, 812.

Brandon, D. G., 1964, *J. Sci. Inst.*, 41, 373.

Brenner, S. S., 1962, *Surfaces: Structure, Energetics and Kinetics* (Cleveland: American Society for Metals), p. 305.

BIBLIOGRAPHY--*Continued*

Bullough, R., 1967, private communication.

Chik, K. P., 1965, *phys. stat. sol.*, 10, 675.

Čížek, A., 1967, *Czech. J. Phys.*, B17, 186.

Clarebrough, L. M., 1964, *Phil. Mag.*, 9, 377.

Clarebrough, L. M., 1966, *J. Austr. Inst. Metals*, 11, 307.

Clarebrough, L. M., Humble, P., and Loretto, M. H., 1967, *Acta Met.*, 15, 1007.

Cottrell, A. H., 1953, *Dislocations and Plastic Flow in Crystals* (London: Oxford Univ. Press).

Cottrell, A. H., 1958, *Vacancies and Other Point Defects in Metals and Alloys* (London: Institute of Metals), Monograph No. 23.

Damask, A. C., and Dienes, G. J., 1963, *Point Defects in Metals* (New York: Gordon and Breach).

Darling, A. S., 1966, *Plat. Met. Rev.*, 10, 14.

de Jong, M., and Koehler, J. S., 1963, *Phys. Rev.*, 129, 49.

Doyama, M., 1965, *Lattice Defects in Quenched Metals* (New York: Academic Press), p. 163.

Drechsler, M., and Müller, E. W., 1952, *Zeit. für Phys.*, 132, 195.

Drechsler, M., and Wolf, P., 1958, *4th Int. Congr. for Elect. Micr.* (Berlin: Springer Verlag).

Edington, J. W., and West, D. R., 1966, *6th Int. Congr. for Elect. Micr.* (Tokyo: Maruzen Co. Ltd.)

Feltner, C. E., and Sefton, L. R., 1964, *Tech. Report SL 64-85*, (Dearborn, Michigan: Ford Scientific Laboratories).

Fortes, M. A., and Ralph, B., 1966, 13th Field Emission Symposium, Cornell Univ., unpublished.

BIBLIOGRAPHY--*Continued*

Frank, F. C., 1949, *Proc. Phys. Soc.*, A, 62, 202.

Frank, F. C., 1951, *Phil. Mag.*, 42, 809.

Frenkel, J., 1926, *Zeit. für Phys.*, 35, 652.

Friedel, J., 1964, *Dislocations* (New York: Pergamon Press).

Gevers, R., 1963, *Phil. Mag.*, 8, 769.

Gomer, R., 1961, *Field Emission and Field Ionization* (Cambridge, Massachusetts: Harvard Univ. Press).

Groves, G. W., and Whelan, M. J., 1962, *Phil. Mag.*, 7, 1603.

Hirsch, P. B., Howie, A., and Whelan, M. J., 1960, *Phil. Trans. Roy. Soc.* A, 252, 499.

Hirsch, P. B., Silcox, J., Smallman, R. E., and Westmacott, K. H., 1958, *Phil. Mag.*, 3, 897.

Howie, A., and Whelan, M. J., 1961, *Proc. Roy. Soc.* A, 263, 217.

Hren, J. J., 1967, private communication.

Hren, J. J., and Newman, R. W., 1967, *Rev. Sci. Inst.*, 38, 869.

Humble, P., Loretto, M. H., and Clarebrough, L. M., 1967, *Phil. Mag.*, 15, 297.

Jackson, J. J., 1965a, *Lattice Defects in Quenched Metals* (New York: Academic Press), p. 467.

Jackson, J. J., 1965b, *Lattice Defects in Quenched Metals* (New York: Academic Press), p. 479.

Jackson, K. A., 1962, *Phil. Mag.*, 7, 1117.

Kiritani, M., Shimomura, Y., and Yoshida, S., 1964, *J. Phys. Soc. Japan*, 19, 1624.

BIBLIOGRAPHY--*Continued*

Kuhlmann-Wilsdorf, D., 1958, *Phil. Mag.*, 3, 125.

Kuhlmann-Wilsdorf, D., 1965, *Acta Met.*, 13, 257.

Kuhlmann-Wilsdorf, D., Maddin, R., and Wilsdorf, H. G. F., 1960, *Strengthening Mechanisms in Solids*, (Cleveland: American Society for Metals), p. 137.

Lazarev, B. G., and Ovcharenko, O. N., 1955, *Dokl. Akad. Nauk. S.S.S.R.*, 100, 875.

Loretto, M. H., Clarebrough, L. M., and Humble, P., 1966, *Phil. Mag.*, 13, 953.

McIntyre, K. G., 1967, *Phil. Mag.*, 15, 205.

McLean, M., and Mykura, H., 1966, *Surface Sci.*, 5, 466.

Moore, A. J. W., 1962, *J. Phys. Chem. Solids*, 23, 907.

Mukherjee, K., 1966, *Trans. Met. Soc. AIME*, 236, 1324.

Müller, E. W., 1951, *Zeit. für Phys.*, 131, 136.

Müller, E. W., 1958a, *Acta Met.*, 6, 620.

Müller, E. W., 1958b, *4th Int. Congr. for Elect. Micr.* (Berlin: Springer Verlag).

Müller, E. W., 1959, *Structure and Properties of Thin Films*, (New York: John Wiley and Sons, Inc.), p. 476.

Müller, E. W., 1960, *Adv. Elect. and Electron Phys.*, 13, 83.

Müller, E. W., 1967, 14th Field Emission Symposium, Washington, D. C., unpublished.

Müller, E. W., Nakamura, S., Nishikawa, O., and McLane, S. B., 1965, *J. Appl. Phys.*, 36, 2496.

Newman, R. W., Sanwald, R. C., and Hren, J. J., 1967, *J. Sci. Inst.*, in the press.

BIBLIOGRAPHY--*Continued*

Newman, R. W., Sanwald, R. C., and Jenkins, E. J., 1967, submitted for publication.

Pashley, D. W., 1965, *Rep. Prog. Phys.*, 28, 291.

Pearson, S., and Bradshaw, F. J., 1957, *Phil. Mag.*, 2, 1387.

Piercy, G. R., 1960, *Phil. Mag.*, 5, 201.

Pimbley, W. T., Speicher, C. A., Attardo, M. J., Galligan, J. M., and Brenner, S. S., 1966, 13th Field Emission Symposium, Cornell University, unpublished.

Ranganathan, S., 1966a, *J. Appl. Phys.*, 37, 4346..

Ranganathan, S., 1966b, private communication.

Ranganathan, S., Bowkett, K. M., Hren, J. J., and Ralph, B., 1965, *Phil. Mag.*, 12, 841.

Rao, P., and Thomas, G., 1967, *Acta Met.*, 15, 1153.

Read, W. T., 1953, *Dislocations in Crystals* (New York: McGraw-Hill).

Ruedl, E., and Amelinckx, S., 1963, *J. Phys. Soc. Japan*, 18, Suppl. III, 195.

Ruedl, E., Delavignette, P., and Amelinckx, S., 1962, *J. Nucl. Materials*, 6, 46.

Rühle, M., and Wilkens, M., 1967, *Phil. Mag.*, 15, 1075.

Sanwald, R. C., 1967, Ph.D. Dissertation, University of Florida.

Sanwald, R. C., Ranganathan, S., and Hren, J. J., 1966, *Appl. Phys. Letters*, 9, 393.

Seidman, D., 1967, private communication.

Seitz, F., 1950, *Phys. Rev.*, 79, 890.

BIBLIOGRAPHY--*Continued*

Silcock, J. M., and Tunstall, W. J., 1964, *Phil. Mag.*, 10, 361.

Silcox, J., and Hirsch, P. B., 1959, *Phil. Mag.*, 4, 72.

Smallman, R. E., and Ashbee, K. H. G., 1966, *Modern Metallography* (Oxford, England: Pergamon Press).

Southon, M. J., and Brandon, D. G., 1963, *Phil. Mag.*, 8, 579.

Swanson, L. W., Reed, D. E., and Bell, A. E., 1967, 14th Field Emission Symposium, Washington, D. C., unpublished.

Thomas, G., 1962, *Transmission Electron Microscopy of Metals* (New York: John Wiley and Sons, Inc.).

van Landuyt, J., Gevers, R., and Amelinckx, S., 1965, *phys. stat. sol.*, 10, 319.

Yoshida, S., Kiritani, M., Shimomura, Y., and Yoshimaka, A., 1965, *J. Phys. Soc. Japan*, 20, 628.